Digital Holographic Studies on Detection of Defects in Honeycomb Sandwich Structures and Imaging of Stresses in Transparent Objects

A thesis submitted

in partial fulfillment for the award of the degree of

Doctor of Philosophy

by

BINU P. THOMAS

Department of Aerospace Engineering

INDIAN INSTITUTE OF SPACE SCIENCE AND TECHNOLOGY

Thiruvananthapuram, India

June 2019

CERTIFICATE

This is to certify that the thesis titled **Digital Holographic Studies on Detection of Defects in Honeycomb Sandwich Structures and Imaging of Stresses in Transparent Objects** submitted by **Binu P. Thomas**, to the Indian Institute of Space Science and Technology, Thiruvananthapuram, in partial fulfillment for the award of the degree of **Doctor of Philosophy**, is a bonafide record of the research work carried out by him under our supervision. The contents of this thesis, in full or in parts, have not been submitted to any other Institute or University for the award of any degree or diploma.

Prof. C. S. Narayanamurthy
Supervisor
Senior Professor, Department of Physics
IIST

Dr. S. Annamala Pillai
Supervisor
Former Deputy Director
Vikram Sarabhai Space Centre

Dr. Manoj T. Nair
Associate Professor and Head
Department of Aerospace Engineering
IIST

Place: Thiruvananthapuram
Date: June 2019

DECLARATION

I declare that this thesis titled **Digital Holographic Studies on Detection of Defects in Honeycomb Sandwich Structures and Imaging of Stresses in Transparent Objects** submitted in partial fulfillment for the award of the degree of **Doctor of Philosophy** is a record of original work carried out by me under the supervision of **Prof. C. S. Narayanamurthy** and **Dr. S. Annamala Pillai**, and has not formed the basis for the award of any degree, diploma, associateship, fellowship, or other titles in this or any other Institution or University of higher learning. In keeping with the ethical practice in reporting scientific information, due acknowledgments have been made wherever the findings of others have been cited.

Place: Thiruvananthapuram
Date: June 2019

Binu P. Thomas
Roll No.: SC11D010

This thesis is dedicated to my beloved parents

ACKNOWLEDGEMENTS

First and foremost, I thank God Almighty for enabling me to persevere the research work, whenever I experienced a lack of self-confidence, and complete this thesis. I wholeheartedly thank my father Thomas P. T., my mother Lilly Thomas, my wife Saritha and my children Tess and Tom for their prayers and love during hard times of my research.

I would like to express my sincere gratitude to my thesis supervisor Professor C. S. Narayanamurthy for his guidance and constant motivation throughout this study. I thank my thesis guide Dr. S. Annamala Pillai for his timely advice and suggestions which helped me to complete my thesis. I would also like to thank the members of my doctoral committee especially Professor Chandra Shakher, IIT Delhi and Professor Ramesk K., IIT Madras for their insightful comments and questions during the periodic review sessions which helped me to bridge the gap and provide completeness in my work. My sincere thanks also go to Dr. A. V. S. S. S. R. Sarma, with whom I began my career, for the inspiration to do research in holography.

I also thank all my friends and colleagues who supported me during the course of my research activities. I thank Dr. Digendranath Swain for the fruitful technical discussions we had during my work which helped me to progress my research activities. My thanks go to my friend Balamurali A. G. for his advice in the fields of structural dynamics and random vibration. I would also like to thank Karthigai Selvan S. and Suresh S. N. for the assistance they have provided to me during the experiments. I also highly appreciate the suggestions and opinions of Vysakh K. V. during my research work.

I also wish to express my gratitude to Director, VSSC for giving me permission to register for the Ph.D. course and supported me during the entire period of this course.

ABSTRACT

In satellite launch vehicles, honeycomb sandwich bonded constructions are extensively being used owing to its high bending stiffness and high specific strength. However reduction in stiffness due to debond and delamination in such structures may result in system failure. Vibration-based damage identification and health monitoring methods are widely used to ascertain proper bonding of face sheets to the honeycomb core. For inspection of such complex structures, the non-contact, whole field, highly sensitive, fast and easy to use optical interferometry techniques based on vibration are being inducted in aerospace industries. A few issues during the application of such optical techniques are addressed and solutions are proposed using one of the recent advancement in the field of interferometry called time average digital holography.

Honeycomb sandwich structures fabricated with curved edges for better structural integrity posed a problem to conventional methods in detecting debonded face sheets at the curved edges. Time average digital holographic method of inspection is proposed and the dynamic response of a debonded face sheet at the curved edge was mapped under a sinusoidal frequency sweep. The resonance frequency of the debonded face sheet at the curved edge was captured through frequency sweep and the feasibility of using time average method is established.

However, the procedure of frequency sweep to capture the resonance is time-consuming and it increases the inspection time. Hence the use of square wave excitation is proposed instead of sinusoidal frequency sweep for fast inspection. The advantage of square wave excitation over random excitation is also demonstrated experimentally. The effect of excitation magnitude and excitation location on the detectability of defects is also illustrated.

Most of the honeycomb sandwich structures are fabricated with potted-inserts to mount hardware ranging from electronic packages to mini-satellites. The effects of geometric and material discontinuities on the dynamic response due to the potted-inserts were studied for the successful application of optical inspection tools. Moreover, the dynamic response of plates with multiple holes and multiple stiffeners were also mapped simulating potted-insert sandwich structures. The above simulation was validated through both experiments and numerical studies. It is proposed that the extent of bonding of face sheet across potted insert can be evaluated at high excitation frequency.

A method to numerically plot holographic fringes, under the square wave and random excitations, is also proposed. The analytical solutions of the characteristic function of time average holography under two or more modes are provided by infinite series of the summation of the product of Bessel functions or by infinite series of probability density functions. However, these solutions under random or square wave excitation become very complex owing to the complex nature of the response under such excitations. A numerical solution through transient response analysis under random or square excitation using finite element method is proposed.

In satellite launch vehicles and space shuttles, transparent materials are being used for chemical storage and windows due to its transparency, high chemical resistance and strength. A study related to the application of digital holography for imaging stress fields in transparent objects was also carried out. A photoelastic digital holographic polariscope is proposed for imaging the stress field in both birefringent and non-birefringent transparent objects. This technique can be used for the inspection of defects in such transparent objects.

CONTENTS

LIST OF FIGURES

ABBREVIATIONS

CCD	-	Charge-coupled device
CMOS	-	Complementary metal oxide semiconductor
TADH	-	Time average digital holography
Re	-	Real part
Im	-	Imaginary part
FRF	-	Frequency response function
MAC	-	Modal assurance criterion
COMAC	-	Co-ordinate modal assurance criterion
RVAC		Response vector assurance criterion
GSC		Global shape correlation
GAC		Global amplitude correlation
MSC		Mode shape correlation
FEM	-	Finite element model
PPLA	-	Passenger payload adapter
NDT	-	Non- destructive testing
PMMA	-	Polymethyl methacrylate
USB	-	Universal serial bus
FEAST	-	Finite element analysis of structures
ISRO	-	Indian Space Research Organization
TAI	-	Time average interferograms
ODS	-	Operational deflection shape
PSD	-	Power spectral density
PLM	-	Product life cycle management

SYMBOLS

p	-	Spatial period of fringes
λ	-	Wavelength
θ_{or}	-	Angle between object and reference beams
$\Delta\xi$	-	Pixel size of sensor in horizontal direction
$\Delta\eta$	-	Pixel size of sensor in vertical direction
θ_{max}	-	Upper limit of angle between reference and object waves
$I(\xi, \eta)$	-	Intensity at the hologram plane
$E_R(\xi, \eta)$	-	Complex amplitude of reference wave field
$H(\xi, \eta)$	-	Complex amplitude of object wave field at sensor plane
k	-	Wave number
r	-	Distance between a point in hologram plane and a point in reconstruction plane
$E(x, y)$	-	Complex amplitude of reconstructed wave field
D	-	Distance between object and camera
M	-	Number of pixels along horizontal direction of sensor
N	-	Number of pixels along horizontal direction of sensor
$H(m, n)$	-	Digital output of sensor
φ_X	-	Experimental vibration modes
φ_A	-	Analytical vibration modes
$\Im$	-	Fourier transform
ϕ_h	-	Phase difference between two stress states of an object
$O(x, y)$	-	Object wave field
$o(x, y)$	-	Amplitude of object wave
$\phi_\omega(x, y, t)$	-	Phase of object wave field vibrating at frequency ω
H_1	-	Digital hologram at stress state 1
$d(x, y)$	-	Vibration amplitude

ω	-	Frequency of vibration
$\theta(x,y)$	-	Mode dependent phase distribution for multimodal vibration
M	-	Characteristic fringe function
T	-	Exposure time
J_0	-	Zero-order Bessel function of first kind
g_{rms}	-	Root mean square acceleration
I_{rec}	-	Intensity of reconstructed image
$\phi_0(r)$	-	Phase at rest position of vibrating object
$\phi_n(r)$	-	Phase as a function of space and frequency ω_n
Ω	-	Fringe locus function
$p(f)$	-	Probability density function
$f(t)$	-	Time function describing object motion
σ_1	-	Maximum principal stress
σ_2	-	Minimum principal stress
n_1	-	Refractive index along σ_1 direction
n_2	-	Refractive index along σ_2 direction
n_0	-	Refractive index of surroundings
n	-	Refractive index of unstressed material
m	-	Mass
c	-	Damping
k	-	Stiffness
$F(t)$	-	Forcing function
$\ddot{u}$	-	Second derivative of displacement
$\dot{u}$	-	First derivative of displacement
u	-	Displacement
A	-	Excitation amplitude
$H(\omega)$	-	Frequency response
ω_n	-	Natural frequency
φ_i,φ_j	-	Vibration modes
ξ_d	-	Damping coefficient
ϕ_{rnd}	-	Random phase
t_0	-	Thickness of unstressed material

t	-	Thickness of stressed material
ν	-	Poisson's ratio
E	-	Modulus of elasticity
P	-	Load
R	-	Radius of disc specimen
A, B	-	Stress optic coefficient
$P(\delta)$	-	Jones matrix of birefringent material
M_{ij}	-	Elements of Jones matrix
P_o	-	Jones matrix of polarizer
A_o	-	Jones matrix of analyzer
Q_{+45}	-	Jones matrix of quarter wave plate, fast axis at 45°
Q_{-45}	-	Jones matrix of quarter wave plate, fast axis at -45°
E_o	-	Object wave field arriving at sensor plane
E_{ox}	-	x-component of the object wave field
E_{oy}	-	y-component of the object wave field
E_R	-	Reference wave field
E_{rx}	-	x-component of the reference wave field
E_{ry}	-	y-component of the reference wave field
θ	-	Angle between maximum principal stress & horizontal axis
δ	-	Relative phase retardation
δ_i	-	Absolute retardation along principal stress directions
I_H	-	Intensity of holographic image
ψ_i	-	Phase change in principal stress directions of stressed model
Ψ	-	Phase change in unstressed model

CHAPTER 1

INTRODUCTION

1.1 Digital Holography

Holography is the science of recording and reproducing both amplitude and phase information of an optical wavefront (Erf, 1974). This is carried out through a two-step construction and reconstruction process. In the construction step, the object is illuminated with a coherent light source, commonly a laser, and the amplitude and phase of optical wave field from the object is recorded as an interference pattern called hologram, between the object wave and a reference wave, on a suitable recording media. The schematic of an off-axis hologram recording setup is shown in Figure 1.1. The laser beam is split into two using a beam splitter. One beam is expanded using a spatial filter assembly and this illuminates the object. The other beam is expanded using another spatial filter assembly and is made to fall directly on the recording media. The scattered light wave from the object and the reference wave interfere at the plane of recording media. In conventional holography, a high-resolution photosensitive film is used as recording media.

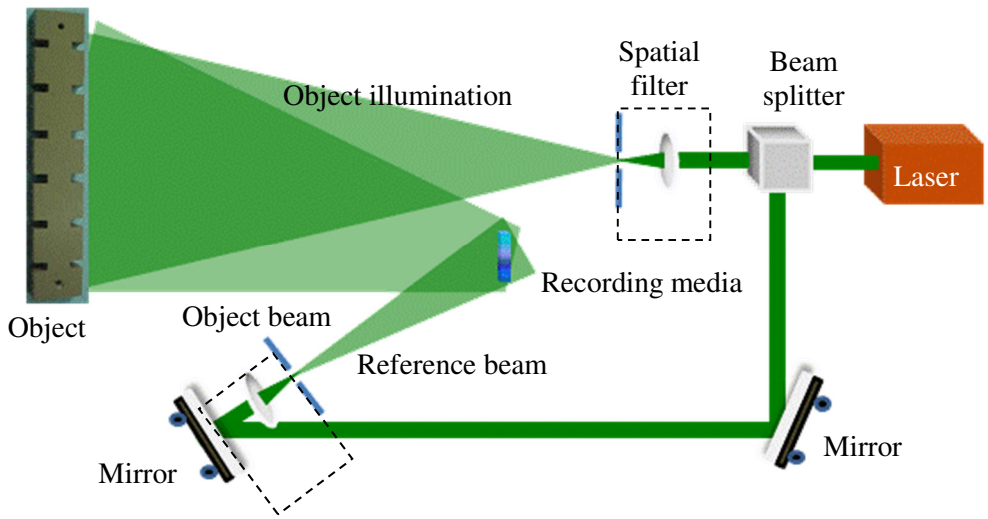

Figure 1.1 Schematic of off-axis hologram construction setup

The original object wave is reproduced by an optical reconstruction step where the wet processed film or hologram is illuminated with an expanded laser beam as shown in Figure 1.2 to produce the virtual image of the object.

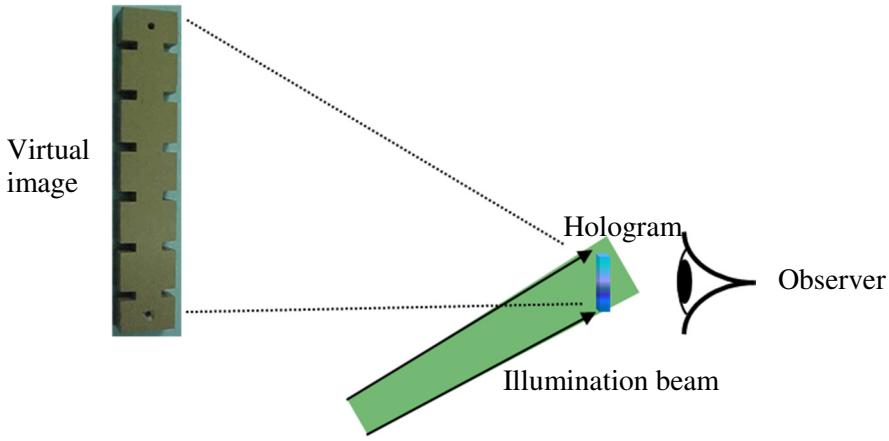

Figure 1.2 Schematic of optical reconstruction setup

Goodman and Lawrence, (1967) demonstrated the possibility of recording the interference pattern electronically in a Vidicon detector sampled in a 256 ×256 array using a lensless Fourier transform geometry and formation of the digital image through Cooley Tukey Fourier transform algorithm. However, with the advent of high-resolution digital image sensors, high-speed computers and advanced image processing algorithms, digital construction and reconstruction of hologram become more demanding and thus digital holography as a practical industrial tool was evolved. Digital holography using Fresnel transform is first demonstrated in the works by (Schnars and Juptner, 1994a; Schnars and Juptner, 1994b). In this method the holograms are recorded digitally using a digital image sensor instead of photosensitive film and reconstruction is carried out numerically instead of optical reconstruction. Thus digital holography eliminates the need for chemical wet processing and minimizes the stringent requirement of a dark room. The recording setup is same as that of conventional holography as shown in Figure 1.1 where the recording media is a digital image sensor like charge coupled device (CCD) or a complementary metal oxide semiconductor (CMOS) detector. The object and reference beams arrive at the image sensor plane and they interfere with each other directly on the surface of the sensor. The spatial period p of the resulting interference fringe pattern is given by Equation (1.1) (Kreis, 2005).

$$p = \frac{\lambda}{2\sin\left(\frac{\theta_{or}}{2}\right)} \tag{1.1}$$

where λ denotes the wavelength of the laser light used in recording the hologram and θ_{or} is the angle between the reference and object waves. The state-of-the-art image sensors are limited with a resolution of about 300 to 400 pixels/mm and recording of holograms is generally possible as long as the sampling theorem is fulfilled. According to the sampling theorem, the spatial period of the fringe pattern should be greater than twice the pixel dimensions ($\Delta\xi$, $\Delta\eta$) of the image sensor as given in Equation (1.2) (Kreis, 2005)

$$p > 2\Delta\xi \tag{1.2}$$

Since θ_{or} is kept small to minimize the fringe frequency, sin (θ_{or}/2) = tan (θ_{or}/2) = θ_{or}/2. From Equations (1.1) and (1.2) the upper limit of the angle θ_{max} between the rays from the object and reference beams is given by Equation (1.3) (Kreis, 2005).

$$\theta_{max} < \frac{\lambda}{2\Delta\xi} \tag{1.3}$$

If the object wave field at the hologram plane or sensor plane is given by $H(\xi,\eta)$ and the reference wave is given by $E_R(\xi,\eta)$ then intensity at the sensor plane $I(\xi,\eta)$ is given by Equation (1.4)

$$I(\xi,\eta) = [H(\xi,\eta) + E_R(\xi,\eta)][H(\xi,\eta) + E_R(\xi,\eta)]^* \tag{1.4}$$

Complex amplitude $E(x,y)$ of the diffracted wave field at the image plane is given by Fresnel-Kirchhoff integral as Equation (1.5) (Gaskil, 1978.)

$$E(x,y) = \frac{D}{i\lambda}\int_{-\infty}^{\infty}\int_{-\infty}^{\infty} H(\xi,\eta)\frac{\exp(ikr)}{r^2}\,d\xi d\eta \tag{1.5}$$

where r is the distance between a point in the hologram plane and a point in the image plane. Since the dimensions of the image sensor are small in comparison to

the distance *D* between the hologram and object, Fresnel approximations hold good. If a plane reference wave with unit amplitude is considered, then the complex amplitude *E(x,y)* is given by Equation (1.6) (Schnars and Juptner, 2002)

$$E(x,y)=\frac{\exp\left(\mathrm{i}\frac{2\pi D}{\lambda}\right)}{i\lambda D}\int_{-\infty}^{\infty}\int_{-\infty}^{\infty}H(\xi,\eta)\exp\left[\mathrm{i}\frac{\pi}{\lambda D}\left((\xi-x)^2+(\eta-y)^2\right)\right]\mathrm{d}\xi\mathrm{d}\eta \tag{1.6}$$

Upon simplification Equation (1.6) becomes

$$\begin{aligned}\mathrm{E}(x,y)&=\frac{i}{\lambda D}\exp\left(-\mathrm{i}\frac{2\pi D}{\lambda}\right)\exp\left(-\mathrm{i}\frac{\pi}{\lambda D}(x^2+y^2)\right)\\&\times\int_{-\infty}^{\infty}\int_{-\infty}^{\infty}H(\xi,\eta)\exp\left(-\mathrm{i}\frac{\pi}{\lambda D}(\xi^2+\eta^2)\right)\exp\left(-\mathrm{i}\frac{2\pi}{\lambda D}(x\xi+y\eta)\right)\mathrm{d}\xi\mathrm{d}\eta\end{aligned} \tag{1.7}$$

Considering *M*×*N* pixels in the sensor with $\Delta\xi$ and $\Delta\eta$ be the pixel sizes in the horizontal and vertical directions respectively, $H(\xi,\eta)$ be represented as *H(m, n)*, which is the digital output of the image sensor where *m* = 0, 1,.. *M*-1 and *n* = 0, 1, 2…*N*-1. The digital representation of equation (1.7) is given by Equation (1.8) (Schnars and Juptner, 2002)

$$\begin{aligned}\mathrm{E}(k,l)&=\frac{i}{\lambda D}\exp\left(-\mathrm{i}\pi\lambda D\left(\frac{k^2}{M^2\Delta\xi^2}+\frac{l^2}{N^2\Delta\eta^2}\right)\right)\\&\times\sum_{m=0}^{M-1}\sum_{n=0}^{N-1}H(m,n)\ \exp\left(-\mathrm{i}\frac{\pi}{\lambda D}\left(m^2\Delta\xi^2+n^2\Delta\eta^2\right)\right)\\&\times\exp\left(-\mathrm{i}\,2\pi\left(\frac{mk}{M}+\frac{nl}{N}\right)\right)\end{aligned} \tag{1.8}$$

Thus the complex amplitude of the real image *E(k, l)* is obtained by the Fresnel transform of the transmittance *H(m,n).* The intensity of the real image is given by the modulus of *E(k, l)* and phase is given by Equation (1.9).

$$Phase\,(k,l)=\frac{\mathrm{Im}[E(k,l)]}{\mathrm{Re}[E(k,l)]} \tag{1.9}$$

Thus single exposure method of digital holography, where the sensor is exposed to only one state of the object, can be used for imaging an object by plotting intensity map, given by modulus of Equation (1.8). However lensless Fourier digital holography proposed by (Wagner et al.,1999) improved the speed of numerical reconstruction by minimizing the number of mathematical operations. Here the effect of spherical phase factor associated with Fresnel diffraction pattern of the object is eliminated by use of spherical reference wave kept at the plane of the object. The complex amplitude of the reconstructed object field is given by Equation (1.10)

$$E(x,y) = \text{const.}\ \exp\left(\frac{\pi}{i\lambda D}\left(x^2+y^2\right)\right)\Im_{\lambda D}(H(\xi,\eta)) \tag{1.10}$$

where $\Im_{\lambda D}$ indicates the two dimensional Fourier transform modified by a factor $1/(\lambda D)$ given by

$$\Im_{\lambda D}(H(\xi,\eta)) = \int_{-\infty}^{\infty}\int_{-\infty}^{\infty} H(\xi,\eta)\exp\left(-i\frac{2\pi}{\lambda D}(\xi x+\eta y)\right)dxdy \tag{1.11}$$

Figures 1.3 (a), 1.3 (b) and 1.3 (c) show respectively the digital hologram of the object (in Figure 1.1), the intensity map and phase map of the numerically reconstructed wave. Details of the setup used to record this hologram and the real-time software developed to reconstruct this hologram are provided in Section 2.2.

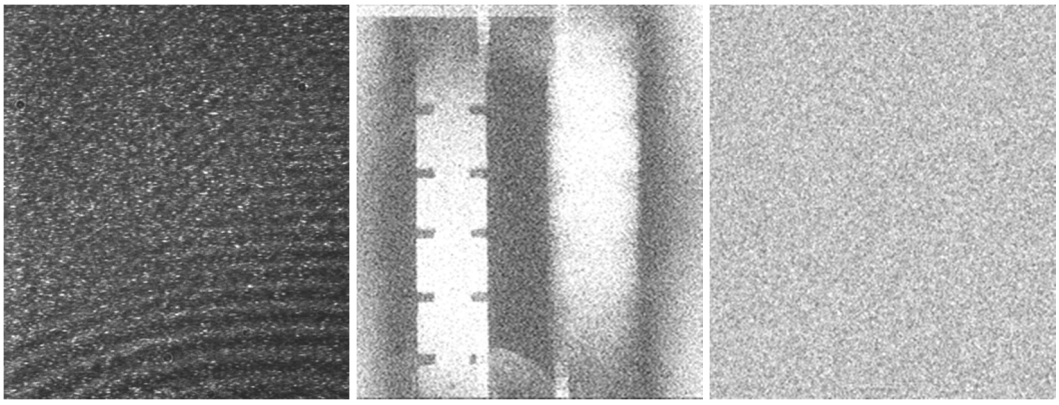

(a) (b) (c)

Figure 1.3 (a) Digital hologram (b) modulus and (c) phase map of the complex amplitude of reconstructed object field

1.1.1 Double exposure digital holography

In double exposure method of digital holographic interferometry, two states of the object are compared. Two holograms at two different states of the object are recorded using the image sensor as individual frames and are superimposed in the computer digitally. The resulting digital image is numerically reconstructed using Equation (1.8) to obtain the digital holographic interferogram. Flowchart for the generation of holographic interferogram is shown in Figure 1.4.

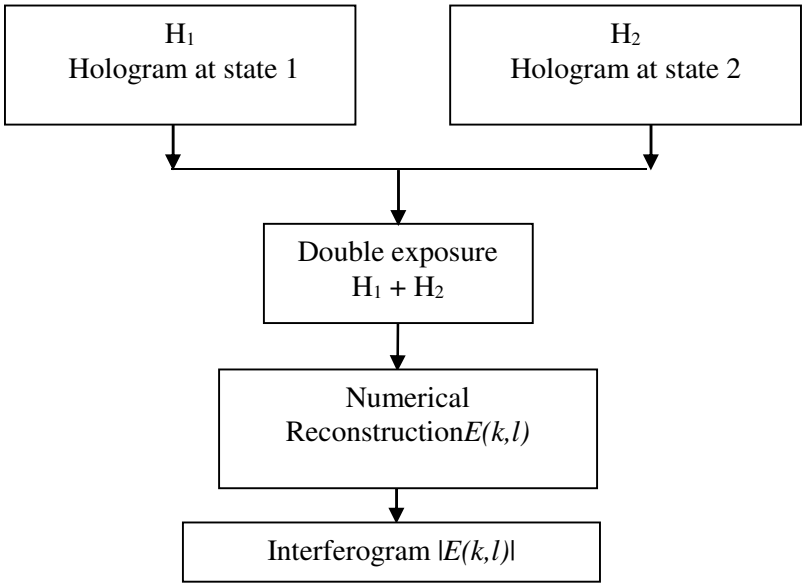

Figure 1.4 Flowchart for generation of double exposure digital holographic interferogram

The intensity I of the object image is modulated with fringe pattern represented by cosine of the optical phase difference ϕ_h between the two states of the object due to stressing the object. The phase difference can be due to a change in the refractive index or due to deformation or displacement of the object upon stressing. Different types of stressing like thermal, vacuum, mechanical, pressure and acoustic can be applied to study the respective changes in the state of object (Erf, 1974). Figure 1.5 shows the double exposure interferogram of an object under internal pressurization recorded using the setup used for the present study (refer Section 2.2).

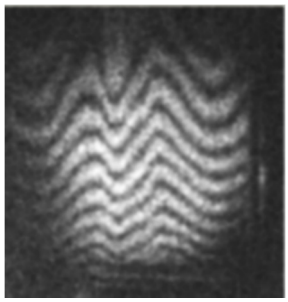

Figure 1.5 Double exposure holographic interferogram of an object under pressurization

The intensity of the reconstructed wave field of double exposure holographic interferogram is given by Equation (1.12) (Kreis, 1974).

$$I = a + b\cos\ (\phi_h) \tag{1.12}$$

where a is the DC term or additive noise and b is the modulation term or multiplicative noise. In the present, study lensless Fourier digital holography was also used to record holograms of large objects.

1.1.2 Time average digital holography (TADH)

Time average holography is an optical technique originated from the studies of (Powell and Stetson 1965; Stetson and Powell, 1965). Later it was established and used as a highly sensitive tool for vibration measurement and vibration analysis (Fryer, 1970; Pryputniewicz, 1985) through mode shape mapping and resonant frequency measurement. The sensitivity of vibration amplitude in the order of 0.1 μm made this technique popular as a tool for non-destructive inspection of defects in bonded structures, turbine blades etc. (Erf, 1974). In the time average method of holographic interferometry, the object under investigation is excited with sinusoidal vibration at an angular frequency ω, then the object field is given by Equation (1.13)

$$O(x,y,t)=o(x,y)\ \exp(i\phi_\omega(x,y,t)) \tag{1.13}$$

where the phase ϕ_ω, for normal illumination and recording conditions, is given by Equation (1.14)

$$\phi_{\omega}(x,y,t)=\frac{4\pi}{\lambda}d(x,y)sin(\omega t+\theta(x,y)) \tag{1.14}$$

Here *d(x,y)* is the amplitude of vibration and *θ(x,y)* is the mode dependent phase distribution for multimodal vibration and its value is zero for single mode vibration. In this method, the image sensor is exposed for a period of time *T* much greater than the period of vibration. Then the reconstructed object wave field, otherwise called as the characteristic function for time average holography M_c, is proportional to the time average of *O(x, y, t)* over the exposure interval *T* given by Equation (1.15) (Vest, 1979)

$$M_c \cong \frac{1}{T}\int_0^T o(x,y)exp\left(i\frac{4\pi}{\lambda}d(x,y)\sin(\omega t)\right)dt \tag{1.15}$$

Then intensity I_{rec} of the reconstructed image is proportional to the square of the characteristic function given by Equation (1.16)

$$I_{rec} \propto M_c^2 \cong \left|\frac{1}{T}\int_0^T exp\left(i\frac{4\pi}{\lambda}d\sin(\omega t)\right)dt\right|^2 \tag{1.16}$$

Using the integral definition of Bessel function the intensity of the reconstructed image is proportional to the square of the Bessel function of zero order given by Equation (1.17)

$$I_{rec} \propto M_c^2 \propto J_0{}^2\left(\frac{4\pi}{\lambda}d\right) \tag{1.17}$$

Thus the intensity of reconstructed image is modulated with fringe pattern representing contour of vibration amplitude related through square of the Bessel function of zero order. The nodes of the vibrating object, for which the amplitude of oscillation is zero, yield the maximum possible value for the squared zero-order Bessel function and therefore appear brighter than any other feature in the holographic interferogram. The dark fringes, at which the intensity drops to zero, corresponding to the zeros of the squared zero-order Bessel function of first kind J_0^2. Hence the fringe pattern recorded through time-average holography visually

indicates the amplitude of vibration in a full-field manner; thereby regions with large vibration amplitudes can be located on the object.

Pioneering works by (Picart et al., 2003; Borza, 2005) established that numerical reconstruction of single exposure digital hologram recorded with an exposure time much greater than the period of vibration modulates the object field with zero-order Bessel function and demonstrated that single exposure digital holography can be used for vibration studies. Off-axis setup shown in Figure 1.2 can be used to record time average digital hologram. The hologram can be reconstructed numerically using Equation (1.8). Validation of the experimental setup and software, used to record and reconstruct time average holograms during the present study, was carried out as explained in Section 2.2

1.2 Scope of the Thesis

Honeycomb core sandwich structures are widely being used in satellite launch vehicles because of its high specific stiffness. It consists of two metallic or composite face sheets bonded on either side of a metallic honeycomb core using film adhesives as shown in Figure 1.6.

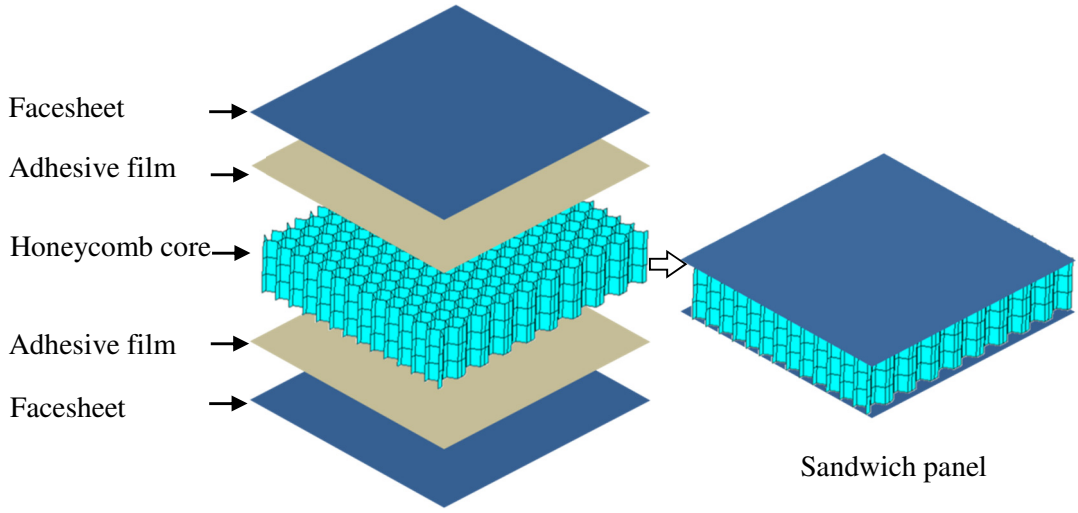

Figure 1. 6 Schematic of honeycomb core sandwich construction

A common defect found in these structures is the separation of adherents known as debond. Improper bonding or debond between the face sheet and the honeycomb core drastically reduces its stiffness and eventually debonded structure fails to perform its intended use. Moreover, under repeated loading, debond can propagate and trigger in-service failures. In space application, such structures range from huge payload fairing to small adaptors and decks and, these structures require a high level of reliability and hence detection of debond is very important. For inspection of such large and complex structures, industries are presently gearing-up into induction of fast and highly reliable optical interferometry techniques, which are non-contact, whole-field and highly sensitive. Vibration-based damage identification methods have been proposed in the literature to estimate the health of a structure by comparing the global and local changes in the dynamic response of a defective structure to that of a non-defective one. However, there are obstacles and challenges in implementing these methods as practical industrial tools. The exact location of defects cannot be identified from the global modal response to infer the severity of defects and for any further possible repair. Among the vibration based methods listed by Fritzen, (2005), the mode shape approach, makes use of the fact that a local change in the stiffness of the structure results in a local change in the mode shape and thus this approach can provide spatial information of a defect. Zou et al., (2000) explained that delamination decreases the stiffness and increases the damping of the structure, which in turn causes irregularity in the mode shape. The extent of irregularity in the mode shape depends on the size and location of the delamination. Hence for detecting defects using modal parameters, the most important task is to find the frequency at which a defect cause maximum irregularity in the mode shape. Montalvão et al., (2006) compiled the criteria proposed by various researchers for damage detection based on natural frequencies, frequency response function (FRF), mode shapes, FRF curvature, strain energy etc. Modal assurance criterion (MAC) determines the level of damage based on the correlation of mode shapes obtained through experimental and analytical methods or mode shapes obtained before and after damage. The MAC is defined inEquation (1.18) (Montalvão et al., 2006)

$$\mathrm{MAC}\left(\{\varphi_X\}_i\{\varphi_A\}_j\right)=\frac{\left|\{\varphi_X\}_i^T\{\varphi_A^*\}_j\right|^2}{\left(\{\varphi_X\}_i^T\{\varphi_X^*\}_j\right)\left(\{\varphi_A\}_i^T\{\varphi_A^*\}_j\right)} \tag{1.18}$$

where the subscripts *A* and *X* refer to the analytical and experimental vibration modes φ. A correlation value of 1 indicates that the mode shapes are identical, whereas a zero value indicates the mode shapes are totally different. Co-ordinate MAC (COMAC) is an improved criterion which provides the location at which the mode shapes do not agree. Similarly, response vector assurance criterion (RVAC), global shape correlation (GSC), global amplitude correlation (GAC) and mode shape curvature (MSC) are a few other criteria, based on modal parameters used for identification and location of damage. Modern type of structural damage detection methods like wavelet analysis method, genetic algorithm method and neural network method are explained in the review paper by (Yan et al., 2009). However in these methods also modal parameters are used for damage detection. The sensitivity of natural frequency and modal damping to impact damages in honeycomb core sandwich structures is compared by (Shahdin et al., 2010) and it is observed that damping is more sensitive to defect, Hence damping is proposed as a damage indicator tool for structural health monitoring. The review of fault detection methods based on mode shape by (Gandomi et al., 2008) has shown that vibration based approaches are potential tools for integrity assessment.

Farrar and Doebling, (1997) highlighted the importance of proper selection of sensors with sensitivity sufficient enough to detect the small changes in the modal parameters of damaged structures. Thereby, whole field optical techniques like shearography and holography are preferred in the industrial scenario. These techniques, under the class of vibration based non-destructive testing techniques, use modal parameters like resonant frequency and mode shape to identify local damages or defects present in a structure. In this thesis work, time average digital holography is used as a tool to provide solutions for a few practical issues faced during inspection of metallic honeycomb sandwich structures as described in Sections 1.3 to 1.6.

Furthermore, in the present research work, a method is proposed for imaging stress fields in transparent objects through digital holography and double exposure digital holographic interferometry. Inspection of such materials can be carried out by locating the regions of stress raisers due to any defect by imaging the stress fields.

1.3 Detection of Debond in Sandwich Structure with Curved Edges

Detection of debond between face sheets and honeycomb core of flat sandwich structures using the time average method of holography and shearography was extensively studied and illustrated in the literature (Erf, 1974; Vest, 1979). Erf et al., (1970) have demonstrated bond integrity evaluation in sandwich panels using ultrasonic excitation through mapping the change in the plate mode. Similarly, the application of time average method of shearography in detecting defects in metallic composite structures is demonstrated by (Toh et al., 1991; Steinchen et al., 1997). Steady-state vibration is proved as an effective stressing method for detecting debonds in honeycomb sandwich panels through both holography and shearography (Hung et al., 2000a; Clarady and Summers, 1993).

Debonded face sheet is identified as a region which resonates locally during a sinusoidal frequency sweep. Special manufacturing techniques like, cut and fold corner (Figure 1.7 (a)) or over expanded core (Figure 1.7 (b)) (Heimbs and Pein, 2009), are used to fabricate curved sandwich structures to minimize the joints for better structural integrity in certain sandwich constructions like passenger payload adaptors (PPLA) in launch vehicles to mount mini satellites as shown in Figure 1.7 (c). Inspection of curved edges with small radius or high curvature is limited by the size of sensors of ultrasonic equipment and Fokker bond tester. Since holography can image any complex shape, time average method of holography can be used to do inspection of such structures.

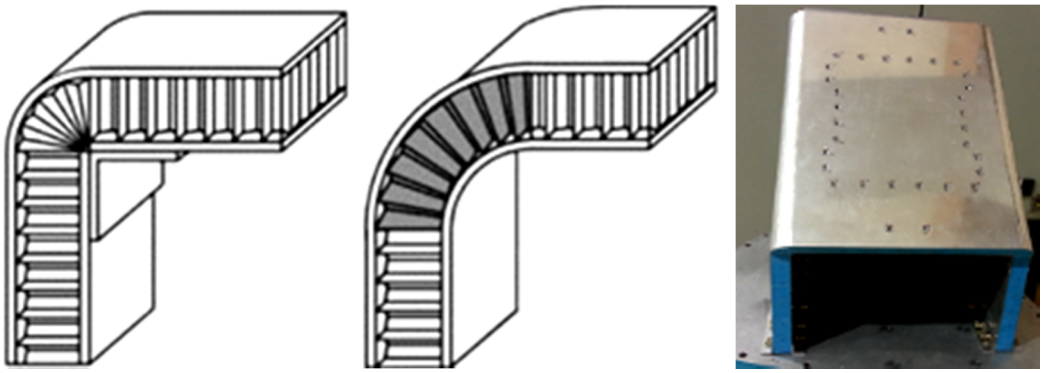

(a) (b) (c)

Figure 1.7 Schematic of curved sandwich construction with (a) cut and fold corner (b) over expanded core (c) photograph of payload adaptor with three edges of high curvature fabricated by cut and fold corner method

However, the effect of high curvature on the local resonance of a debonded metallic face sheet under forced vibration is not reported elsewhere and has to be studied to validate the time average digital holographic method for inspection of face sheet debond along curved edges. A few experimental studies using point sensors were reported to capture the global dynamic behavior of curved sandwich beams with composite skin sheets and with low curvature under free vibration (Baba and Thoppul, 2009; Erdogan and Yetmez, 2014). It is reported that in certain curved configurations, the modal frequencies remained the same even with the presence of debond when compared with the non-defective one. This is due to the additional bending stiffness provided by the curvature. Nevertheless, the displacement field or response map of a debonded face sheet along a curved edge is not addressed in the literature.

To confirm the feasibility of time average method of holography, the dynamic response of a debonded face sheet across a curved region during a sinusoidal frequency sweep was recorded using this technique. Towards this, a full fiber off-axis digital hologram recording setup was configured and real-time numerical reconstruction software was developed to record and save time average interferograms based on the fundamental works in the literature (Schnars and Juptner, 1994a; Picart et al., 2003; Schnars et al., 1996). Results of this study are elaborated in Chapter 2.

1.4 TADH with Square Wave Excitation

Time average method of holography and shearography conventionally uses sinusoidal frequency sweep to capture the local resonance of defective regions (Erf, 1974; Vest, 1979). In the present study, numerical frequency response analysis of honeycomb core sandwich specimens with or without debonds using finite element method (FEM) is carried out to demonstrate the requirement of frequency sweep in detecting the local resonances. Moreover, time average holographic fringes are plotted theoretically using the displacement responses at frequencies corresponding to the maximum response obtained from the frequency response curve. However, the present approach of frequency sweep requires a large number of holograms to be recorded to identify the frequency at which defects resonate and in turn to detect the defects. The difficulties with the conventional approach of frequency sweep are highlighted in this study. However, the use of random excitation is reported in the literature with the idea to reduce the number of time average holograms recorded during a frequency sweep (Clarady et al., 1983). The use of random excitation is demonstrated on a honeycomb-cored structure with programmed defects using film holography and through image plane holography (electronic speckle interferometry) (Clarady, 1990; Clarady and Summers, 1993). However, random excitation should be provided within a predetermined frequency range in line with the resonant frequencies of defects of possible sizes and locations. Such random vibrations are difficult to be generated through a common function generator. Moreover, advanced systems are required to generate random vibrations for a particular band of frequency and with the desired energy level. Hence a novel defect identification strategy is proposed which enhances the speed and accuracy of inspection. Moreover, the issues with the identification of defects from the complex fringe pattern due to the overlay of global and local modes, time-consuming frequency sweep in search of local resonances and high sensitivity of the fringe pattern with excitation amplitude and its application point are illustrated. Square wave excitation strategy proposed for characterization of defects overcomes the prevailing issues and also certain practical aspects of random excitation. Extensive experiments were conducted to validate the new approach. It is noticed that the

proposed methodology is much faster and economical for the identification of defects. Details of this study are described in Chapter 3.

1.5 Detection of Debond in Potted-Insert Sandwich Structure

Large numbers of metallic inserts are potted in certain sandwich structures especially in those used in launch vehicles to mount electronic packages and mini satellites as shown in Figure 1.8. Hot bonded inserts, co-cured along with the fabrication of sandwich panel, become an integral part of the structure with bond lines on both face sheets and are very strong when compared to cold inserts which are post bonded (Bianchi et al., 2010). The bond line of a cold insert is shown in the schematic of insert in Figure 1.9.

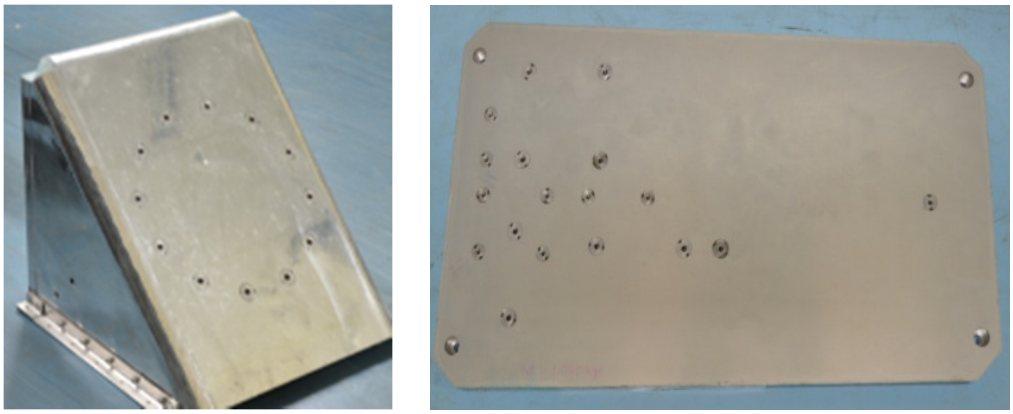

Figure 1. 8 Sandwich structures with potted-inserts

For post-bonding the inserts, a hole has to be drilled in the existing panel upto the bottom face sheet with a diameter sufficient enough for insertion of the metallic insert. The insert is then placed on the bottom face sheet after applying a thin layer of adhesive on the bottom face sheet and the potting compound is injected through the runner. Then the room temperature adhesive which is used as the potting compound is allowed to cure. The top of such fully potted inserts can be either in line with the face sheet or project above the face sheet. The former configuration is called flush insert and the latter is called collar insert. Schematic of a collar insert is shown in Figure 1.9. These inserts should be properly potted into the panel and

their bonding has to be verified or inspected to avoid possible failures (Thomsen, 1998; Rao et al., 2005). The major failure modes in sandwich structures with inserts are listed as the face sheet failure caused by the bending stress concentrations induced adjacent to the insert, the face sheet 'bearing' failure at the insert/face sheet intersections, potting to insert interface or the bottom potting to face sheet interface failure due to the induced transverse normal and shear stresses, honeycomb to face sheet interface failure due to the presence of transverse normal and shear stress concentrations adjacent to the potting/honeycomb intersection. Thus debond of face sheets across and adjacent to the metallic inserts should be detected. Many non-destructive testing (NDT) techniques have been proposed to detect the face sheet debond. Because of the complex geometry of honeycomb core, most of the conventional techniques like X-ray radiography and ultrasonic technique failed as practical NDT techniques. Thermography is extensively used in sandwich panels with composite face sheets but it is not so effective in case of metallic face sheets. It is difficult to distinguish small changes on the surface temperature of thin metallic face sheets with defects and to separate the defect-related effects on the surface temperature from that due to geometric and material discontinuity created by metallic inserts (Ibarra-Castanedo et al., 2009; Sfarra et al., 2010). Shop floor techniques like Fokker bond and woodpecker methods are time-consuming point techniques and difficult to apply near holes and local stiffeners, which calls for advanced NDT methods.

In the present work, one such advanced technology called time average digital holography (Picart et al., 2003) was used to study the effect of potted inserts on the face sheet debond. Digital holographic interferometry is reported as a highly sensitive inspection tool which can measure small variations in physical, mechanical or thermal parameters in various engineering and medical fields (Sharma et al., 2012; Pérez-Huerta et al., 2017; Ruiz et al., 2018). Quantitative measurement of displacement and strain through direct calculation of phase information from the numerically reconstructed complex amplitude is also reported (Kumar and Shakher, 2016).

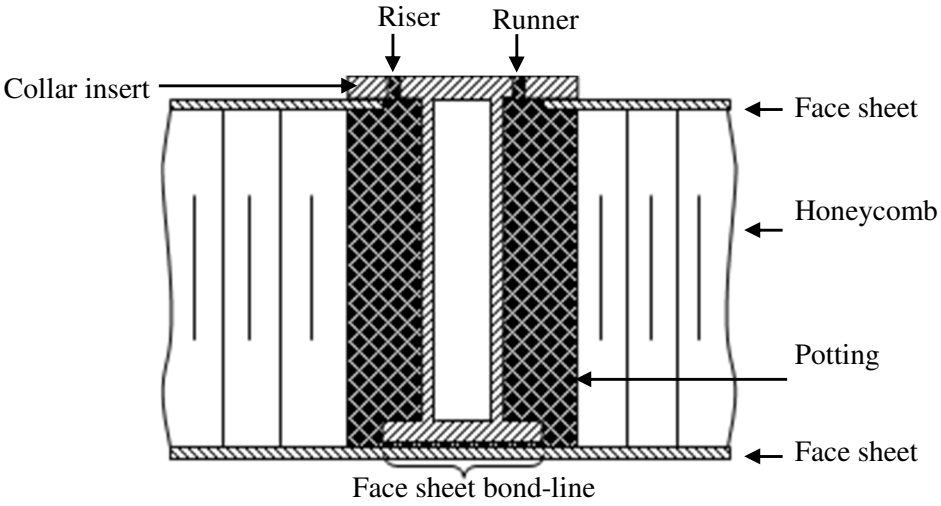

Figure 1. 9 Schematic of potted-insert showing face sheet bond-line

The inserts which are made of stiffer and stronger material compared to the honeycomb core along with potting compound act as hard points in the sandwich panel (Bozhevolnaya et al., 2004; Thomsen and Rits, 1998). Hence the effect of geometric and materials discontinuities due to the introduction of metallic inserts on the operational deflection shape need to be studied for implementation of the above technique as an industrial tool. However out of plane displacement and its derivative in panels with one fully potted insert under static loading using electronic speckle pattern interferometry and shearography is reported (Huang and Lin, 2008; Huang et al., 2007). Nevertheless, the dynamic response of plates or sandwich panels with localized stiffeners and holes are hardly reported. Moreover non-linear dynamic analysis of debonded sandwich panels without inserts carried out using finite element method by (Burlayenko and Sadowski, 2012; Burlayenko and Sadowski, 2014), using contact elements reported a variety of behaviour like periodic, quasi-periodic and irregular motions within the debond zone and this makes the numerical prediction even more difficult in potted-insert panels. Time average method of holography and shearography under vibration excitation detect defects through identification of locally resonating regions captured through a frequency sweep. However, inserts which are made of stiffer and stronger material compared to the honeycomb core along with potting compound alter the local response of defective face sheet. Hence dynamic responses of sandwich structures with fully potted inserts, which are hardly reported, need to be studied for successful use of time average method. In this thesis work, the digital method of time average

holography was employed to understand the behaviour of insert potted sandwich structure. Both numerical and experimental studies were carried out and the dynamic responses were compared with that of the potted-insert sandwich structure. The details of this study are presented in Chapter 4.

1.6 Computed TADH for Random Excitation

Successful application of holographic interferometry technique for the non-destructive testing of any structure or component depends upon the proper selection of the type and magnitude of stressing, which can create an anomaly in the surface deformation due to the presence of a surface or subsurface defect. Generally, calibration experiments are conducted with all expected types and sizes of defects programmed in a sample. Interferograms of samples with programmed defects are recorded with various types of stressing like mechanical, pressure, vacuum, thermal, acoustic, and vibration with different magnitudes. The details of excitations which can trigger the defects to produce local discontinuities in the surface deformation which in turn create fringe anomalies are documented for routine testing. In this context, the theoretical simulation of holographic fringe patterns is very much necessary to arrive at the optimum stressing method for each type of defect in each type of component. This will reduce the number of experiments and specimens and also provide a prior knowledge on the fringe anomalies for each type of defect. Matczak (1994) has shown that computer-aided simulation of double exposure holographic fringes with holographic measuring system parameters can be applied to design such inspection systems, for quantitative interpretation of holographic interferograms and to characterize the type of defect. Theoretical plotting of double exposure holographic fringe patterns through customizing a finite element software package is reported by (Thomas et al., 2005). In that paper, the structural deformations obtained through static analysis is used along with the experimental parameters like the wavelength of the laser and coordinates of the object, reference beam and recording media. These parameters can alter the nature of the fringe pattern and also the fringe density.

Similarly, interference fringe pattern under dynamic response of structures or time average holographic fringe patterns are also plotted for visualization of dynamic response prior to experiments and for better evaluation of experimental interferograms (Ragulskis et al., 2003; Roesel et al., 2003). The characteristic fringe function of time average holography for single frequency sinusoidal excitation is proportional to the zero order Bessel function of first kind whose argument is proportional to the amplitude of vibration. And intensity is square of the zero order Bessel function given by Equation (1.17). However, the characteristic function becomes very complex for multiple excitations and for multiple modes of vibration. For a typical non-sinusoidal vibration and for other general forms of motion the characteristic fringe function is defined by (Gupta and Singh, 1975; Zambuto and Lurie, 1970). Depending upon rational and irrational modes of vibration, the characteristic function respectively becomes infinite series of sum of the product of Bessel function or product of Bessel function with argument proportional to vibration amplitude of individual modes as reported in (Wilson, 1970; Wilson and Strope, 1970). The characteristic fringe function for an object whose motion is considered as sum of a series of sinusoidal functions of time having arbitrary amplitudes, frequencies ω_n, and relative phases θ_n is given by Equation (1.19)(Wilson, 1970)

$$M_c = e^{i\phi_0(r)} \sum_{\substack{m- \\ 1}}^{M} \prod_{n=1}^{N} i^{l_{nm}} J_{l_{nm}} [\phi_n(r)] e^{-il_{nm}\theta_n} \tag{1.19}$$

where $\phi_0(r)$ relates to the rest position of the object, $\phi_n(r)$ characterizes the peak phase variation as a function of space and frequencies ω_n and l_{nm} are the positive and negative $M \times N$ integer roots of the M set of equations given by Equation (1.20)

$$\sum_{n=1}^{N} l_{nm}\omega_n = 0 \tag{1.20}$$

If $\phi(r,t)$ is given by three odd-harmonic sinusoidal time function as Equation (1.21)

$$\begin{aligned} \phi(r,t) = \phi_0(r) + \phi_1(r)\sin(\omega t - \theta_1) + \phi_2(r)\sin(3\omega t - \theta_3) \\ + \phi_5(r)\sin(5\omega t - \theta_5) \end{aligned} \tag{1.21}$$

Then the characteristic fringe function is given by Equation (1.22) (Wilson, 1970)

$$\begin{aligned} M_c = {} & J_0(\phi_1)J_0(\phi_3)J_0(\phi_5) + J_0(\phi_1)J_{\pm5}(\phi_3)J_{\pm3}(\phi_5)e^{-i(\pm5\theta_3\pm3\theta_5)} \\ & + J_{\pm5}(\phi_1)J_0(\phi_3)J_{\pm1}(\phi_5)e^{-i(\pm5\theta_1\pm\theta_5)} \\ & + J_{\pm3}(\phi_1)J_{\pm1}(\phi_3)J_0(\phi_5)e^{-i(\pm3\theta_1\pm\theta_3)} \\ & + J_{\pm1}(\phi_1)J_{\pm3}(\phi_3)J_{\pm2}(\phi_5)e^{-i(\pm\theta_1\pm3\theta_3\pm2\theta_5)} + \cdots \end{aligned} \tag{1.22}$$

Computed time average fringe pattern for a circular plate vibrating at two different modes are described in (Wilson, 1971). In this paper, the characteristic fringe function provided by Equation (1.22) is used to plot the fringe patterns. Here a circular plate clamped along the edges is made to vibrate under two independent sources of excitation, and frequencies are controlled in such a way that to excite the first two vibration modes. However, this approach becomes very complex for simulation of time average fringes under square and random wave excitations. Moreover, the complexity of time average fringe patterns increases during the transition between rational and irrational modes. Molin and Stetson, (1969) have shown that for objects vibrate with combination of their basic resonant modes the time average fringe patterns show distinctive modifications. For independent frequencies, the joined characteristic function is the product of the fringe function and for same frequency, the fringe function argument is the vector addition of the motion at individual modes given by following equations respectively.

$$M_c = J_0(\bar{\Omega}_1)J_0(\bar{\Omega}_2) \tag{1.23}$$

$$M_c = J_0(|(\bar{\Omega}_1)+(\bar{\Omega}_2)|) \tag{1.24}$$

where $\bar{\Omega}$is the fringe locus function i.e., amplitude of the object motion. Pedersen and Lglkberg, (1994) have also reported that at low excitation level the fringe function for time average holography under non-periodic sinusoidal excitations is given by the product of the fringe functions for each of the harmonic vibration components as given by Equation (1.23). However, if the object vibrates at high excitation level, identification of an individual fringe function becomes difficult.

Another definition of characteristic function based on probability density function is provided by Stetson, (1971). According to this, the characteristic function is given by Equation (1.25)

$$M_c = \int_{-\infty}^{+\infty} p(f)\, exp(i\Omega f) df \tag{1.25}$$

where Ω is the fringe locus function, *f(t)* is the time function describing the motion of the object and *p(f)* is the density function of *f(t).*

Ganesan et al., (2000) reported use of time average holography to map the response of objects vibrating simultaneously at different modes. The changes in the fringe pattern during the transition from rational to irrational relation of the frequencies of vibration are illustrated in this paper. Separation of vibration modes during such vibration is reported by Ganesan et al., (1994) using speckle interferometry. A method based on stroboscopic holographic interferometry to capture rational vibration modes is explained by Alexeenko et al., (2009). All the above studies explain the difficulty to arrive an analytical solution for the characteristic function of time average holography under random excitation or square wave excitation with any magnitudes of excitation.

In the present work, a numerical method is proposed to simulate time average fringe under periodic non-sinusoidal and random excitations. In this method probability density function of the displacement response calculated through transient response analysis using finite element method was used. The transient response analysis under random vibration was carried out using a random time signal generated from a given power spectral density. These simulations can be used for parametric studies in the detection of debonds in sandwich structures under square or random excitations using time average holography. The details of this study are presented in Chapter 5

1.7 Imaging of Stresses in Transparent Objects

Transparent non-crystalline materials are widely used in launch vehicles, spacecrafts and in many machines and equipment. In general, such materials can be divided into two categories, namely birefringent materials whose refractive index depends on the stress applied to it and non-birefringent materials whose refractive index is independent of the applied stress. Thus the birefringent materials are optically isotropic when there is no applied stress and becomes optically anisotropic whenever stress is applied. Photoelasticity is an experimental stress analysis technique in which the state of stress in birefringent materials is determined by its effect on the polarization state of light when trans-illuminated through them with a polarized light (Vest, 1979). Whenever a polarized light beam passes through a stress-induced birefringent material its refractive indices along the directions of the principal stresses σ_1 and σ_2 become n_1 and n_2 respectively. Such stress-induced birefringent material when viewed, through crossed polarizers, exhibits two types of fringe systems, namely isochromatic and isoclinic. The fringe system which shows the difference in principal stresses is known as isochromatic and they are contours of constant values of σ_1-σ_2.Isoclinic fringe system shows the direction of the maximum principal stress. Along with the differences in principal stresses, photoelasticity can map the sum of principal stresses in birefringent materials, making use of Maxwell-Neumann equations. Numerous classical optical methods like polariscope, Mach-Zehnder interferometer, conventional holographic interferometry and photorefractive holographic interferometry have been widely used to find the isochromatic and isopachic fringes of stress-induced birefringent materials (Nisida and Saito, 1964; Fourney, 1968; Fourney and Mate, 1970; Hovanesian et al., 1968; Sanford, 1980).

Compared with interferometry techniques like polariscopes and Mach-Zehnder interferometer, the holographic technique introduced by (Fourney, 1968; Hovanesian et al., 1968) to find simultaneously the isopachic and isochromatic fringes alleviated most of the problems associated with the former techniques. But, the problem of wet processing of recorded holograms still posed problems and also

the analysis of phase information from the recorded hologram. Narayanamurthy and Dainty (1992) using photorefractive $Bi_{12}SiO_{20}$ (Bismuth Silicon Oxide) crystal developed a new dynamic holographic photoelasticity technique. Though, this technique eliminated wet processing of recorded holograms, the evaluation of phase information of photoelastic isochromatic/ isoclinic or isopachic fringes remained unsolved. The advancement in digital methods of holography paved way for polarization imaging studies to record and quantify the distribution of polarization states in microscopic to macroscopic objects through different configuration of optical elements as reported by (Beghuin et al., 1999; Colomb et al., 2002; Colomb et al., 2005; Tahara et al., 2011). A digital holographic interferometer proposed by Desse and Olchewsky, (2018) can record the density gradients during transonic and supersonic flows through mapping the refractive index change. Similarly using digital holography, Narayanamurthy et al., (2017) have developed a new photoelasticity technique for studying isochromatic and isopachic fringes of stressed PMMA (Polymethyl methacrylate) material. But, this method did not include circular polarizers in the object and reference arms respectively, as these are required for recording simultaneously the isochromatic and isopachic fringes superposed with isoclinic fringes of stressed photoelastic material. This is because, if the reference wave is vertically polarized or horizontally polarized, then the reconstructed hologram will have real amplitude and phase distribution from the identical respective components of object wave. This is irrespective of the state of polarization of reconstruction wave and instead, if the object and reference waves are circularly polarized then both vertical and horizontal components can be simultaneously recorded in a single hologram (Vest, 1979). Moreover, the experimental geometry used by Narayanamurthy et al., (2017) was Mach-Zehnder interferometric geometry, and that requires stringent optical quality of the material under test, which is normally difficult to achieve. Thus, by introducing circular polarizers in the object and reference beams of a holographic photoelasticity geometry one can record complete polarization states of stressed birefringent material. A digital holographic polariscope method is proposed, by combining polariscope and digital holography for measuring isochromatic and isopachic fringes for both birefringent and non-birefringent transparent non-crystalline

materials. It is demonstrated that conventional circular polariscope could not show isopachic fringes for stressed non-birefringent material, whereas the proposed digital holographic polariscope could detect these fringes. Details of this study are presented in Chapter 6

CHAPTER 2

DYNAMIC RESPONSE OF CURVED SANDWICH STRUCTURE

2.1. Introduction

Detection of debonds at sharply curved edges on sandwich structures is found difficult using conventional non-destructive testing (NDT) techniques. Many non-destructive testing techniques have been developed to detect and assess debonds, like for example X-ray radiography, ultrasonic technique and thermography to detect the defects. However, each technique has its own limitation due to the complex nature of honeycomb construction, large sensor size and thin metallic face sheets with high thermal conductivity. However, thermography is an established technique for debond detection in sandwich structures with composite face sheets. Shearography is another optical technique, which has been successfully developed as a practical NDT tool in recent years for composite structures (Findeis and Gryzagoridis, 2014). However, due to recent developments in digital holography, the determination of defects becomes more precise and accurate. The advantages of digital holography and time average holographic interferometry are utilized to detect debonds along the curved edges of sandwich structures. As explained in Section 1.3 the effect of high curvature on the vibration behaviour of a sandwich structure is not reported in literature. In the present study, the dynamic response of debonded face sheet along the edges with high curvature was mapped through time average digital holography technique and the feasibility of this technique for identifying debond region of curved sandwich structures is established. For this study, an experimental setup for recording time average digital hologram was set-up as explained in the next section. The details of the software developed to record and reconstruct time average digital holograms in real time are also explained in the next section.

2.2. Experimentation Details

The schematic of the experimental setup used for recording time-average digital hologram is as shown in Figure 2.1. It was an all-fiber off-axis hologram recording setup where the optical elements like spatial filter assembly, mirrors and beam splitter cube (shown in Figure 1.1) were replaced with a bifurcated optical fiber.

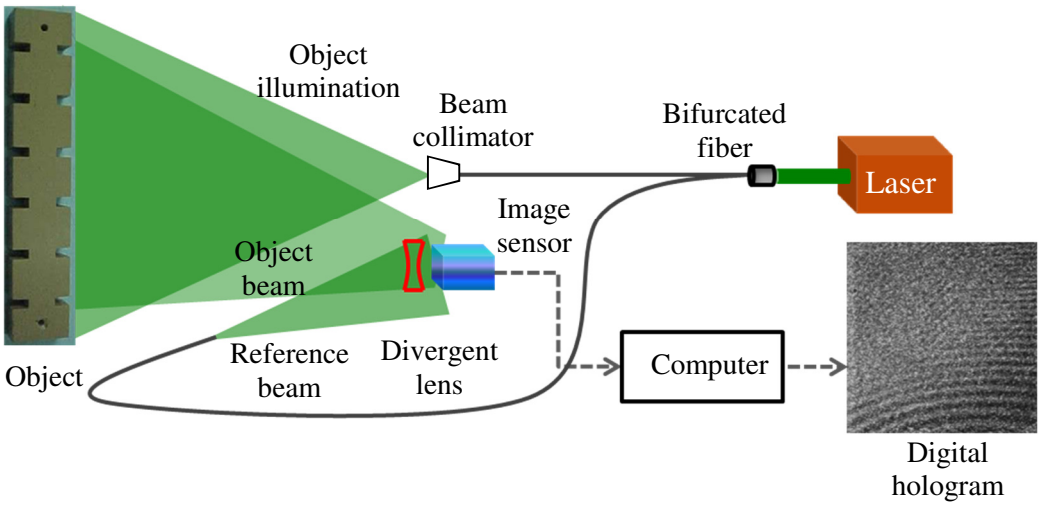

Figure 2.1 All-fiber off-axis hologram recording setup

In this study, Verdi 6W continuous wave laser was used at a maximum power level of 1W. The expanded beam from one fiber end is directly used as reference beam and beam from the other fiber end is taken through a collimator to control the intensity and area of coverage for object illumination. CMOS image sensor of make PixeLINK, Germany with 6-megapixel resolution and 3.45 µm pixel size was used for recording the digital hologram. A divergent lens as proposed by Schnars (1996) with normal illumination and observation direction is used to satisfy the sampling criteria given by Equation (1.3). Figure 2.2 shows the front panel of numerical reconstruction software developed for the present study. The software was developed in LabVIEW. The software has two display windows. One window displays live hologram which is direct sensor output. This live display of digital hologram helps to record a proper hologram, through controlling the intensities of reference and object beams and also the sensor parameters like exposure time and brightness. The second window displays the reconstructed time average holographic images. Provisions to control the camera and reconstruction parameters

are provided in the front panel. Numerical reconstruction of the digital hologram can be carried out in real time and can be saved in video format using this software. Provision to feed the reconstruction parameters, like wavelength of laser, pixel size and distance between sensor and object, t used in the Equation 1.8 is also provided.

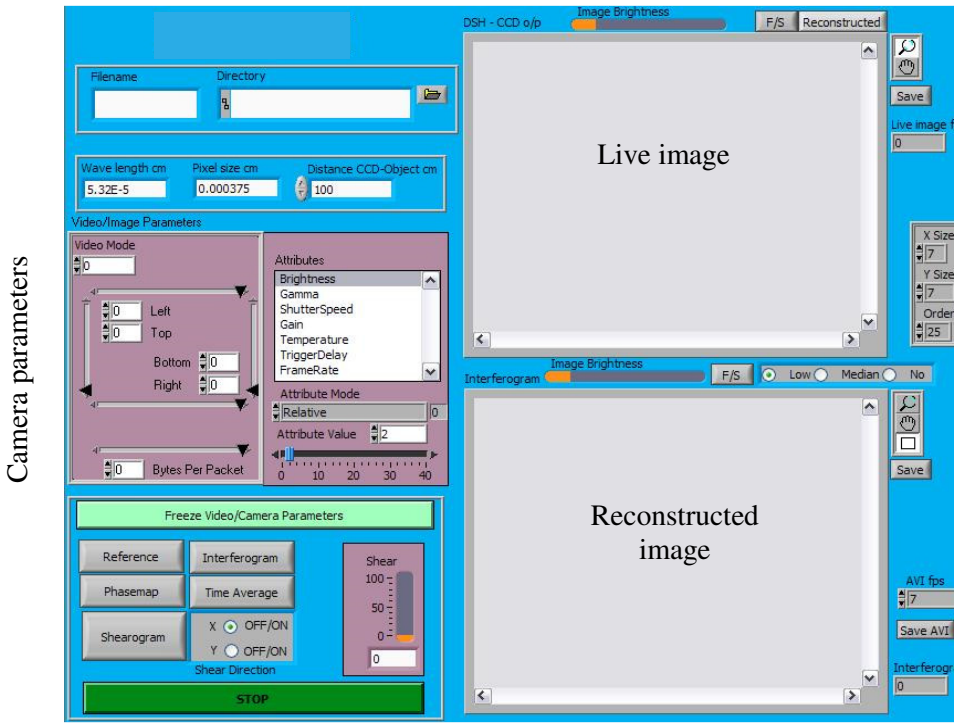

Figure 2.2. Front panel of real-time numerical reconstruction software

2.2.1 Vibration stressing

A piezo actuator is used for vibrating the object. The piezo actuator is a high voltage device requiring high voltage amplifier. Maximum power, force and acceleration are functions of frequency and depend on the transfer function of the amplifier as well as on the piezo-crystal material and number of layers per stack. Piezo shaker system of make M/s isi-sys, Germany used in the present study is shown in Figure 2.3. Piezo shaker is mounted on the object surface using a vacuum adaptor. A vacuum pump is connected to the vacuum adaptor. The excitation frequencies are generated by a function generator and controlled via software. The function generator is an external USB wave generator device connected to the USB port of computer. The output from the wave generator is fed to the dual channel bipolar

amplifier which in turn connected to the piezo shaker. Different type of waveforms can be generated using a function generator. Moreover, the amplitude level of the excitation can also be controlled through the software. Provisions to give a frequency sweep with start frequency, end frequency and frequency step are also available with this system.

Figure 2.3. Photograph of piezo shaker mounted with vacuum cup

2.2.2 Validation Experiments

To validate the optical setup and reconstruction software, time average holograms of an Aluminium plate during a frequency sweep were recorded and the fringe patterns were compared with contours of out of plane displacement response, obtained through a frequency response analysis using finite element method at respective frequencies. The photograph of the experimental setup and piezo shaker mounted on the plate are shown in Figure 2.4 (a) and 2.4 (b) respectively.

(a)

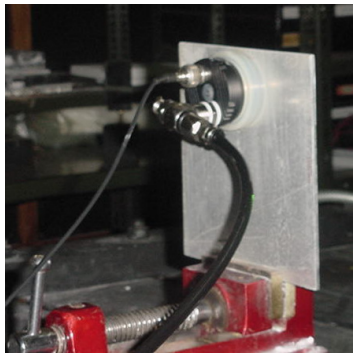

(b)

Figure 2.4. Photographs of (a) experimental setup (b) piezo shaker mounted on the top edge of plate with its bottom edge clamped in a vice

The plate was clamped at one edge as a cantilever and vibrated using a piezo shaker at top edge. The frequency of vibration was swept from 0 Hz to 20 k Hz. Frequency response analysis of a cantilever plate was carried out using (FEAST^{SMT}, 2018), ISRO's structural analysis software based on FEM, and contours of vibration amplitudes at four typical frequencies are compared with time average fringe patterns and their shapes are in good agreement as shown in Figure 2.5. The displacement response obtained at respective frequencies can be used as an input to the intensity Equation (1.17) to simulate realistic fringes as explained in Section 3.3

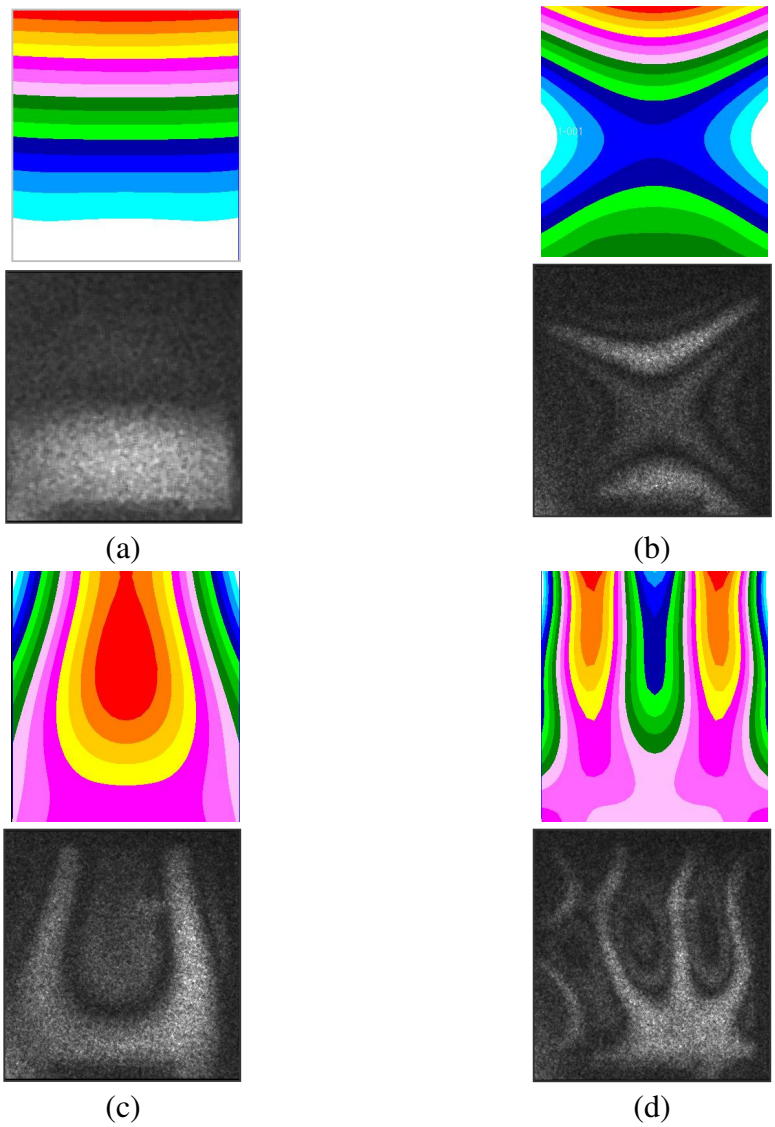

Figure 2.5 Displacement response through FEM vs. experimental time average interferograms at frequencies(a) 100 Hz (b) 540 Hz and (c) 820 Hz (d) 4040 Hz

The vibration nodes are regions with the brightest fringe and are coincided with regions of zero displacement response in the numerical plots.

2.3. Results and discussion

A flat honeycomb core sandwich panel with a programmed debond was tested to obtain the resonance frequency of the debond region for flat specimens. Figure 2.6 (a) shows the photograph of a flat sandwich specimen with shaker mounted on the top edge. Frequency was swept upto 25 kHz. Figure 2.6 (b) shows the 2nd bending mode of the specimen at low frequency of around 1 kHz. Debonds are not locally resonating at this frequency. The bright fringes at the middle of the specimen indicate the node location where the vibration amplitude is zero. During the frequency sweep, the debonded regions start locally resonating at frequency of around 8 kHz and up to a frequency of 10 kHz as shown in Figures 2.6 (c) and 2.6 (d). The debond regions are marked with dotted rectangles in the figures. The single fringe corresponds to the vibration amplitude of about 0.1 µm. The results indicate that time average holography is highly sensitive to vibration of very small amplitude and that the resonant frequency of debonded face sheet of flat panel is around 8 kHz to 10 kHz.

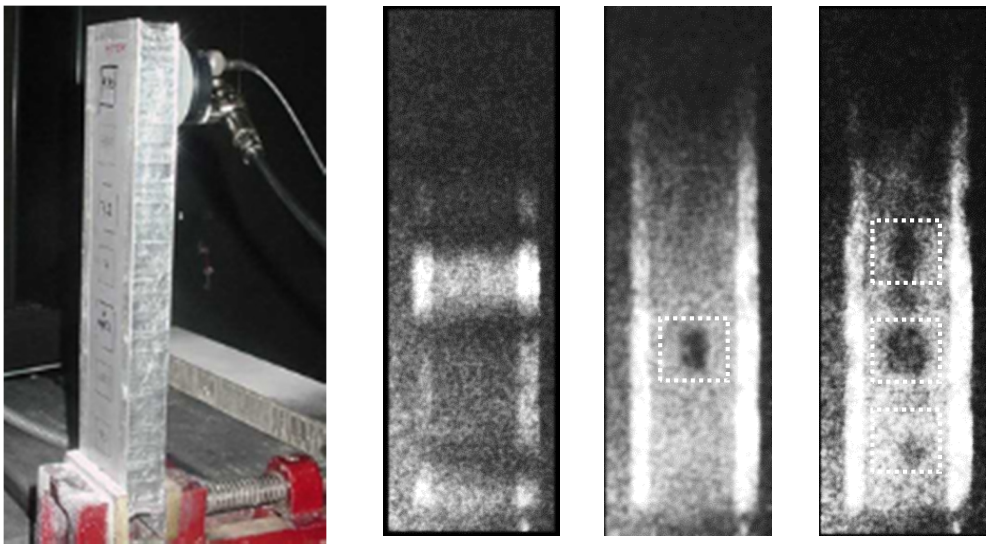

(a) (b) (c) (d)

Figure 2.6 (a) Photograph of flat sandwich specimen with shaker mounted on its top edge and time average interferograms at (b) 1 kHz (c) 8 kHz(d) 10 kHz

Time average holograms of a typical sandwich structure with curved edges were recorded during a frequency sweep and the experimental setup is shown in Figure 2.7. The region monitored is marked in dotted rectangle in Figure 2.7. Two typical

fringe patterns at frequencies 800 Hz and 8 kHz are shown in Figures 2.8 (a) and 2.8 (b) respectively. The first mode of vibration was around 800 Hz. At 8 kHz, fringe patterns were not visible. Hence this is an indication that the curved edges are free of any face sheet debond if its resonating frequency is same that of the debonded face sheet for flat constructions.

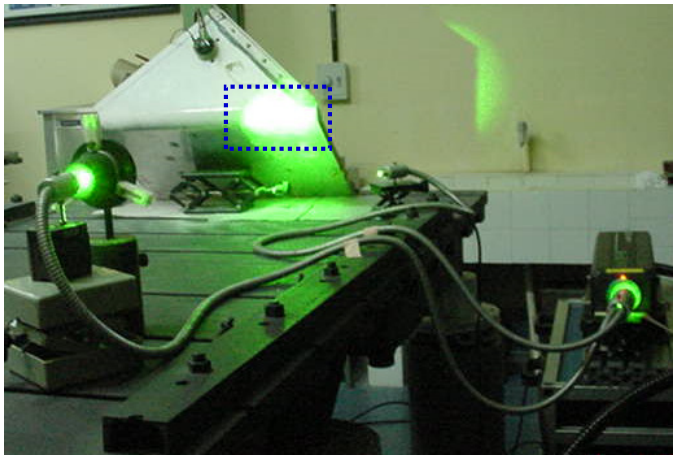

Figure 2.7 Photograph of the off-axis set-up

(a)

(b)

Figure 2.8 Time average interferograms of curved edge at frequencies (a) 800 Hz and (b) 8 kHz

To determine the effect of curvature on the vibration amplitude, displacement field and the resonance frequency of the debonded face sheet along a curved edge, a programmed debond was generated at one region on one curved edge. Debond was programmed at the curved edge, as marked in the photograph in Figure 2.9, through local heating of the face sheet by buffing operation which increased the temperature

sufficient enough to create a face sheet debond. Holograms were recorded during a frequency sweep for curved edges with and without programmed debonds.

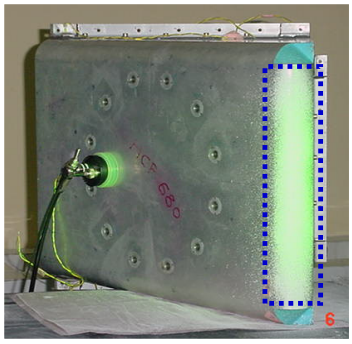

Figure 2.9 Photograph of sandwich construction with programmed debond at one of its curved edges

Time average holographic fringes at 800 Hz for a curved region with and without defect are shown in Figures 2.10 (a) and 2.10 (b) respectively.

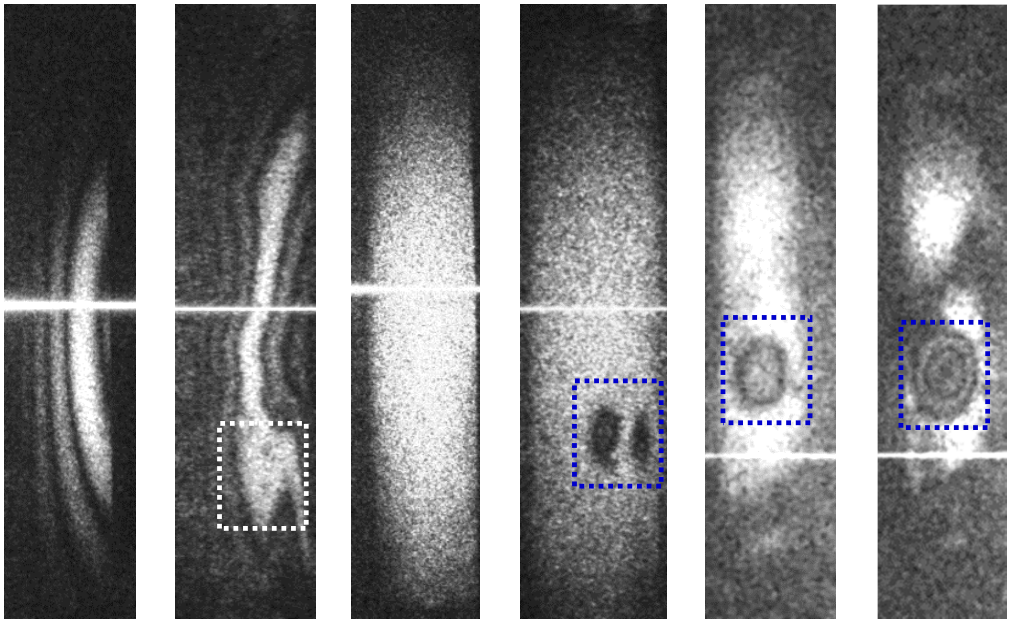

(a) (b) (c) (d) (e) (f)

Figure 2.10 Time average interferograms of the curved edge without debond at (a) 800 Hz (c) 8 kHz and with debond at (b) 800 Hz (d) 8 kHz and time average interferogram of another curved edge with debond at 8 kHz with piezo shaker excitation input of (e) 1 Volt and (f) 10 Volt

A local discontinuity was observed in the displacement field at the vicinity of the debonded region. Similarly, the time average fringe patterns at 8 kHz are shown in

Figures 2.10 (c) and 2.10 (d) respectively for the curved region with and without debond. At 8 kHz, fringe patterns were not visible for a perfectly bonded curved edge, whereas debonded face sheet at the curved edge shows resonance depicted by fringes with vibration amplitude of approximately 0.1 μm. The behaviour of the debonded face sheet is similar for both flat and curved surfaces. To validate this dynamic response, time average hologram of another curved edge with programmed debond was recorded at 8 kHz as shown in Figure 2.10 (e). Moreover, the magnitude of excitation was also increased by applying 10 Volt to the piezo shaker. An increase in the response of the defective region was observed, which is depicted by more number of fringes as shown in Figure 2.10 (f). Since the time average fringes due to local resonance are confined to only the debonded region, the quantification of the size of debond is also possible from the respective fringe pattern.

2.4. Conclusion

Sandwich structures with edges having high curvature under forced vibration were studied using time average digital holography. Dynamic displacement responses of the curved edges with and without programmed debonds were mapped under a sinusoidal frequency sweep. It is observed that the debonded face sheet resonates at the same frequency irrespective of flat or curved sandwich construction. Thus the feasibility of using time average digital holography for the inspection of curved sandwich construction is established.

CHAPTER 3

TIME AVERAGE DIGITAL HOLOGRAPHYWITH SQUARE WAVE EXCITATION

3.1 Introduction

With the advancement of digital holography, industries started employing double exposure method of digital holography as an NDT tool due to its high sensitivity, whole field nature and less environment stability requirement to levels comparable to commercial electronic speckle-based systems(Thomas and Pillai, 2009; Thomas et al., 2007). The use of thermal and mechanical stressing for defect detection in various thermal protection systems and aerospace structures has been well documented (Thomas et al., 2007; Ferraro, 1991). However, the practical difficulties in ascertaining the requirement of uniform thermal stressing for repeatability of results, rigid body movement in an industrial environment during double exposure method, and poor defect detection capability in a sandwich structure with metallic skin sheets limit the application of thermal stressing in the shop floor. For inspection of huge honeycomb core sandwich structures like payload fairings and equipment bay decks in satellite launch vehicles proper selection of stressing method is required which can be applied to a large area with repeatability in terms of stressing magnitude and point of application. This paves way to dynamic excitation and therein time average method of digital holography. The single exposure time average method is an added advantage to stability requirement where in other stressing methods like vacuum and thermal require a stable environment between two exposures. However, time average digital holography (TADH) conventionally uses sinusoidal frequency sweep to identify and characterize the local defects in a component. The practical difficulties in the implementation of TADH technique for the inspection of bonded structures are addressed in this study. The issues with the identification of defects from the

complex fringe pattern due to overlay of global and local modes, time-consuming frequency sweep in search of local resonances and high sensitivity of the fringe pattern to the amplitude and location of the point of excitation are highlighted in the Section 3.2. Subsequently, a novel excitation strategy is proposed for characterization of defects, which overcomes the prevailing issues, including that of random vibration. Extensive experiments were conducted to validate the new approach. It is noticed that the proposed methodology is much faster and economical for the identification of defects.

3.2 Experimentation Details

As a case study, responses of non-defective and defective honeycomb sandwich panels are studied first through TADH with the conventional approach of inspection where the structure under test is excited through sinusoidal vibration and the time average hologram is recorded during a frequency sweep. Later the experiments were carried out with proposed scheme of excitation using the same test setup. In the present study, three flat sandwich panels of length 300 mm and width 100 mm were tested. Among these panels, one panel was in good condition or defect-free as shown in Figure 3.1 (a), whereas face to core debonds were programmed in the other two panels by removing the adhesive film at the locations as marked in Figure 3.1 (b) and 3.1 (c) respectively with one debond and two debonds.

(a) (b) (c)

Figure 3.1 Sandwich panels with (a) no debond, (b) one debond, and (c) two debonds

The sandwich panels were made of metallic honeycomb core of 20 mm thickness with two Aluminium face sheets of thickness 0.5 mm bonded on either side of the core with adhesive. Initially, vibration response of the good panel is mapped during a sinusoidal frequency sweep from 1 Hz to 10 kHz through TADH. The panel is clamped at the bottom for a length of 40 mm and is excited through forced vibration at the top using a piezo shaker mounted through a vacuum cup with excitation location at around 30 mm from the top of the panel as shown in Figure 3.2 (b).

(a)

(b)

Figure 3.2 Photographs of (a) off-axis digital holography setup and (b) excitation setup on the specimen

All experiments were conducted using VERDI-V6 continuous wave laser of Coherent Inc. and with a 6-megapixel monochrome CMOS (complementary metal oxide semiconductor) image sensor PL-B781F manufactured by PixeLINK. The photograph of the off-axis digital holography setup is shown in Figure 3.2 (a). The diverging beam from one fiber end was directly used as reference beam, whereas the beam from other fiber end was collimated for illuminating the object. Reference beam was kept near the object such a way that to satisfy both the sampling requirement and non-overlapping diffraction orders. Beam for illuminating the object was kept near the sensor to make sure, a normal illumination and recording

condition. Moreover, a divergent lens was kept in front of the image sensor, to record the entire test object from its virtual image of reduced size to overcome limited resolution of the image sensor (Schnars et al., 1996).

3.3 TADH under Sinusoidal Excitation

Typical time average interferograms (TAI) showing the response of the non-defective specimen at various frequencies are shown in Figure 3.3. Fringe patterns represent various vibration mode shapes of panel. Only one anomalous fringe was visible as marked in Figures 3.3 (e) and 3.3 (f). This location is exactly opposite to the excitation point where the piezo shaker was mounted.

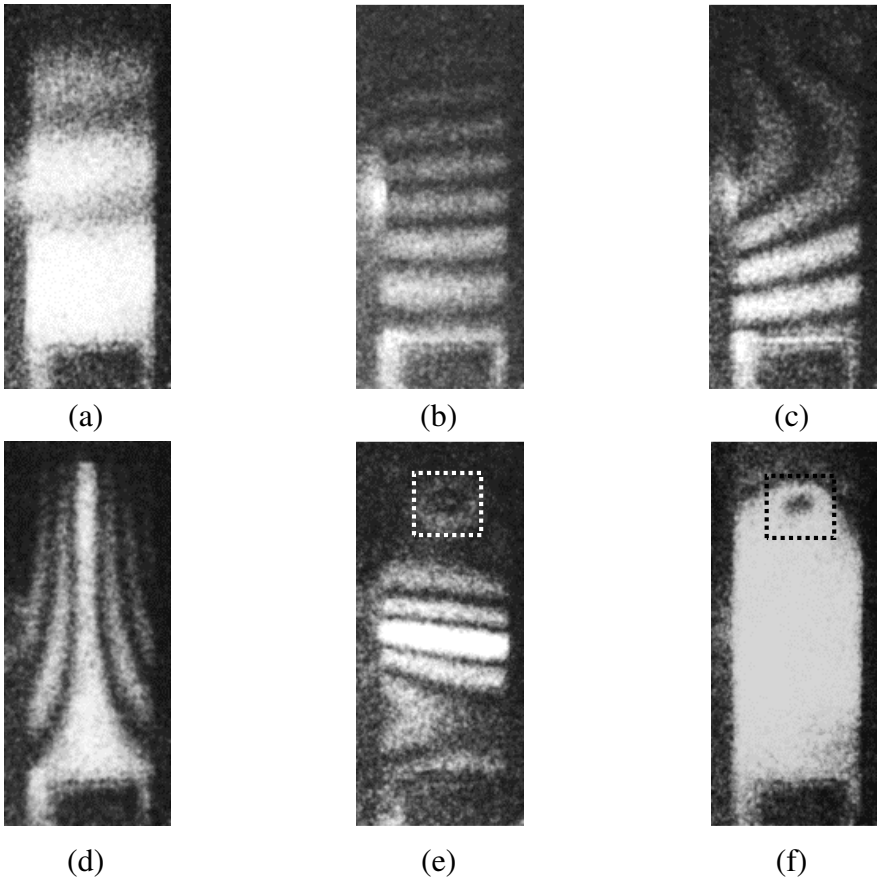

Figure 3.3 TAI of good panel at frequencies (a) 50 Hz, (b) 200 Hz, (c) 800 Hz, (d) 1000 Hz, (e) 2365 Hz, and (f) 6000 Hz

Likewise, two representative TAI each at 90 Hz and 1000 Hz for all the three panels recorded under sinusoidal excitation are shown in Figure 3.4. There are no

significant demarcations between the fringe maps in the case of defective and non-defective panels.

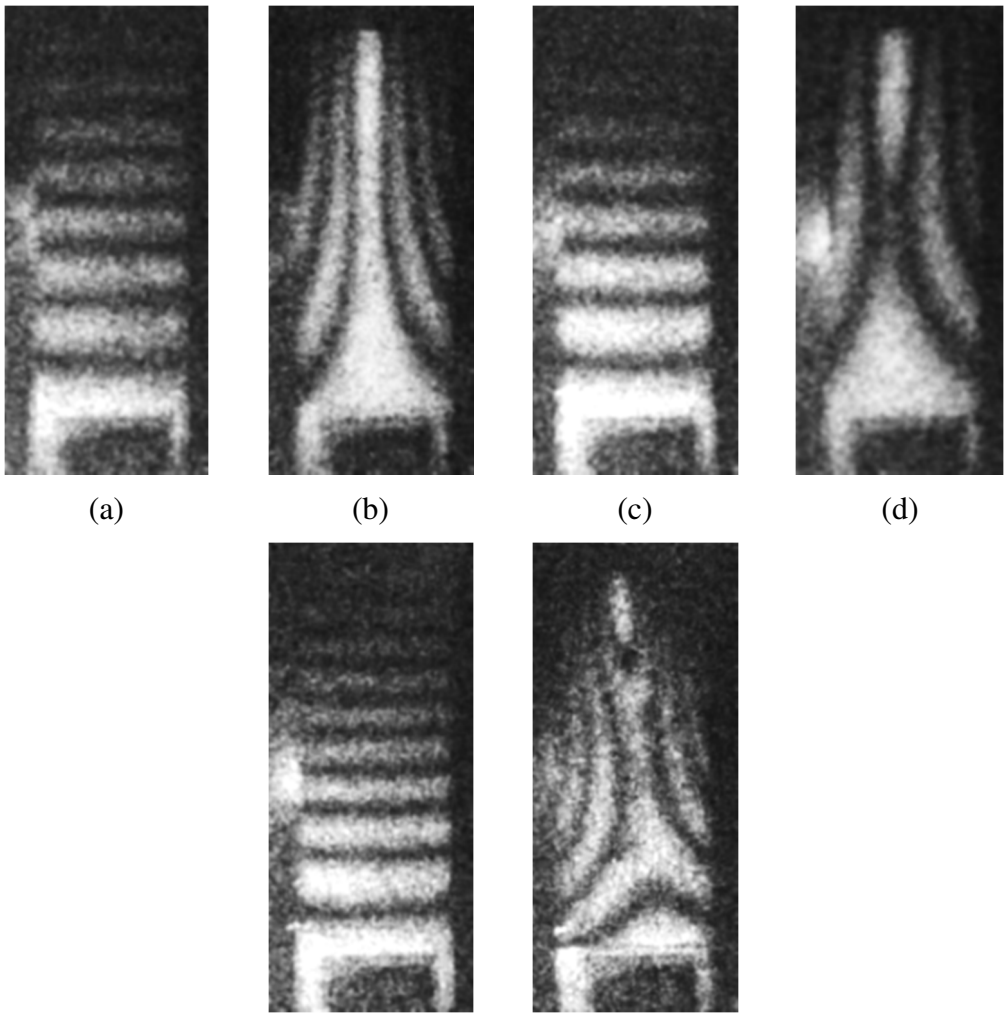

Figure 3.4 TAI of good panel at (a) 90Hz, (b) 1000 Hz, panel with one debond at (c) 90 Hz, (d) 1000Hz, and panel with two debonds at (e) 90Hz, (f) 1000Hz

Similarly, the TAI of the good panel for different magnitudes of excitation amplitude at a frequency of 800 Hz are shown in Figure 3.5 and that for the panel with two defects at 6000 Hz are shown in Figure 3.6. As expected the dynamic response of the total panel increases with excitation magnitude as indicated by the increase in fringe density. The responses of the defects in Figure 3.6arealso gets amplified with increasing excitation. It is observed that the response of bottom debond is more when compared to that of top debond for small excitation magnitude

as indicated by one fringe in Figure 3.6 (b). The magnitudes of sinusoidal excitations are given at the bottom of respective interferograms.

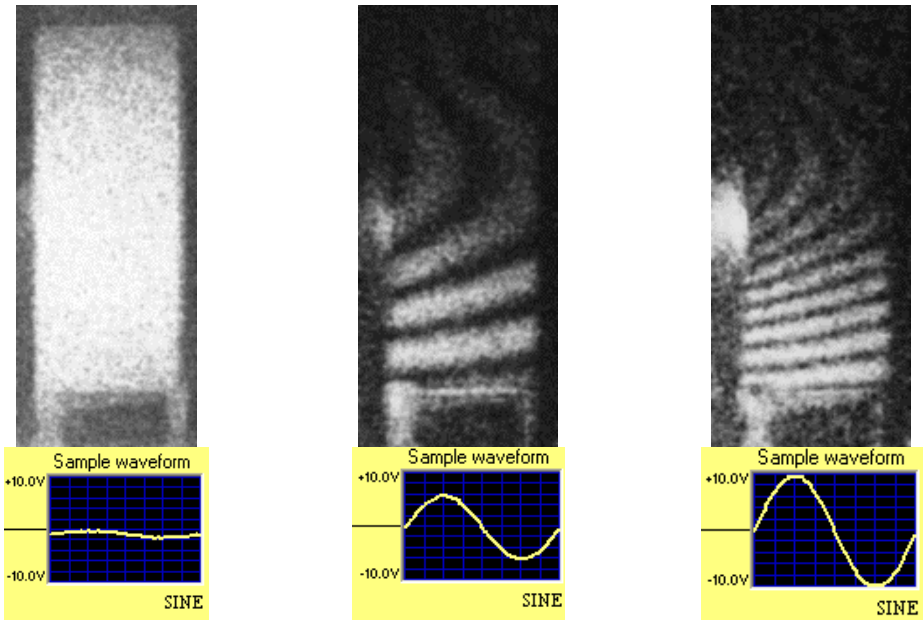

(a) (b) (c)

Figure 3.5 TAI of the good panel at 800 Hz with piezo shaker excitation input of (a) 1 V, (b) 6 V, and (c) 10 V

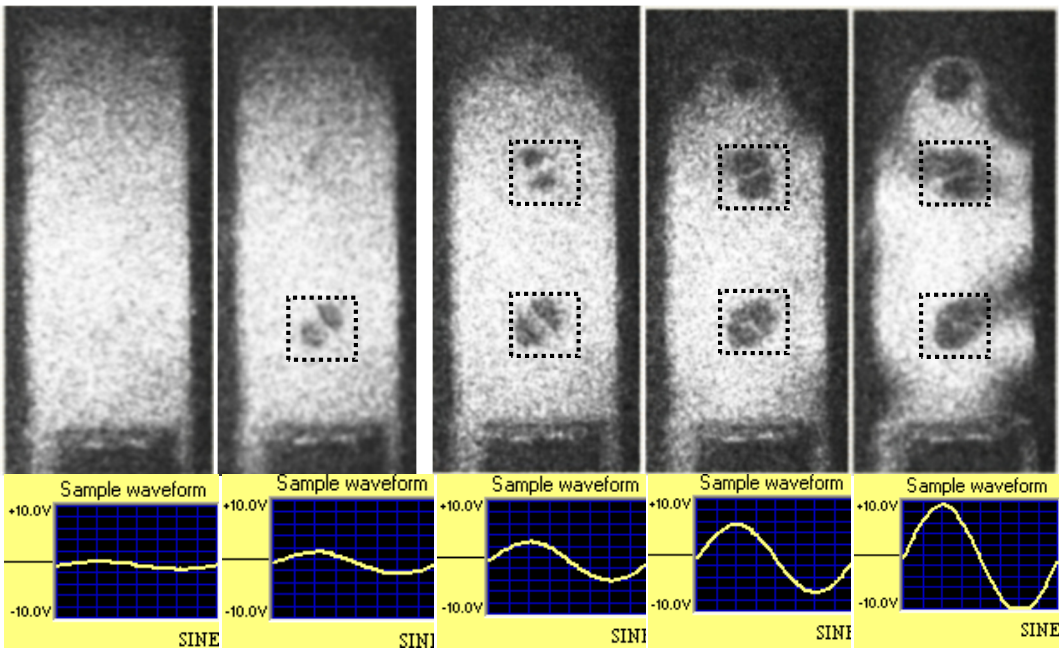

(a) (b) (c) (d) (e)

Figure 3.6 TAI of the panel with two defects at 6000 Hz with piezo shaker excitation input of (a) 1 V, (b) 2 V, (c) 4 V, (d) 6 V, and (e) 10 V

The location of excitation was also changed for a particular frequency of 800 Hz with the point of application at a distance of 60 mm, 120 mm and 180 mm from the clamped edge. TAI for the panel having one defect are shown in Figure 3.7. The anomalous fringe pattern as marked in Figure 3.7 (a) corresponds to the excitation point. Here the local modes are overlaid with the global modes.

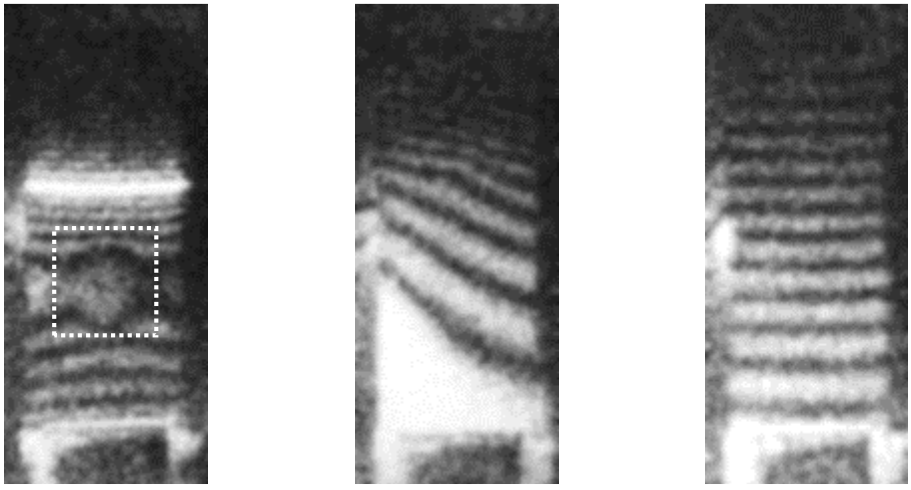

(a) (b) (c)

Figure 3.7 TAI of the panel with a single debond at 800 Hz with point of excitation at (a) 60 mm (b) 120 mm and (c) 180 mm from the clamped edge

From all the above interferograms it is clear that the response mapped through time average method is highly sensitive to the frequency, amplitude and point of excitation. Similarly, the global modes are very complex and superimposed with the local response of defects which makes the defect identification difficult, hence decreasing the confidence level of defect identification. Moreover, at each frequency, both the magnitude and point of excitation has to be changed to determine optimum values of these parameters for defect identification. Moreover, the component has to be excited for a wider frequency range to identify other defects such as core compression, inclusions, delamination of composite face sheets and the debond near inserts which are having a broad range of dynamic response. All the above issues result in a time-consuming inspection of a component through TADH. The frequency at which the debonds resonate and the excitation magnitude which is sufficient enough to produce one fringe, obtained through different sets of frequency sweep at different excitation were 6 kHz and 6 V respectively.

3.4 Simulation of TADH under Sinusoidal Excitation

A frequency response analysis of a sandwich honeycomb specimen with and without debonds is carried out numerically using (FEAST, 2018), to capture the effect of debond on the local and global responses during a sinusoidal frequency sweep. Time average holographic fringe patterns were plotted using the out of plane displacement response from the above analysis and substituting for*d* in the Equation (1.17). Three-dimensional finite element model of honeycomb core sandwich specimen with dimensions same as that of specimens used in experiments was used for analysis. Four-node linear shell elements were used to model both the honeycomb core and face sheets. Figures 3.8 (a) and3.8 (b) show the plan and side views of the model. The fixed end boundary condition and the location of the vibration excitation are shown in Figure 3.8 (b).

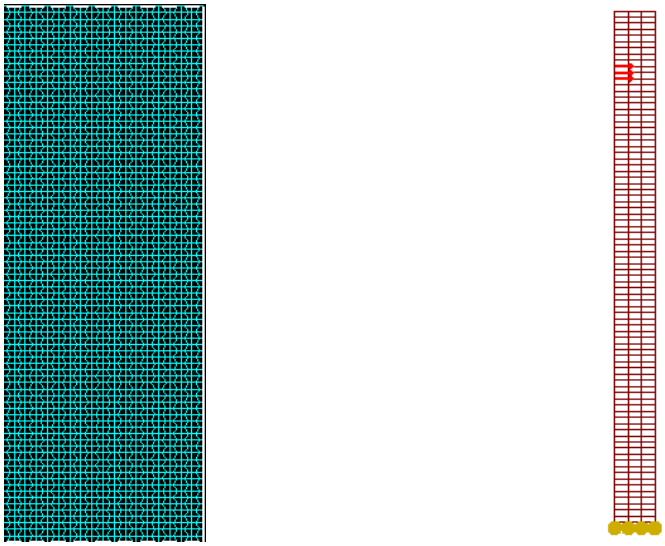

(a) (b)

Figure 3.8(a) Finite element model of the honeycomb core specimen (b) side view showing boundary condition and excitation location

The 3D honeycomb core is modeled with three elements in the thickness direction as shown in the cut view of the 3D model in Figure 3.8 (a). The face sheet debond is modeled using double node approach (Marshall, 1991; Burlayenko and Sadowski, 2010). The elements on the face sheet where debond is to be created are modeled with double nodes thus fully separating the face sheet from the honeycomb

core. The debonded regions are shown in Figure 3.8 (b). The location and size of the debond regions are same as that of debonds programmed in the specimens used for the experiments. The responses of the node number 11316 at the center of the bottom debonded region on the face sheet of both non-defective and defective panels were extracted after the analysis. Procedure proposed by Burlayenko and Sadowski, (2012) can be followed for better simulation of debonded face sheet.

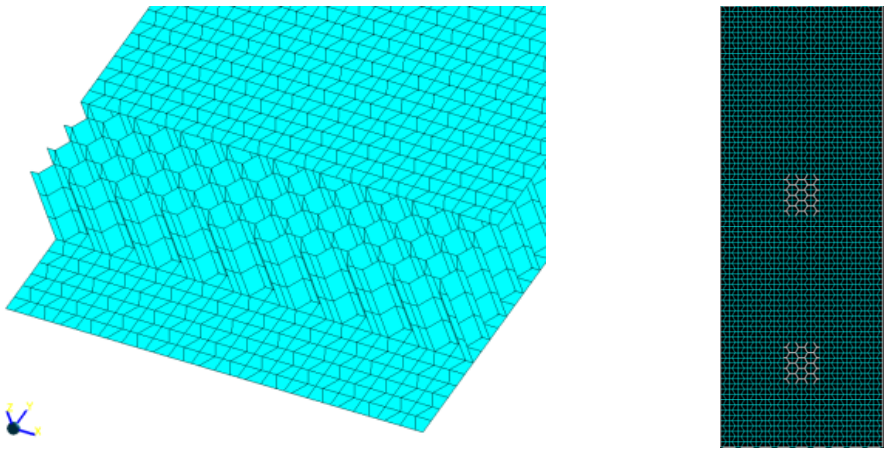

(a) (b)

Figure 3.9(a) 3D view of the model (b) FE model showing debond regions

The frequency response curve for node 11316 of a defective panel and good panel are respectively shown in Figure 3.10 and Figure 3.11. Comparing the out-of-plane displacement response, the vibration amplitude of the debonded face sheet is more at higher frequencies of around 3 kHz, 6 kHz and 7 kHz as marked in Figure 3.10.

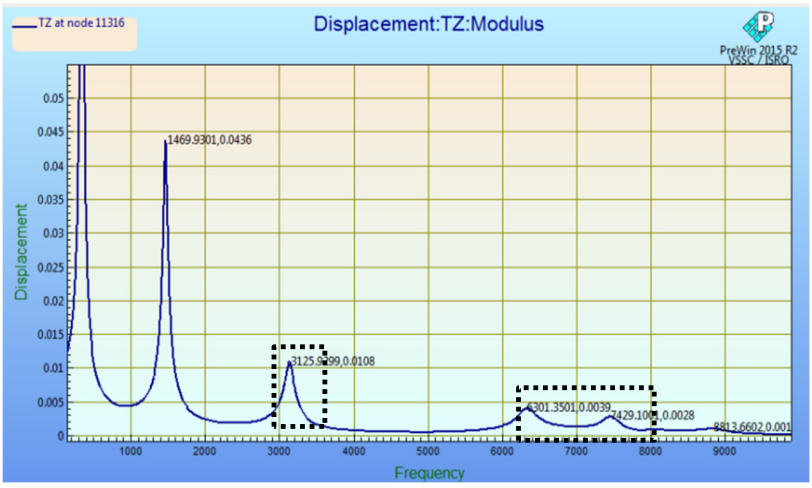

Figure 3.10 Displacement response at node 11316of defective panel

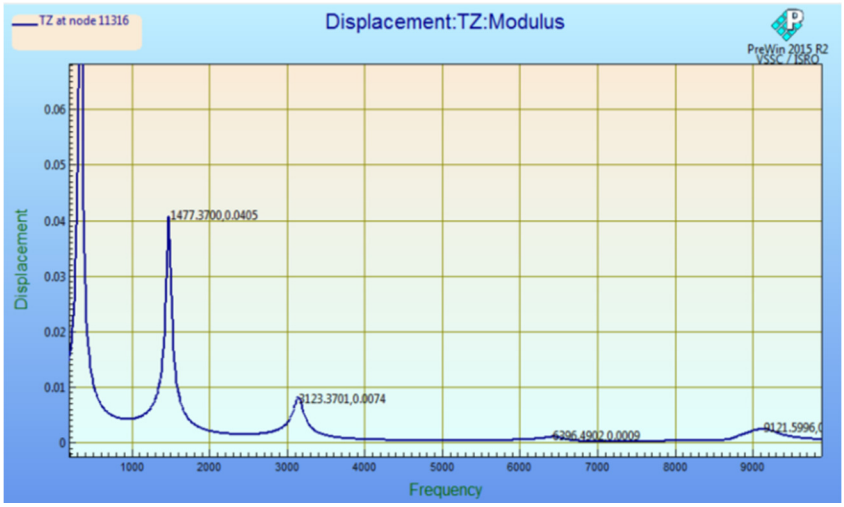

Figure 3.11 Displacement response at node 11316of non-defective panel

Simulated time average holographic fringes are plotted using this displacement response as an input to the Equation (1.17) for the good and defective panels with multiple debonds at two typical frequencies of 800 Hz and 5600 Hz are shown in Figure 3.12. Debonded face sheets have less response at 800 Hz and large response at 5600 Hz. Moreover, at 800 Hz the local and global modes are superimposed. The anomalous fringe pattern marked in Figure 3.12 (d) is similar to fringes observed in experiments (Figure 3.6). A few fringes due to the global response of the structure and point of excitation are also accompanied with the anomalous fringes.

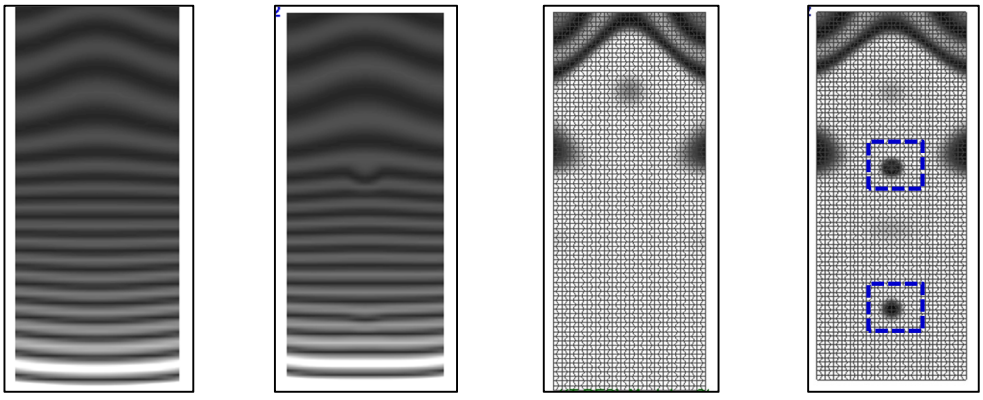

(a) (b) (c) (d)

Figure 3.12 Simulated time average holographic fringe pattern of good panel at (a) 800 Hz (c) 5600 Hz and defective panel at (b) 800 Hz (d) 5600 Hz

Similarly, the responses of the defect for different excitation magnitude at 5600 Hz were also determined for panel with one debond and the respective simulated time average fringe patterns are shown in Figure 3.13. The global and local displacement

responses of debonded region (marked in dotted rectangle) are found increasing with the excitation magnitude, in line with the experiments (Figure 3.5). The point of excitation visible as single fringe at higher frequency (Figure 3.13 (c)) is comparable with fringes in Figure 3.3 (f).

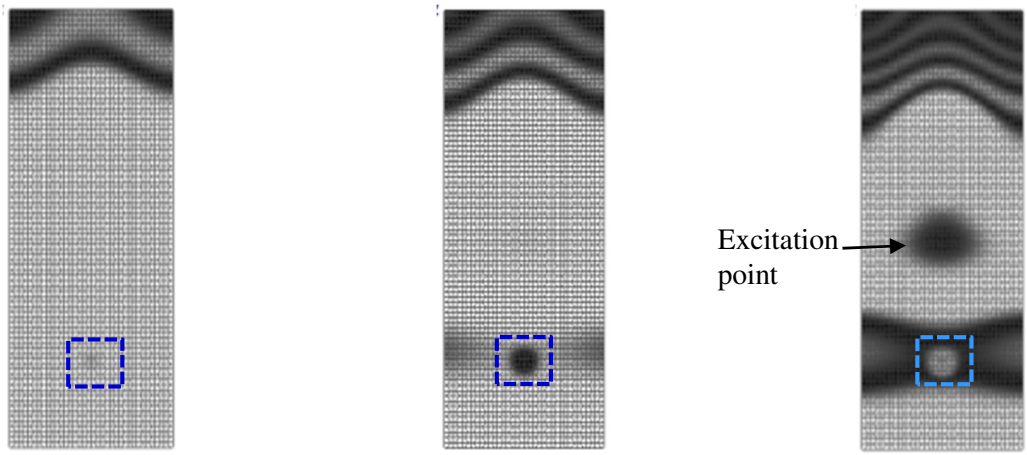

(a) (b) (c)

Figure 3.13 Simulated time average holographic fringe pattern of a panel with one debond at 5600 Hz for (a) small (b) medium and (c) large excitations

3.5 TADH with Periodic Non-Sinusoidal Excitation

A few problems involving accurate identification of defects using conventional sinusoidal excitation are also addressed by (Hung et al., 2000b) and a solution is proposed with the use of multi-frequency sweep to detect defects using time-integrated shearography. In their approach interferograms correspond to excitation at individual frequencies are again recorded during a frequency sweep and then these images are combined to generate a final interferogram for identifying defects. Again like the conventional approach, time-consuming frequency sweep cannot be avoided.

Figures 3.14 and Figure 3.15 show the simulated time average fringe patterns of a good panel and defective panel at four typical frequencies. The frequencies are selected in such a way that, these are the first four harmonics of a

periodic square wave signal of 800 Hz. It can be seen that the fringes become visible at both debond regions at higher frequencies as clearly depicted in Figure 3.15 (d).

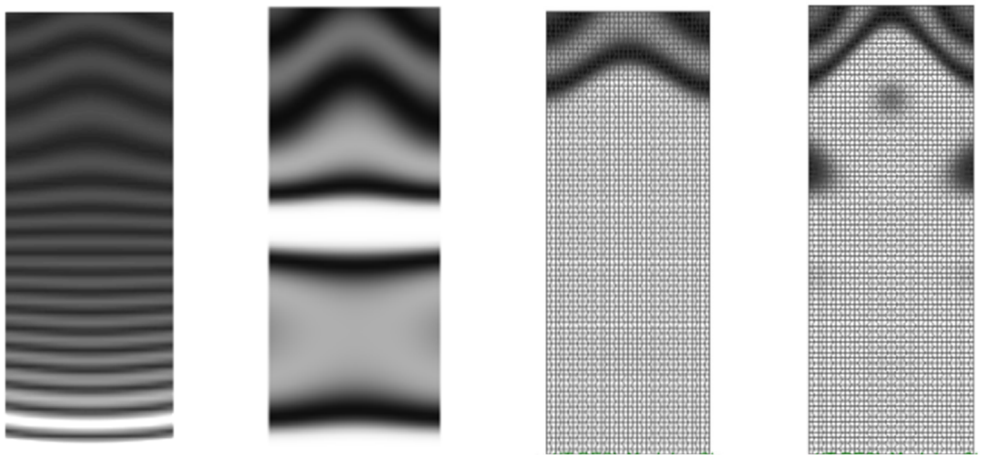

(a) (b) (c) (d)

Figure 3.14 Simulated TAI of a good panel at frequencies (a) 800 Hz (b) 2400 Hz (c) 4000 Hz and (d) 5600 Hz

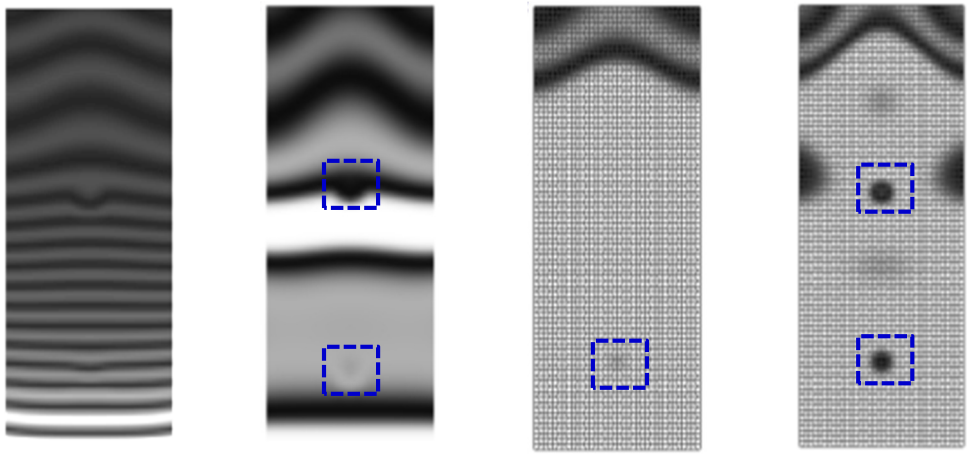

(a) (b) (c) (d)

Figure 3.15 Simulated TAI of a defective panel at frequencies (a) 800 Hz (b) 2400 Hz (c) 4000 Hz and (d) 5600 Hz

In line with these observations, an approach based on the vibration of an object simultaneously at several frequencies is used to improve the qualitative results of the conventional time average digital holography. This is achieved by the application of square wave excitation at a single frequency instead of single frequency sinusoidal excitation. Then the time average holograms are recorded during such an excitation to study the response of defective components. The theoretical basis for the proposed methodology is explained below.

Consider the equation of motion for a single degree of freedom system as given by Equation (3.1) (Mukhopadhyay, 2008).

$$m\ddot{u}+c\dot{u}+ku=F(t) \tag{3.1}$$

where m, c and k are the mass, damping and stiffness of the system respectively, $F(t)$ is the forcing function and $\ddot{u}$ and $\dot{u}$ are the second and first derivative of the displacement u. In conventional approach, the forcing function is given as $F(t)=A\sin(\omega t)$, where A is the amplitude and ω is the frequency of excitation. The steady-state response of such a system is given by Equation (3.2) (Mukhopadhyay, 2008).

$$u = \frac{\frac{A}{m}}{\sqrt{\left(\frac{k}{m}-\omega^2\right)^2+\left(\frac{c}{m}\omega\right)^2}}\sin(\omega t) = d\sin(wt) \tag{3.2}$$

where d is the amplitude of vibration used in the intensity equation for time average interferogram given by Equation (1.17).Any periodic non-sinusoidal signals can be considered as a summation of a large number of sinusoidal components when expanded as a Fourier series. An odd periodic square wave function at 800 Hz having unit excitation amplitude is shown in Figure 3.16and its spectrum gives the magnitude of the sinusoidal components of the forcing function for odd multiples of 800 Hz as shown in Figure 3.17.

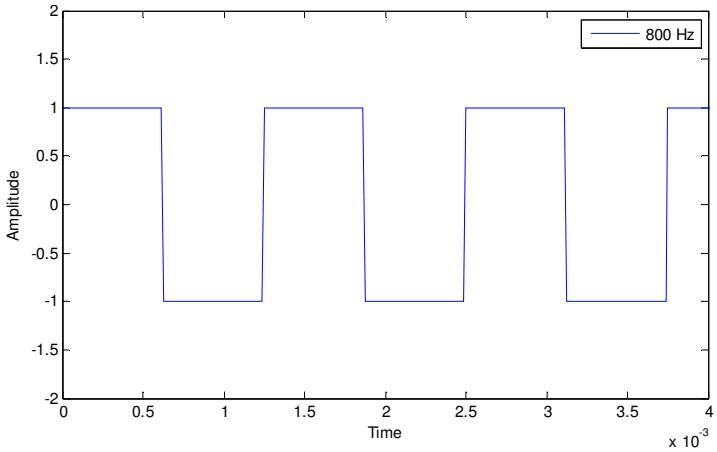

Figure 3.16 Odd periodic square wave function at 800 Hz

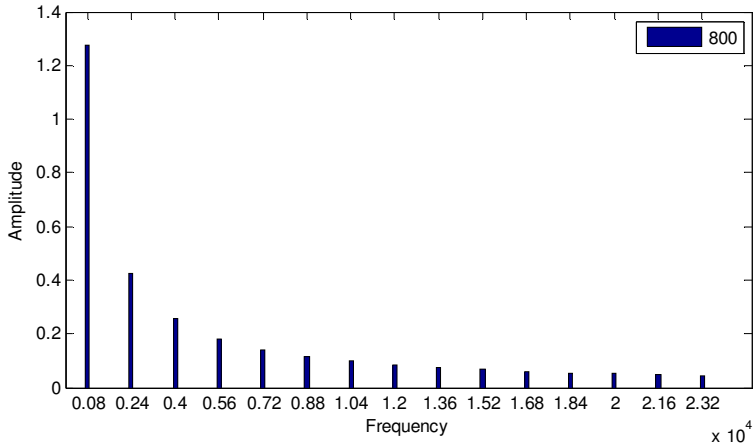

Figure 3.17 Response spectra of the square wave function

The Fourier series representation of the square wave excitation is given by Equation (3.3) (Mukhopadhyay, 2008)

$$F(t) = \frac{4A}{\pi}\sum_{n=1,3,5\ldots}^{N}\frac{1}{n}\sin(n\omega t) \tag{3.3}$$

Then the steady-state response of Equation (3.1) with the above forcing function is given by Equation (3.4) (Mukhopadhyay, 2008)

$$u = \sum_{n=1,3..}^{N} u_n \sin(n\omega t) \tag{3.4}$$

where u_n is the amplitude of response of individual Fourier component. Finally, the phase of the object wave given in Equation (1.14) for square wave excitation becomes

$$\phi(x,y,t) = \sum_{n=1,3..}^{N} \phi_n \sin(n\omega t) = \frac{4\pi}{\lambda}\sum_{n=1,3..}^{N} u_n \sin(n\omega t) \tag{3.5}$$

Thus the characteristic function for time average holography for square wave excitation can be written using the infinite series solution of Equation (1.15). Substituting Equation (3.5) the characteristic fringe function becomes

$$M_c = e^{i\phi_0(x,y)}\sum_{m=1}^{M}\prod_{n=1}^{N} i^{l_{nm}} J_{l_{nm}}[\phi_n(x,y)]e^{-il_{nm}\theta_n} \tag{3.6}$$

However, simulation of fringe pattern under square or random excitations is compute-intensive using the above equation and is addressed in Chapter 5. Practically an object can be excited with multiple vibration frequencies when more than one shaker is used with independent input frequencies or with a random signal from a single shaker. However, with the use of a single square input frequency, an infinite number of odd periodic frequencies can be generated which is expected to excite the defect without any miss. This novel aspect of the square input signal is exploited in this thesis work for defect identification. It is worth mentioning that random vibration containing a predetermined bandwidth of frequencies has already been used for defect detection as reported by (Clarady et al., 1983). Certain aspects of the random excitation strategy are discussed below.

Clarady et al., (1983) were the first to propose the application of random excitation to detect debonded areas thereby reducing the number of holograms recorded. An experiment with the specimen mentioned in section 3.2 with two programmed debonds was conducted with random excitation. The time average interferograms for random forcing function using white noise random signal with 10 MHz bandwidth from a generic function generator is shown in Figure 3.18 (a). Even the resonance of the defect is within this frequency range, no anomalous fringe patterns were observed in this interferogram. Low response of the specimen is due to the distribution of input energy across the entire spectrum, so the amount of energy available for exciting any mode is statistically low. Hence, for a wider frequency range, the excitation force must be sufficiently large enough to get the defect response. Hence random signal with a frequency bandwidth of 5 Hz to 2000 Hz was applied using another sophisticated random vibration controller Leuven Measurement Systems Test.Lab from M/s Siemens PLM software. However, the response mapped through TADH in Figure 3.18 (b) indicates that the upper limit of frequency band should be more than the resonant frequency of defects for detecting them. The responses for random excitation in the frequency range 50 Hz to 3000 Hz at 5 g_{rms}, 10g_{rms} and 20 g_{rms} are shown in Figures 3.18 (c) to 3.18 (e) respectively. The response of debonds with superposition of global and local modes was noticed. Moreover, at high frequency range of 10 kHz to 60 kHz of random excitation since

most of the defects resonate at its higher modes; the vibration amplitude will be comparatively low, requiring more input power for a detectable response. Therefore, attempts for getting the defect response at lower frequencies below 1 kHz has been attempted in this work.

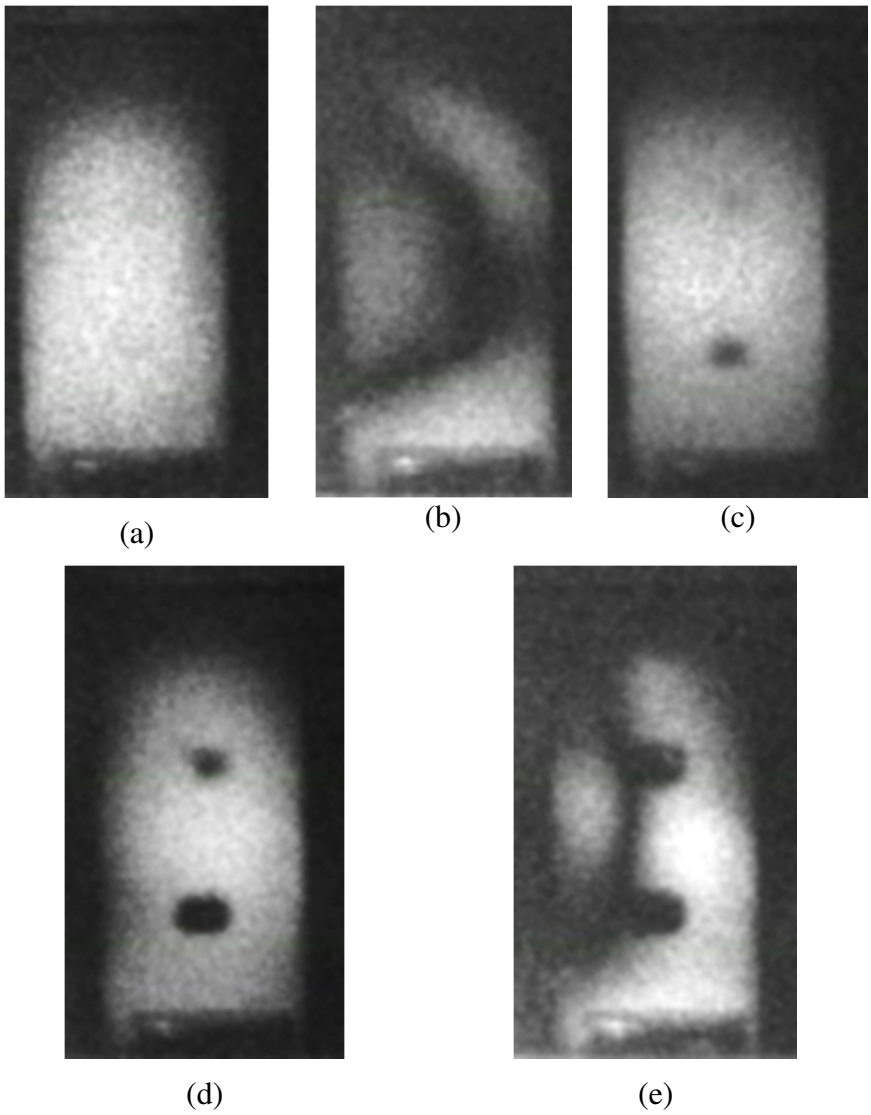

Figure 3.18 TAI of the panel with two defects under random excitation(a) white noise signal (b) 50 Hz to 2000 Hz, (c) 50 Hz to 3000 Hz with $5g_{rms}$, (d) 50 Hz to 3000 Hz with 10 g_{rms} and (e) 50 Hz to 3000 Hz with 20 g_{rms}

Generation of a random signal with a specified power spectral density and bandwidth is very complex and such a signal is not commonly available in standard signal or function generators. Towards this objective square wave excitation as demonstrated in this thesis would be preferable. Such an excitation can be achieved through a low-cost function generator having square wave output.

3.6 Results and Discussion

The three specimens mentioned in Section 3.2 were excited with square wave forcing function at different frequencies with different magnitude and excitation locations, and the dynamic responses were mapped using time average digital holography. Square wave forcing function was applied at the top edge of the specimen as shown in Figure 3.2 (b) using the piezo shaker and the bottom edge of the specimen was clamped in a vice. The displacement responses at 50 Hz, 200 Hz and 800 Hz were mapped to compare with the displacement responses obtained previously with sinusoidal excitation. Figures 3.19 to 3.21 show the responses of the specimens with single and multiple programmed debonds under square wave excitation. Figures 3.19 (a) to 3.19 (c) show the responses of the specimen with one debond closer to the shaker. Similarly to obtain the effect of debond away from the point of excitation, the specimen was rotated 180° to make the debond location near the clamped edge and the responses are shown Figures 3.19 (d) to 3.19 (f).

The response of the panel with multiple debonds under square wave excitation is shown in Figure 3.20. The newly proposed excitation strategy can provide the local response of the debonded region with TADH at a very low frequency of 50 Hz as compared to the sinusoidal excitation with a wider frequency band. Moreover, superposition of global modes could be avoided, when square wave excitation is used with proper tuning of the excitation magnitude. This process is less time consuming than frequency sweeping. For example, the first resonant mode of the debonded region with sinusoidal excitation was found around 3 kHz during a frequency sweep. A similar local resonance could be captured through square wave excitation at much lower input frequency. This is because one of the Fourier components of the square wave excitation was closer to the resonant frequency of the defect. Thus the sweeping of frequency is no longer required in search of local resonance of defective region. At one or two low frequencies, the magnitude of vibration can be tinkered in real time which would be sufficient enough to obtain fringes as shown in Figure 3.19 and Figure 3.20.

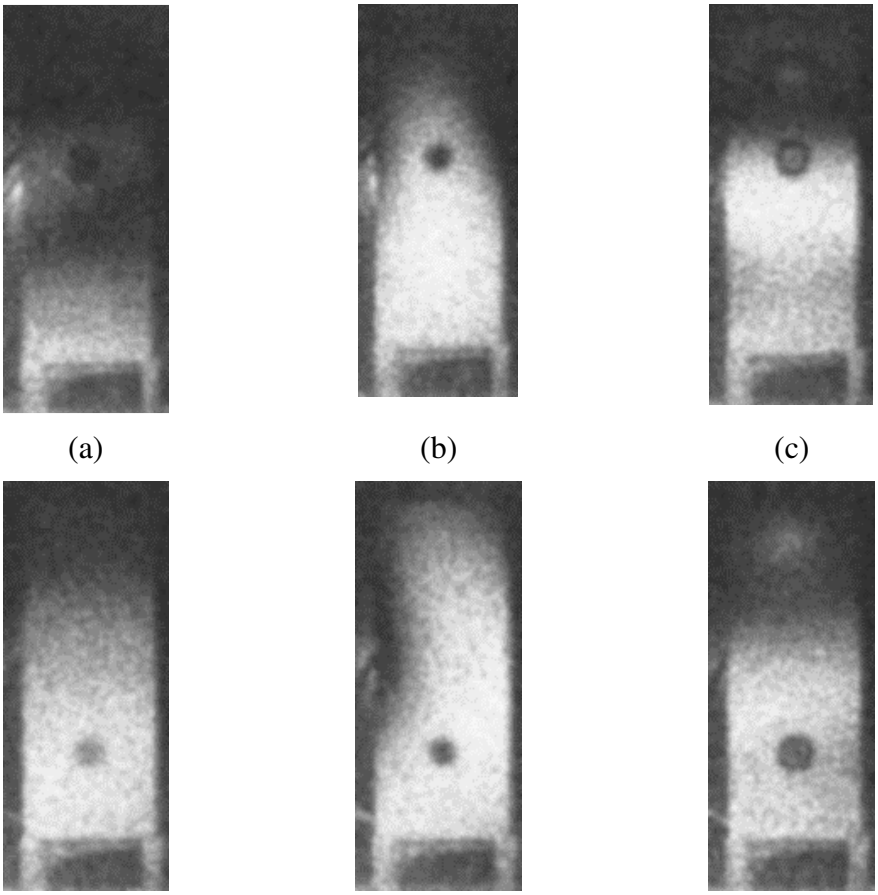

(a) (b) (c)

(d) (e) (f)

Figure 3.19 TAI of panel with top debond under square excitation at (a) 50 Hz and (b) 200 Hz (c) 800 Hz and bottom debond at (d) 50 Hz (e) 200 Hz (f) 800 Hz

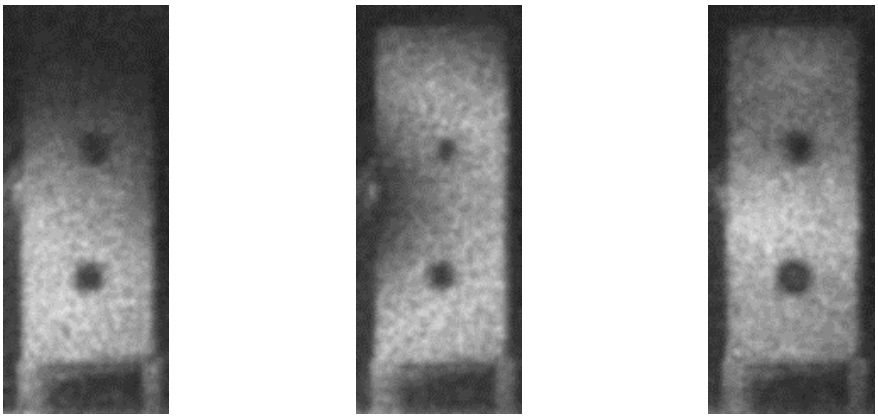

(a) (b) (c)

Figure 3.20 TAI of panel with multiple debond under square wave excitation at (a) 50 Hz and (b) 200 Hz (c) 800 Hz

The responses of the panel with single debond near the bottom clamp are shown in Figure 3.21 for different locations of square wave excitation. The time average fringe shown in Figure 3.21 (a) indicate 2nd mode of vibration of the debonded region due to higher excitation and lower damping when shaker is mounted closer to the debonded region.

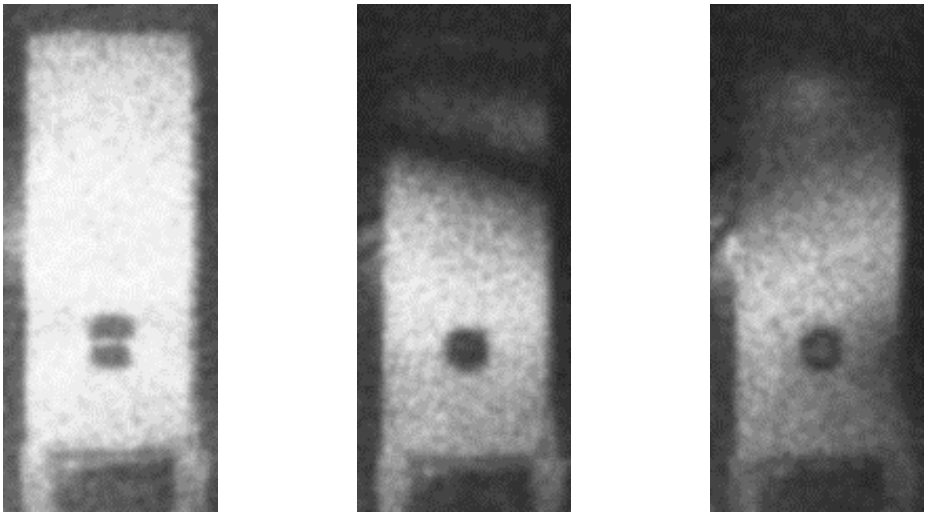

(a) (b) (c)

Figure 3.21 TAI of panel with debond near clamped edge under square wave excitation at 800 Hz with point of excitation at (a) 60 mm (b) 120 mm and (c) 180 mm from the clamped edge

3.7 Conclusion

This study demonstrates the capability of multi-frequency excitation of the object through square wave excitation in capturing the local response of defects present in an object with TADH. The resonance of debonded regions which occurs at higher frequencies can be mapped at a low frequency through the proposed method owing to the infinite number of Fourier frequency components resulting from square excitation. The conventional approach of inspection of adhesively bonded sandwich structures with time average mode of interferometry through sinusoidal excitation with wider frequency sweep or random excitation with predetermined frequency range can be replaced with square wave excitation to obtain better fringe response without superposition of global and local mode fringe patterns. The change in point of excitation also does not affect much on the local responses of the defects.

Moreover, TADH is implemented in real time as the stability requirement of this setup is very minimal, due to single exposure, and it does not require any reference state hologram. Thereby, time average digital holography with square wave excitation is a practical and faster tool for in-situ inspection of sandwich components.

CHAPTER 4

TADH OF POTTED-INSERT HONEYCOMB SANDWICH STRUCTURE

4.1. Introduction

Inspection of bonding of the face sheet in a potted-insert honeycomb core sandwich panel, using optical interferometry techniques like time-average holography or shearography, is different from those without inserts due to its complex response towards loading as demonstrated by Heimbs and Pein, (2009). Hence dynamic response of metallic honeycomb core sandwich structures with bonded and debonded inserts need to be mapped using time average digital holography to validate this technique. Moreover, the geometric and material discontinuities created by such inserts are very complex to simulate numerically (Burlayenko and Sadowski, 2014; Burlayenko and Sadowski, 2012; Heimbs and Pein, 2009). In the present study, these discontinuities were simulated using plates with multiple holes and with fully and partially bonded multiple local stiffeners and their dynamic behaviours were compared with the response of face sheet across inserts in a potted-insert sandwich structure. The results of the above study are applied for the inspection of passenger payload adaptor (PPLA) and are illustrated.

4.2. Experimental Details

In this study also time average digital holograms are recorded with a 6-megapixel monochrome CMOS image sensor of model PL-B781F by PixeLINK as explained in Section 3.2. All the interferograms presented in the results are as reconstructed without any filtering and post-processing. The intensity level of time average fringe patterns decreases with the number of fringes due to the property of Bessel function.

For better fringe visualization various post-processing functions like sigmoidal mapping function directly on the intensity map or low pass filtering on two orthogonal components of the reconstructed time average hologram can be used as reported in the literature (Matczak, 1994; Ragulskis et al., 2003). The experimental setup is same as explained in Section 3.2. VERDI 6 W laser of make M/s Coherent Inc, USA was used in this study. Similar to earlier experiments a bifurcated optical fiber was used to guide the laser beams for object illumination and for reference. The photograph of the off-axis digital holography setup is shown in Figure 4.1.

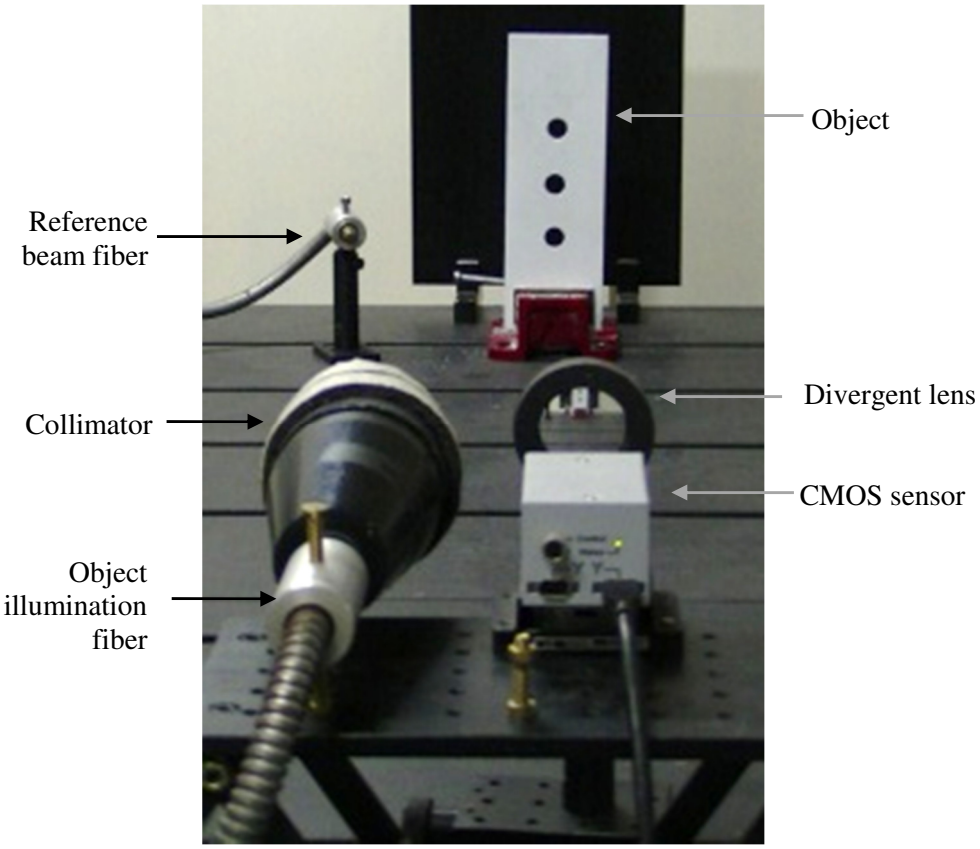

Figure 4.1 Photograph of the digital holography setup

4.2.1 Sandwich panel with collar inserts

Two honeycomb core sandwich specimens of size 200 mm × 200 mm with four post-bonded fully potted collar inserts were used in this study. The photograph of a specimen 1 without debond is shown in Figure 4.2.

Figure 4.2 Photograph of specimen 1

For post-bonding the inserts, the procedure as explained in Section 1.4 was followed. Specimen 1 was prepared using the standard procedure ensuring perfect bonding and specimen 2 was fabricated with programmed debond between the insert and face sheet. The bond line to be inspected is as marked in Figure 1.9. Metallic face sheets of 1 mm thickness were used. The top face sheet with visible inserts and the bottom face sheet with insert bond line to be inspected are shown in Figures 4.3 (a) and 4.3 (b) respectively.

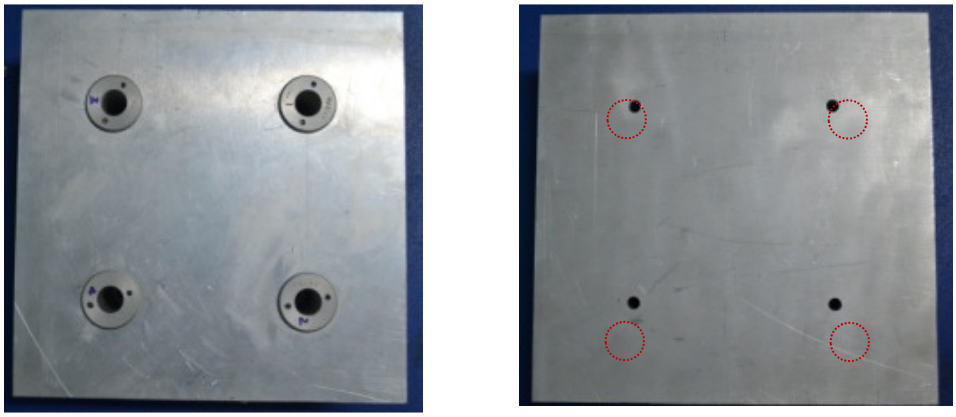

(a) (b)

Figure 4.3 Photographs of (a) top face sheet side and (b) bottom face sheet side of specimen 1

4.2.2 Plate with multiple holes and stiffeners

To understand the effect of geometric and material discontinuities due to metallic inserts on the dynamic behaviour of potted insert sandwich structure, the

operational deflection shape (ODS) of plate specimens with multiples holes and stiffeners under vibration excitation were studied. ODS is defined as the deflection of a structure at a particular frequency. Five plate specimens made of Aluminium material with size 300 mm × 100 mm and thickness 3 mm were used for the study as shown in Figures 4.4 (a) to 4.4 (e). Specimen P_1 is without any defect as a reference of the ODS, specimen P_2 with three holes to study the interaction of geometric discontinuity on ODS simulating the insert hole, specimen P_3 with three completely bonded local stiffeners of 20 mm diameter to study the effect of local change in stiffness on ODS simulating metallic inserts, specimen P_4 with two completely bonded stiffeners and a partially bonded stiffener to compare the local ODS with fully bonded stiffener and specimen P_5 with two stiffeners of 25 mm diameter with partial debond at the bottom insert to study the extent of debond. The stiffeners were made by bonding a 3 mm thick steel disc on the Aluminium plate to simulate the local stiffness ratio of 3 between them (Thomsen, 1998).

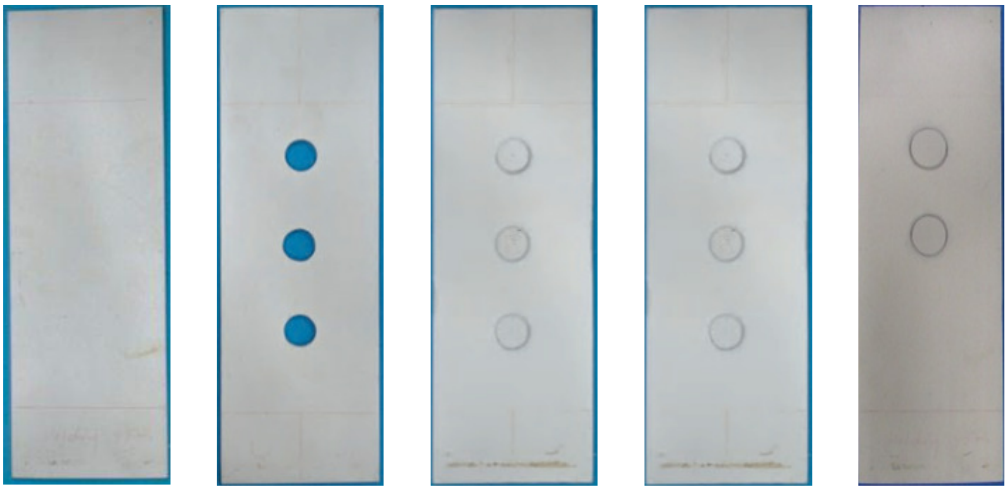

(a) (b) (c) (d) (e)

Figure 4.4 Photographs of plate specimen (a) P_1 without any defect (b) P_2 with multiple holes (c) P_3 with multiple stiffeners (d) P_4 with partially bonded top stiffeners (e) P_5 with partially bonded bottom stiffener

4.2.3 PPLA with flush inserts

PPLA is used in satellite launch vehicle to mount mini-satellites with flush type inserts as explained in Section 1.5. A region with four such inserts as marked in

Figure 4.5 (a) is studied. A skin sheet debond was programmed between two inserts as marked in the photograph in Figure 4.5 (b) and the response is studied.

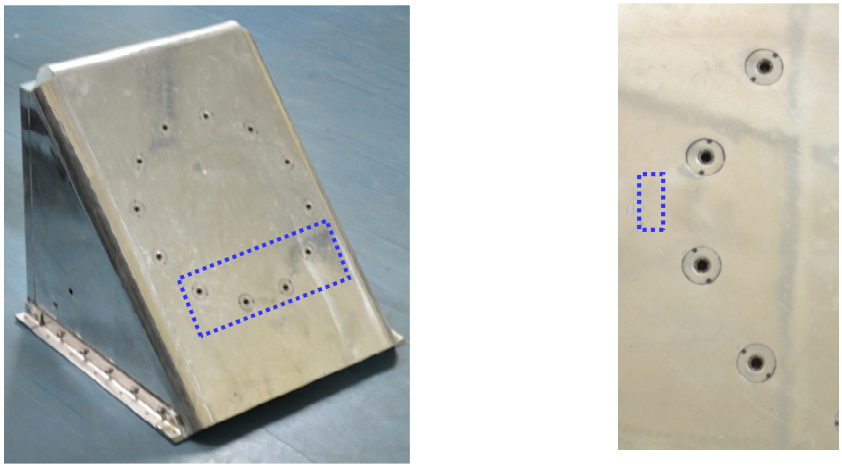

(a) (b)

Figure 4.5(a) Photograph of PPLA (b) zoomed view of the flush type potted insert region with debonded region marked with dotted rectangle

4.2.4 Vibration stressing

Each plate specimen was mounted vertically with one end fixed using a vice and on the other end with a piezo shaker through a vacuum cup as shown in Figure 4.6 (a). Piezo shaker was mounted on potted-insert sandwich specimen and PPLA as shown in Figures 4.6 (b) and 4.6 (c) respectively.

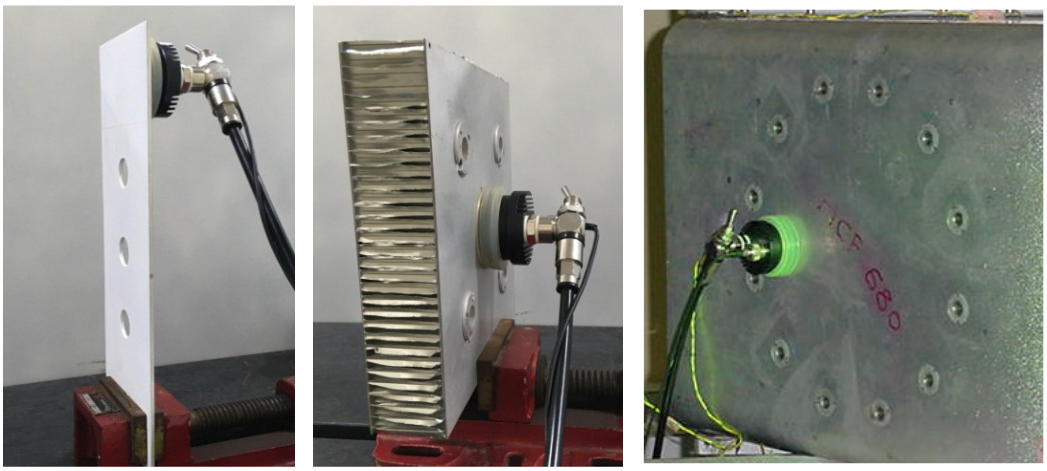

(a) (b) (c)

Figure 4.6 Photographs of (a) plate specimen (b) potted-insert sandwich specimen and (c) PPLA, with piezo shaker mounted on each object using vacuum cup

The frequency of vibration was swept from 1 Hz to 25 kHz with 25 Hz increment during the test. Time average digital holograms were reconstructed in real time and reconstructed images for the entire frequency range during the frequency sweep were stored. Similarly, the reconstructed images were stored for potted insert specimens and PPLA for a frequency sweep from 1 Hz to 25 kHz.

4.3. Results and Discussion

When a structure is vibrated with a forced sinusoidal excitation, the equation of motion for a single degree of freedom is given by Equation (3.1) as $m\ddot{u}+c\dot{u}+ku=F(t)$. Then the operating deflection shape given by the solution u of the above equation depends on the excitation magnitude, excitation frequency and the excitation location along with the mass, stiffness and damping of the system. Since time average digital holography maps the operating deflection shape, the global response of a plate with multiple holes and stiffeners were studied initially to simulate the local effects of such discontinuities on the ODS and compared with that from numerical results. Later the results were correlated with that of a sandwich panel with potted metallic inserts and verified the same on a sandwich structure.

4.3.1 Plate specimens

Typical time average holographic fringe patterns obtained during a frequency sweep of three plate specimens P_1, P_2 and P_3 at low frequencies are shown in Figure 4.7. Fringe patterns indicate that holes and stiffeners have less sensitivity on the global response at low frequencies and the fringes indicate only global behaviour. Moreover, the influences of such discontinuities on local response are hardly visible. The fringe patterns are not locally changed due to the introduction of holes and stiffeners at low frequencies. Hence the presence of such discontinuities could not be identified. However at 24 kHz, the holographic fringe patterns locally differ for P_1, P_2 and P_3 as shown in Figures 4.8 (a), 4.8 (b)and 4.8 (c) respectively. Here the locally stiffened regions of P_3 act as an infinitely rigid point with zero vibration as indicated by regions without any fringes in Figure 4.8 (c). Figures 4.9 (a) and 4.9 (b) show the ODS of specimen P_4 with partially bonded top stiffener and specimen

P_5 with partially bonded bottom stiffener respectively. The region of the stiffener which was not bonded is found locally vibrating as shown by the local fringe pattern. Further, the top two inserts region of the specimen P_4 alone was illuminated and ODS was recorded without a divergent lens for magnifying this region as shown in Figure 4.9 (c).

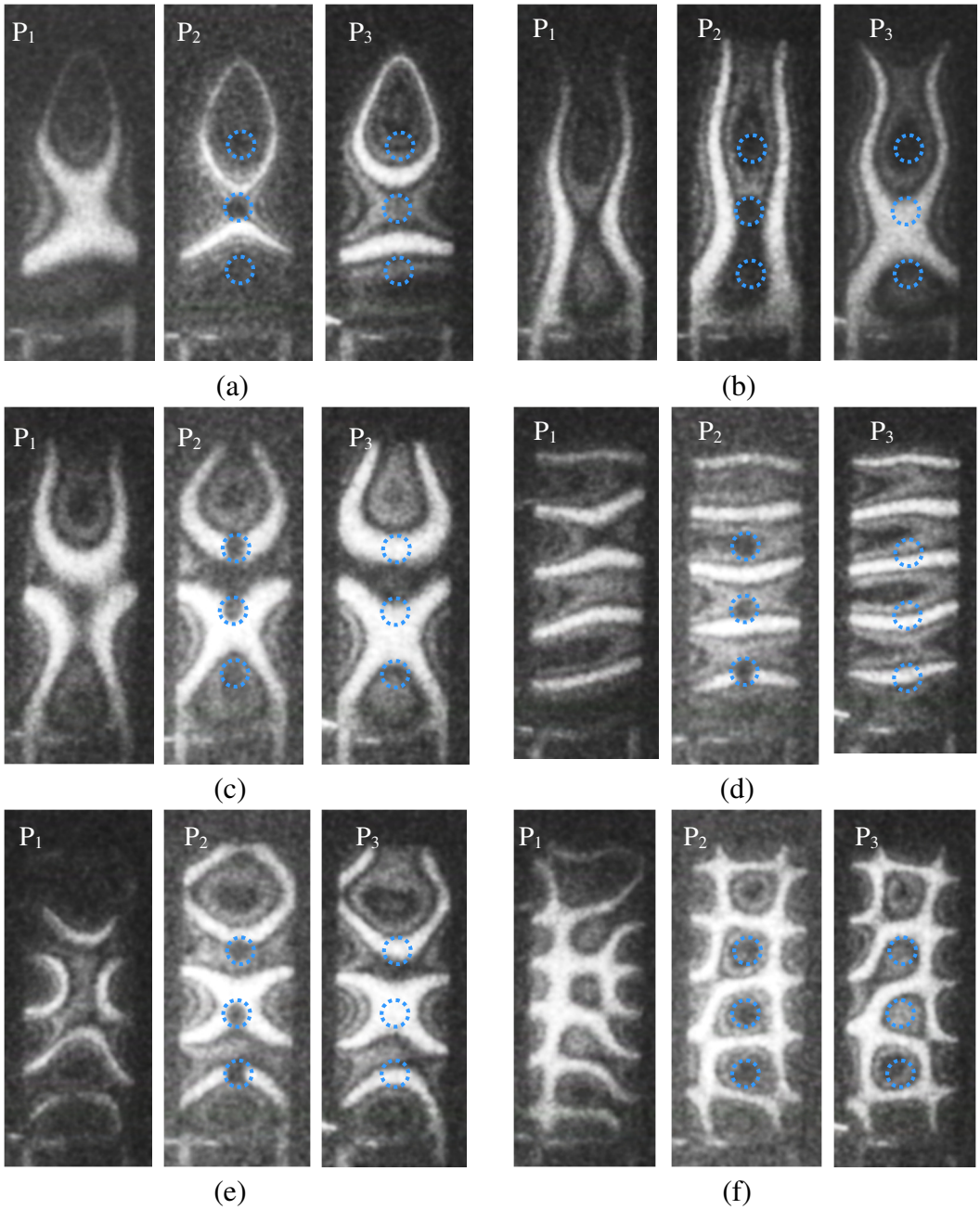

Figure 4.7 Time average holographic fringe patterns forP_1, $P_2$and P_3at six typical frequencies of around (a) 1200 Hz (b) 1700 Hz, (c) 2200 Hz, (d) 2700 Hz, (e) 4100 Hz, (f) 6200 Hz

From these ODS, the extent of debond area can be clearly identified at higher frequencies. It is found from Figure 4.9 (c) that the debonded region vibrates with an amplitude of 0.1µm as the fringe order is 1, considering normal illumination and for laser wavelength of 532 nm.

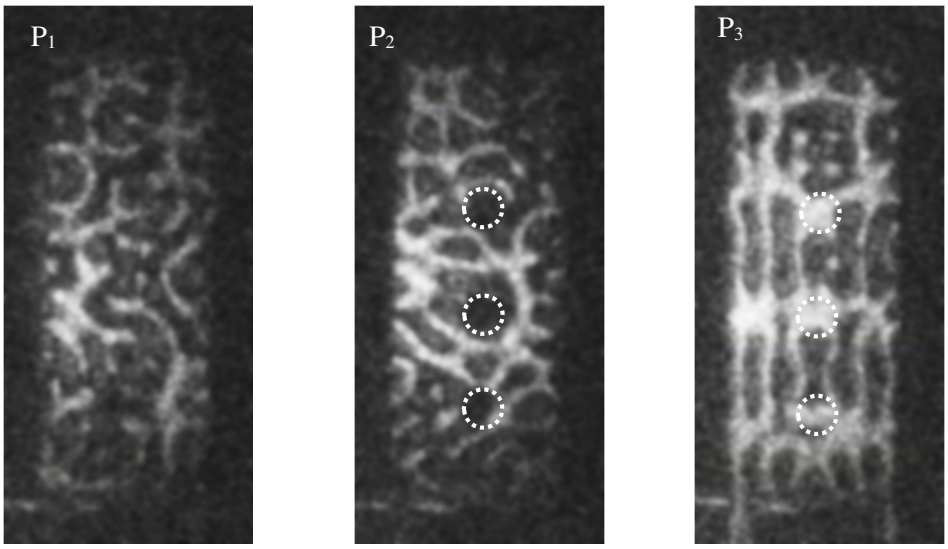

(a) (b) (c)

Figure 4.8 Time average holographic fringe patterns at 24 kHz for (a) plate (b) plate with holes (c) plate with stiffeners

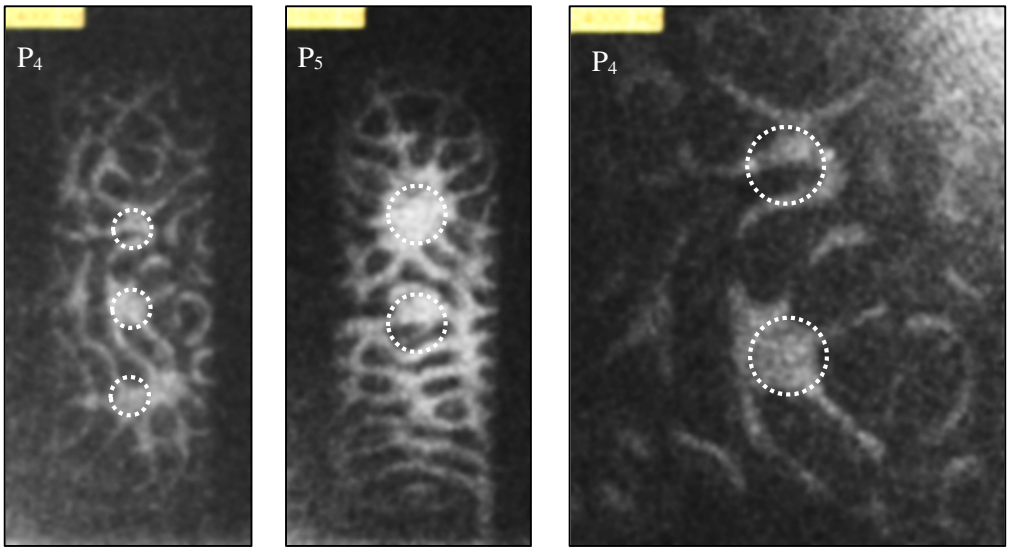

(a) (b) (c)

Figure 4.9 Time average holographic fringe patterns for partially bonded stiffeners (a) specimen P_4 (b) specimen P_5 and (c) Top two inserts region of specimen P_4

4.3.2 Numerical simulation using FEM

Frequency response analysis of plate under forced vibration was carried out and the contours of the out of plane displacement corresponding to the maximum amplitude of vibration were plotted along with that of a plate with multiple holes and multiple stiffeners as shown in Figure 4. 10.

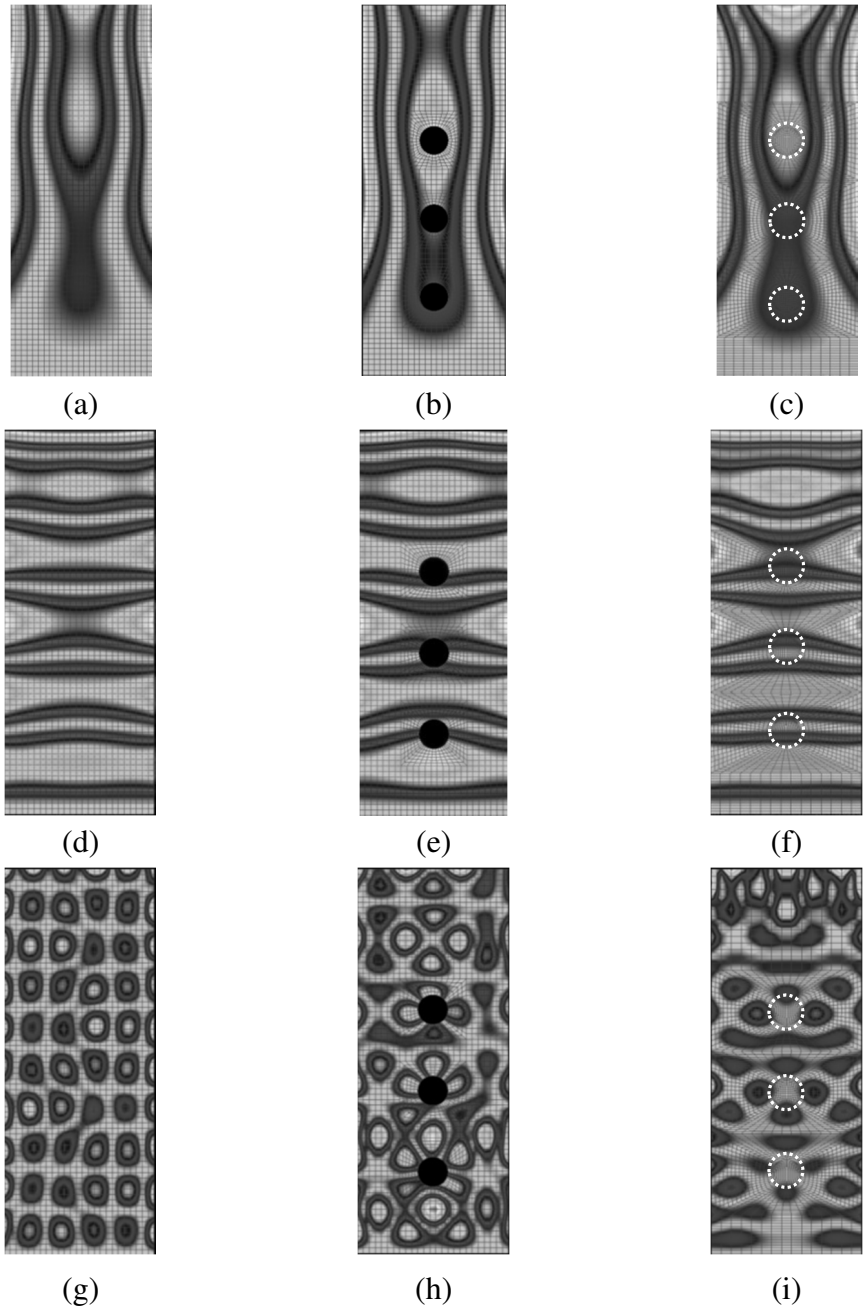

Figure 4.10 Simulated time average fringes at frequencies 1760 Hz, 3200 Hz and 24775 Hz of plate (a), (d) & (g); of plate with three holes (b), (e) & (h); and of plate with three stiffeners (c), (f) & (i)

The plate was modeled with shell elements using (FEAST, 2018). The bottom end of the plate was fixed and sinusoidal force was applied on the top and responses were calculated for a frequency range from 1 Hz to 25 kHz. The first hundred modes $\{\varphi\}_r$, r=1 to 100 were used for the calculation of the response. The frequency response $H(\omega)$ of a multiple degrees of freedom system is given by Equation (4.1) (Mukhopadhyay, 2008)

$$H(\omega) = \frac{\varphi_i \varphi_j / m}{\sqrt{(\omega_n^2 - \omega^2)^2 + (2\xi_d \omega_n \omega)^2}} \tag{4.1}$$

where ω is the excitation frequency, ξ_d is the damping coefficient, ω_n is the natural frequency given as $\omega_n^2 = \frac{k}{m}$, k is the stiffness and m is the mass of the system. From the generalized residual model, the frequency response function is given by Equation (4.2) for lower modes and by Equation (4.3) for higher modes.

$$H(\omega) \cong \frac{\varphi_i \varphi_j}{\omega^2 m} \tag{4.2}$$

$$H(\omega) \cong \frac{\varphi_i \varphi_j}{k} \tag{4.3}$$

The effects of the lower modes tend to have mass-like behavior and the effects of the higher modes tend to have stiffness-like behavior. Hence at low frequencies, the geometric discontinuities are less sensitive to ODS as shown in Figures 4.10 (a) to 4.10 (f). However the local change in the stiffness is very effectively reflected at higher frequencies due to the contributions from the higher modes as evident from the zero response of the locally stiffened regions shown as hard points in both the time average holographic image in Figure 4.8(c) and numerical result shown in Figure 4.10 (i).

4.3.3 Collar insert specimen

Figures 4.11 (a), 4.11 (c) and 4.11 (e) show the time average fringe pattern of potted-insert honeycomb panel without debond at three typical frequencies 4.7 kHz, 5.6 kHz and 22 kHz obtained during frequency sweep. Similarly Figures 4.11 (b),

4.11 (d) and 4.11 (f) show time average fringes of specimen 2 with programmed debond respectively at the above frequencies. It is observed that at low frequencies the influence of holes on the ODS is less and is comparable with the dynamic behaviour observed on plates with multiple holes (Figure 4.7). At higher frequencies of about 22 kHz, the vibration modes become very complex. However, the perfectly bonded inserts act as an infinitely rigid body and indicated clearly as regions without any fringes as shown in Figure 4.11 (e) whereas the debonded face sheets continue to resonate at its higher modes, as visible in the Figure 4.11 (f). This behaviour is in line with that of plate with multiple hole and stiffeners (Figure 4.9).

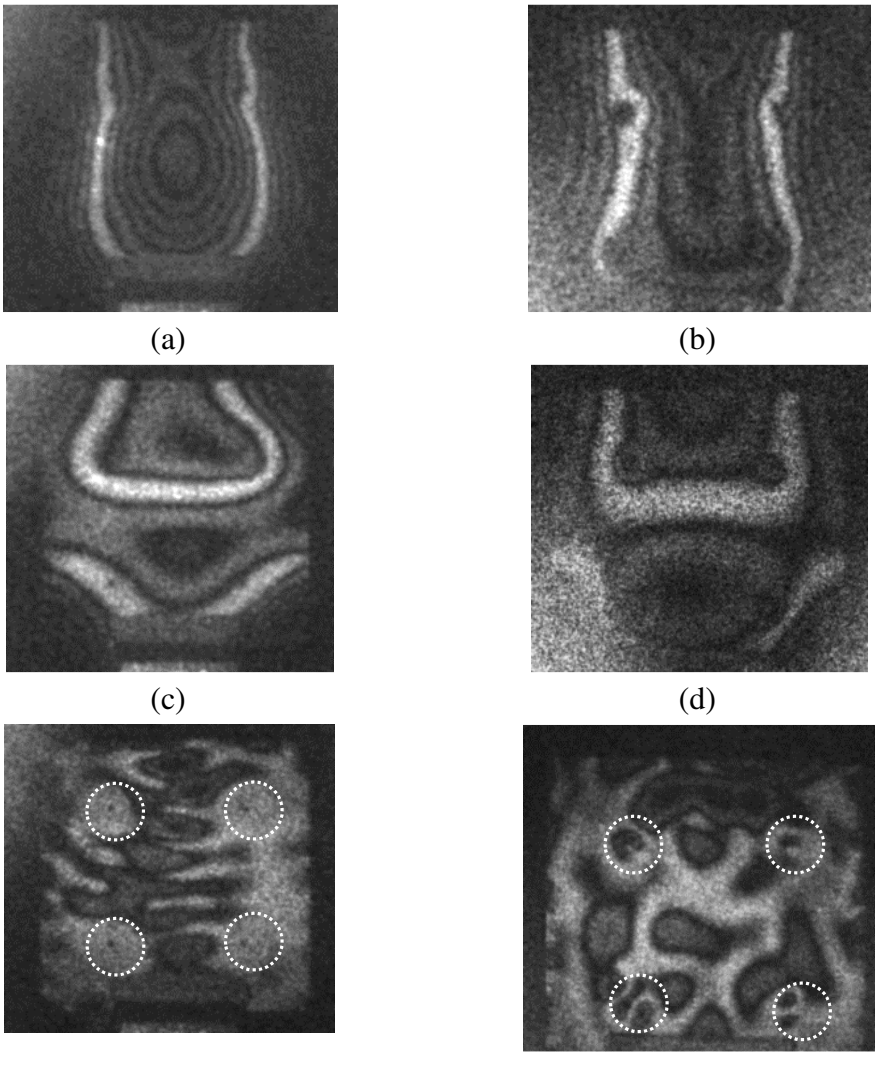

Figure 4.11 Time average fringe patterns at frequencies 4.7 kHz, 5.6 kHz and 22 kHz respectively (a), (c) & (e) of specimen 1 and (b), (d) & (f) of specimen 2

The rigid bond between the face sheet and bottom of the collar insert is not allowing the face sheet at the collar insert of the specimen 1 to vibrate or resonate. This confirms a perfect bond between the bottom of the collar insert and skin sheet of specimen 1 as evident in the case of a plate with multiple stiffeners. This is in good agreement with the assumption made by (Thomsen, 1998) during the analysis considering insert points as an infinitely rigid body to which face sheets and potting material are rigidly connected. From this study, it is clear that inserts with perfect bonding will act as a rigid body with zero vibration amplitude at higher frequencies. Moreover, at higher frequencies, the fringe patterns are found confined to only the debond area in specimen 2 and thus the extent of debond can also be assessed.

4.3.4 PPLA with flush inserts

The behaviour of face sheet with programmed debond between two flush type inserts on a PPLA was mapped at a frequency of 22 kHz as in Figure 4.12 (a). The complex fringe patterns at 22 kHz evidently show the locally stiffened regions as zero response zones. This confirms the rigid bonding of flush type inserts. However, at 9 kHz, the debonded region between the inserts resonate with clear demarcation from the global response as shown in Figure 4.12 (c) confirming the independent nature of debonded skin sheet in the vicinity of geometrical or material discontinuities.

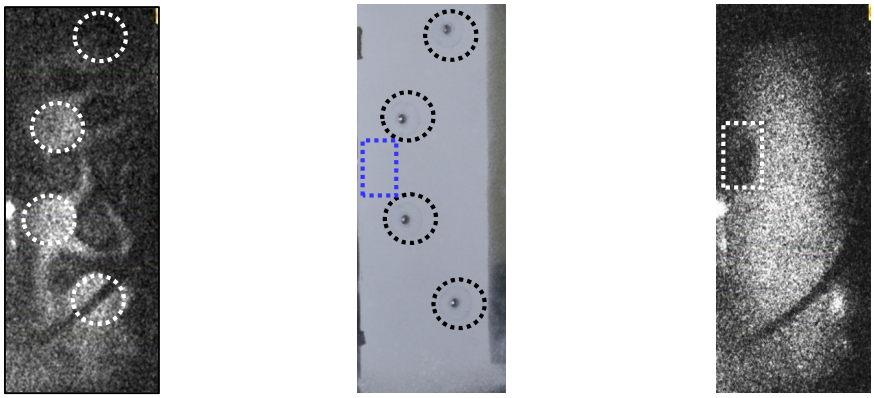

(a) (b) (c)

Figure 4.12(a) Time average fringe pattern at 22 kHz (b) photograph of insert potted region of PPLA (c) time average fringe pattern at 9kHz

Thus at high frequencies, the extent of debond can be verified. However to ascertain face sheet debond, initial modes at low frequencies are to be mapped.

4.4. Conclusion

Dynamic response of a plate specimen with multiple holes and stiffeners under sinusoidal excitation was studied using time average digital holography to understand the influence of such discontinuities on the operational deflection shape at various frequencies simulating potted insert sandwich structure. The experimental results are comparable with the numerical results obtained through FEM. Moreover, the ODS of the plate with partially bonded local stiffeners established the possibility of assessing the extent of debond at high frequencies. Analysis of the time average holograms of honeycomb core sandwich panel with fully potted metallic inserts indicates that the local effects in the vicinity of these hard points are in good agreement with the above study. This study confirmed the feasibility of the time average method of interferometry for inspection of sandwich panels with fully potted metallic inserts. At high frequency of excitation, it was observed that the skin sheet above the metallic inserts acts as infinitely rigid, with zero vibration amplitude. However, the global responses are found very complex at higher frequencies. Nevertheless, the fringe patterns are confined to only the debonded region at higher frequencies. Thus the extent of debond can be evaluated from ODS at high frequencies. It was observed that debonded face sheet resonates at a lower frequency with clear demarcation from the global response irrespective of the geometric discontinuities and local stiffness change due to inserts. These results can be directly used for the industrial application of holography and shearography for the inspection of potted-insert sandwich panels.

CHAPTER 5

COMPUTED TIME AVERAGE FRINGES UNDER RANDOM EXCITATIONS

5.1 Introduction

In time average method of holography, holograms are recorded with an exposure time more than the period of vibration of the structure. Upon reconstruction, the intensity of object field is modulated with square of the zero order Bessel function of first kind given by Equation (1.17) whose argument is the amplitude of vibration at the respective frequency of forcing function or the frequency of single excitation source. However when a structure is vibrated in multiple modes under multiple sources of excitation, depending upon the rational and irrational nature of the modes, the characteristic function is given as an infinite series of sum of product of Bessel function or product of the Bessel function and also in terms of density function as described in Section 1.6. However, for single frequency excitation, time average holographic fringe patterns can be simulated directly using the vibration amplitude at that frequency by various numerical methods. The frequency response analysis using any finite element software can provide the displacement response, which is the input to the Equation (1.17) to plot the fringe patterns. This method is illustrated in Section 3.4 to simulate the fringe pattern for the defective sandwich panel under sinusoidal excitation.

However, the sinusoidal frequency sweep can be replaced with square wave or random excitations for better inspection of debond in honeycomb core metallic sandwich panels as explained in Chapter 3. In an industrial scenario, validation of the time average technique is required for each type and size of defects in each type of component. This necessitates simulation of time average fringe patterns under square (non-sinusoidal) or random excitation with the idea to

minimize the experiments and also for better evaluation of the test results. This data can be further used for automation of defect detection through neural network approach (Kreis et al., 1995). In this study, a method is proposed to compute time average fringe patterns under random excitation. This approach can be followed also for any periodic non-sinusoidal excitation like square wave excitation.

5.2 Proposed Method

Time average holography is the record of time average of the vibrations during the recording time. The position of the object where it spends more time in one vibration cycle is where its velocity is zero. These positions are the turning points or the maximum amplitude positions which contribute more to the hologram exposure than the positions of the object which spend less time (Molin, 1999). And during reconstruction, the interference fringe represents the phase map which describes the vibration amplitude distribution. Hence time average is the probability density function of the vibration amplitude during the recording time (Molin, 1998).

The vibration amplitude of an object under non-sinusoidal or random excitation can be obtained numerically through transient response analysis using finite element method. The probability density function for the vibration amplitude can be determined from the displacement response with respect to time data. Figure 5.1 shows the flow chart of the proposed method. The major input to transient response analysis is the forcing function. Periodic non-sinusoidal forcing function can be easily generated either through the sum of the Fourier components of the respective signal or by using built-in functions in MATLAB. Figures 5.2 (a) and 5.2 (b) show a square signal at 800 Hz generated through built-in function of MATLAB and through the summation of first 15 terms of its Fourier components respectively. However random signals are generated from the displacement power spectral density curve defined over the required frequency range. Figure 5.3 (a) shows the power spectral density (PSD) curve of a random signal which has the same intensity level at frequency range 5 kHz to 6 kHz and zero intensity at all other frequencies.

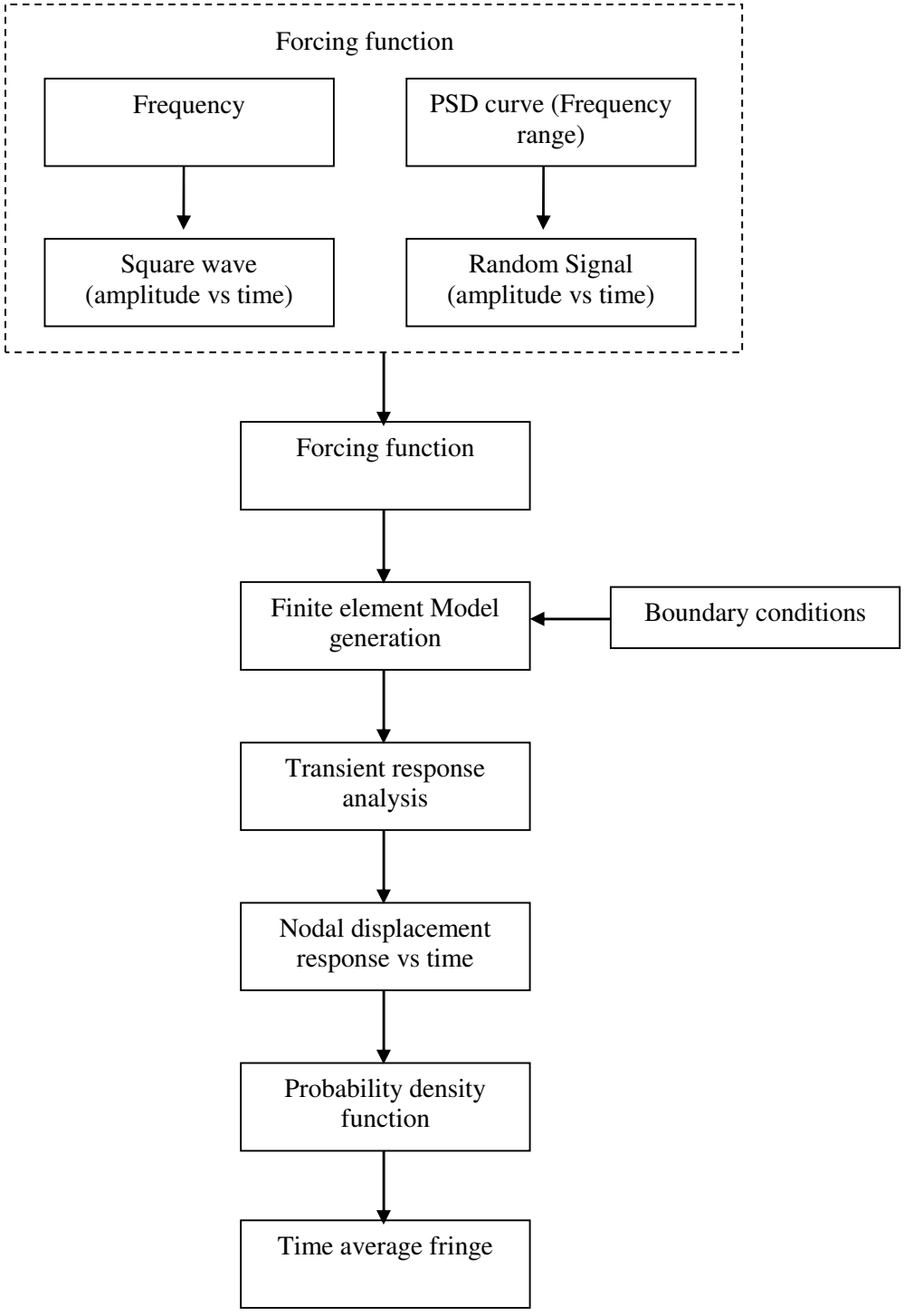

Figure 5.1 Flowchart to simulate time average fringes for random excitation

The white noise signal is a random signal which has the same PSD intensity at all frequencies. A set of random number generated between 0 and 1 is multiplied by 2π to generate random phases ϕ_{rnd}. Then a set of complex noise is generated using exponential function $\exp(i\phi_{rnd})$. The random time signal is generated by taking the

real part of the inverse Fourier transform of the product of the respective PSD and the white noise signal. Figure 5.3(a) shows the random time signal thus generated for a frequency range 5 kHz and 6 kHz. Figure 5.3 (c) shows the frequency content of this random time signal obtained by taking its Fourier transform. This time signal is the input to the transient response analysis as the forcing function. MATLAB code is written to generate the random time signal and also to generate the square wave time signal. The code is given in Appendix A.4.

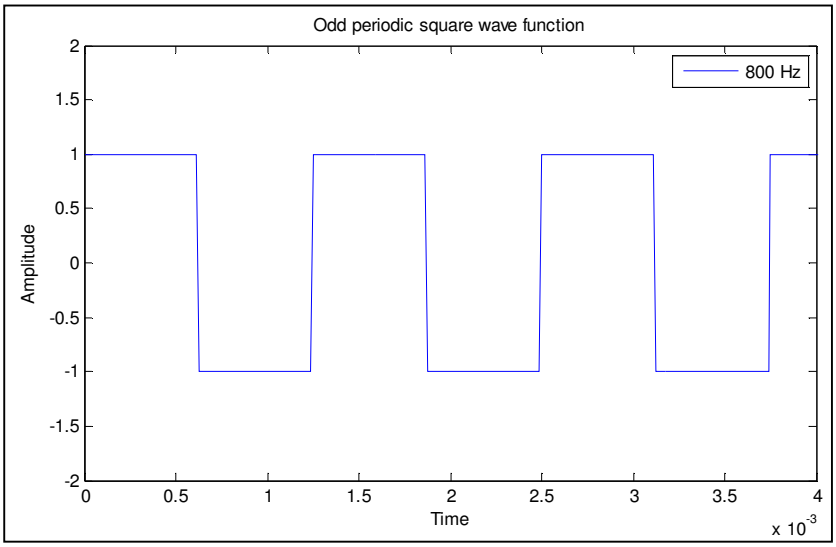

(a)

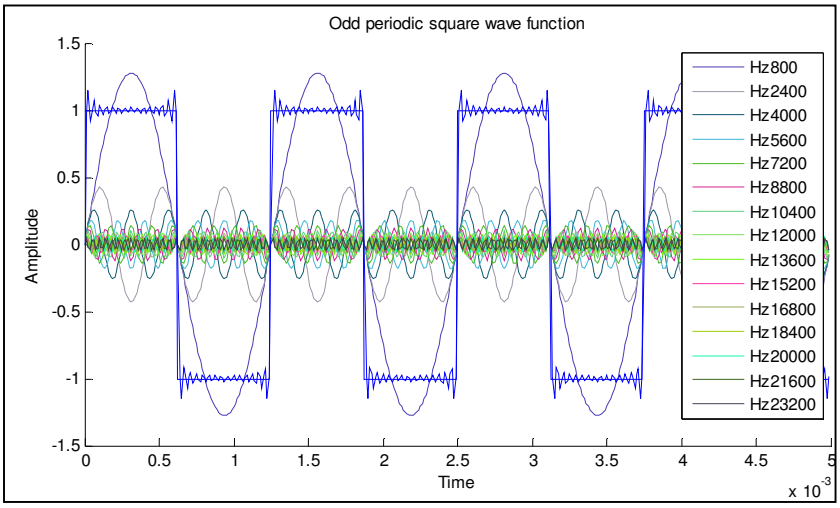

(b)

Figure 5.2 Square wave signal at 800 Hz generated through (a) built in MATLAB functions (b) with summation of first 15 terms of Fourier components

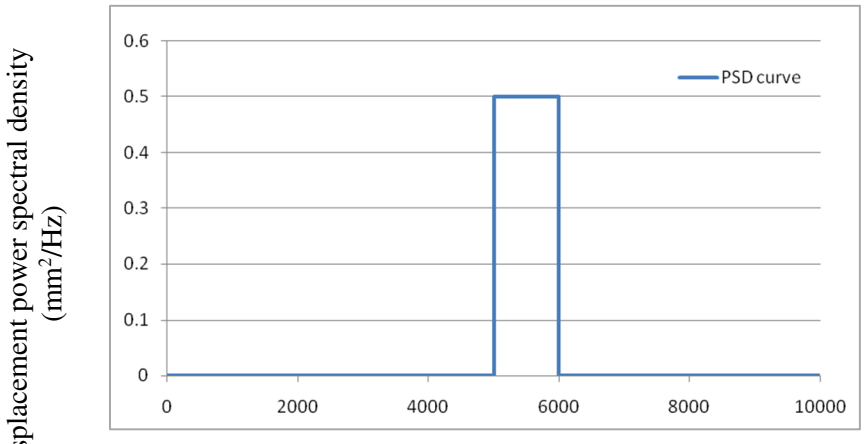

(a)

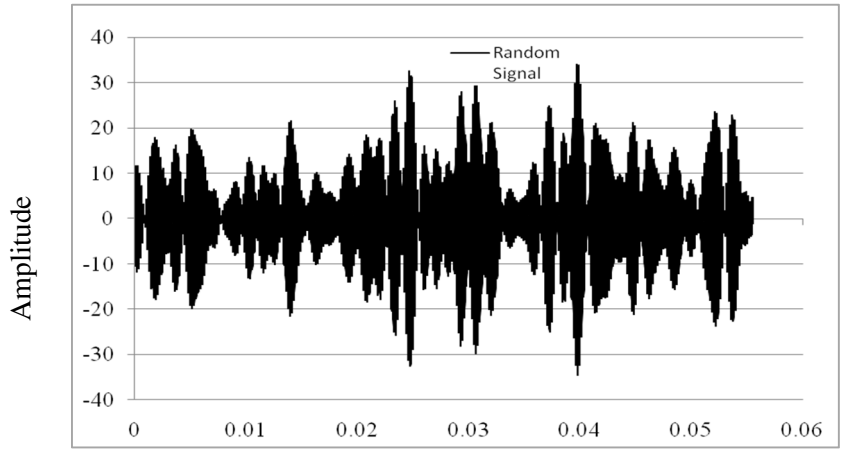

(b)

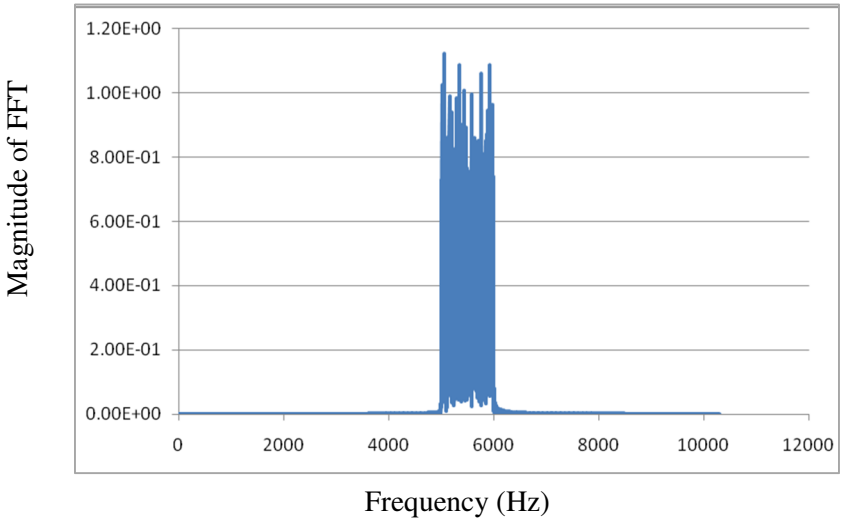

(c)

Figure 5.3 (a) PSD curve for a frequency range 5 kHz to 6 kHz (b) random time signal (c) Fourier transform of the random time signal

5.3 Experimental Details

A rectangular Aluminium plate of size 300 mm × 100 mm with thickness 3 mm was used for the present study. A defect was programmed in the plate as a region with a thickness of 0.5 mm. The off-axis hologram recording setup as explained in Section 3.2 was used for this experiment. The bottom edge of the plate was clamped to vice and the vibration excitation was applied at the top edge. Time average holograms were recorded during a frequency sweep and also with a square wave excitation. The typical time average interferograms of the plate at 600 Hz sinusoidal excitation and 600 Hz square wave excitation are shown in Figures 5.4 (a) and 5.4 (b) respectively. The second bending mode is visible for sinusoidal excitation. However, with square wave excitation at 600 Hz, the defective region locally resonates at one of the Fourier component of the square wave excitation. The defective region is clearly visible with one fringe at the defective region as marked with dotted rectangle in Figure 5.4 (b).

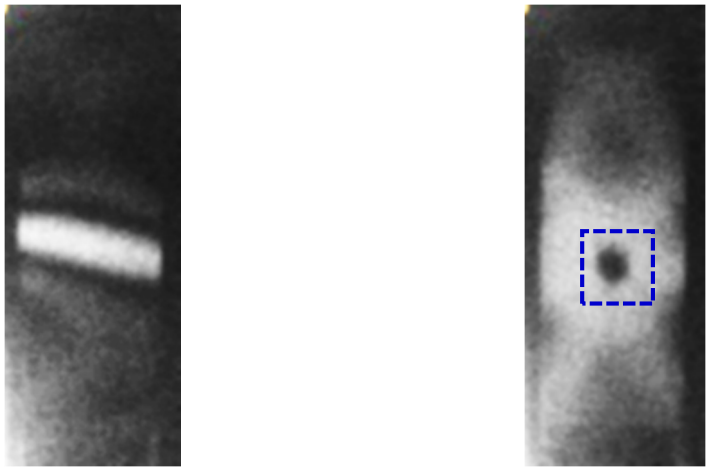

(a) (b)

Figure 5.4 Time average interferogram of plate (a) with sinusoidal excitation at frequency 600 Hz (b) with square wave excitation at 600 Hz.

5.4 Computed Time Average Fringes

Transient response analysis was carried out using (FEAST, 2018). Four-node shell elements are used to model the rectangular plate with dimensions same as that of

specimen used for experiments. Figure 5.5 (a) shows the finite element model of the rectangular plate and Figure 5.5 (b) shows the side view with the boundary condition and force applied. Random excitation defined by the random signal as shown in Figure 5.3 (b) was applied as tip load.

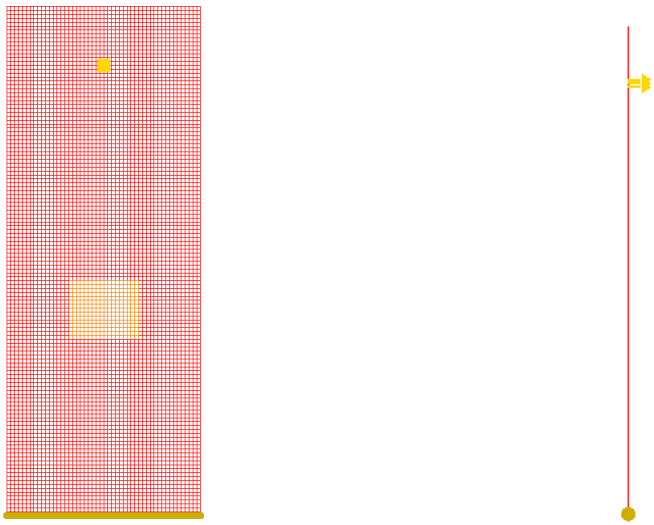

(a) (b)

Figure 5.5(a) Finite element representation of flat plate (b) side view showing the excitation and boundary condition.

Displacement responses of all nodes at every time step were extracted as shown in Figure 5.6 for a typical node. The probability density function is calculated from the displacement response for each node using MATLAB code given in Appendix V. Probability density function for response at a typical node is shown in Figure 5.7.

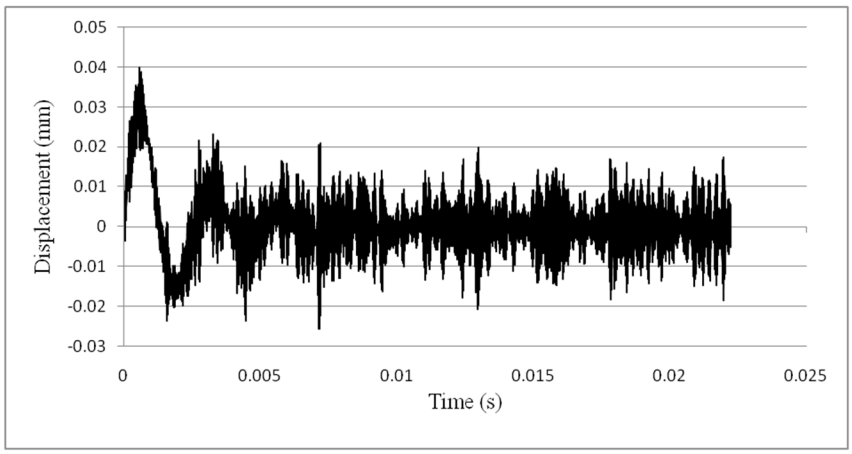

Figure 5.6 Displacement response at a typical node

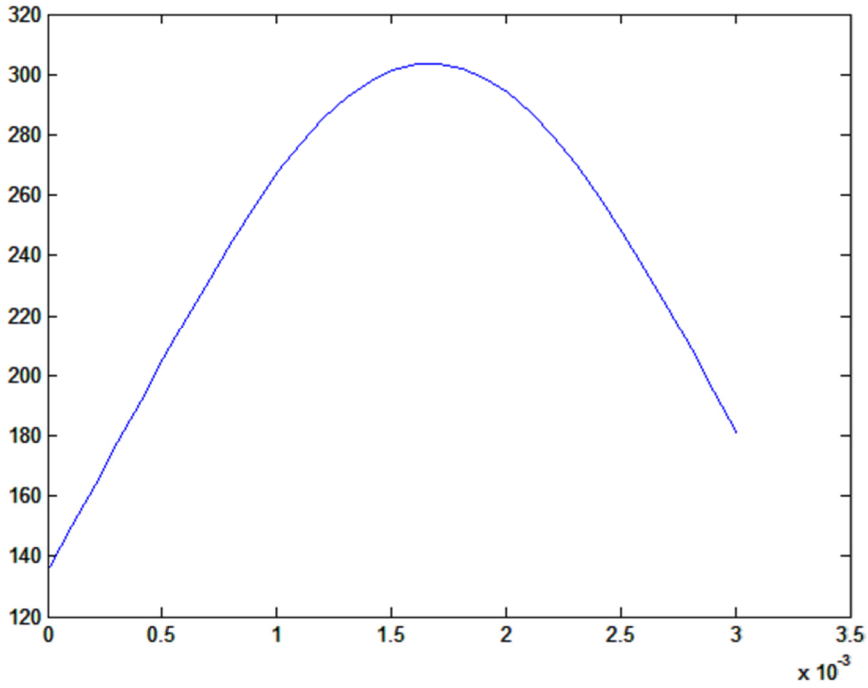

Figure 5.7 PDF of the displacement response at a typical node

The computed time average hologram is shown in Figure 5.8 as generated by the cloud of PDF at every node. MATLAB code used to generate the hologram is given in Appendix V.

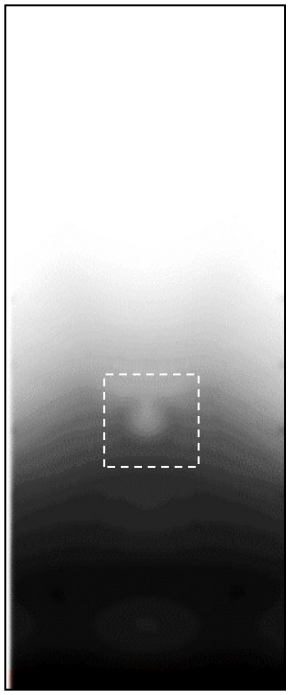

Figure 5.8 Computed time average hologram for random excitation

5.5 Conclusion

Computed time average holographic fringe pattern for multi-frequency excitations like a square wave or random excitation through transient response analysis of an object is proposed and demonstrated in this study. Transient response analysis was carried out for a random excitation numerically using the finite element method and the vibration responses of each node were obtained for a given exposure period of hologram. The probability density functions of the vibration amplitudes at each node were calculated and thus the position of the object which spends more time during the exposure time for each node was obtained. This simulation helps to define the frequency range for random excitation or optimum frequency for square wave excitation.

CHAPTER 6

IMAGING OF STRESSES IN TRANSPARENT OBJECTS

6.1 Introduction

Photoelasticity is an optical technique used for measurement of both magnitude and direction of principal stresses in birefringent materials from the isochromatic and isoclinic fringe system using polariscope. This technique is widely used to measure stresses in components through respective models fabricated using birefringent materials. However, all transparent engineering materials are not birefringent. A polariscope based on digital holography and photoelastic polariscope is proposed to image the stress field in transparent objects which are either birefringent or non-birefringent. Phase information can be obtained directly using digital holography for quantification, whereas it is difficult through conventional holographic approaches listed in Section 1.6. A polariscope with single element circular polarizer instead of the conventional four elements polariscope which consists of a polarizer, analyzer and two quarter-wave plates is proposed. The results were compared with those obtained through conventional photoelastic polariscope. The isopachics of non-birefringent materials were captured through double exposure digital holography without any circular polarizers. It is demonstrated that the proposed digital holographic polariscope could detect these fringes.

6.2 Experimental Procedure and Theory

Three experiments were carried out to demonstrate the capability of proposed digital holographic polariscope for recording isochromatic and isopachic fringes of both transparent non-crystalline birefringent and non-birefringent materials. The experimental geometry of proposed digital holographic polariscope is shown in

Figure 6.1. The vertically polarized beam from an Nd-YAG laser source (M/s Laser Quantum, UK, of model Torus, wavelength 532 nm, power 300 mW) passes through a non-polarizing beam splitter which splits the beam into two parts. One of the beams coming from beam splitter passes through a circular polarizer. This beam is expanded and collimated using spatial filter assembly and a collimator and then passes through the transparent birefringent specimen under test and then reaches CCD camera. This beam is called object beam. The other beam split from beam splitter passes through a circular polarizer and spatial filter assembly and interferes with the object beam at CCD camera plane. This beam acts as a reference beam for recording hologram. The circular polarizer placed in the reference path converts the vertically polarized reference beam into circularly polarized reference beam. Thus both object and reference beams are circularly polarized and they interfere at CCD camera for recording a hologram.

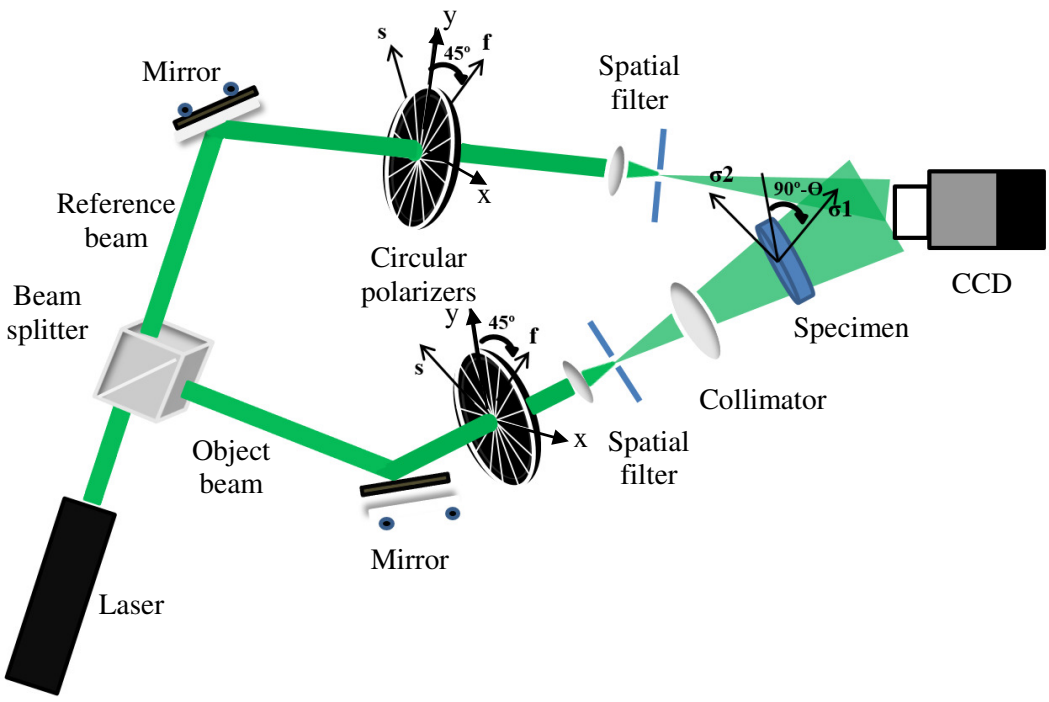

Figure 6.1 Schematic of digital holographic polariscope

The geometry shown in Figure 6.1 is used for the theoretical explanation using the Jones matrix. Consider a loaded photoelastic material, which can be represented in Jones matrix by Equation (6.1), following (Lee and Hu, 1986),

$$P(\delta)=\exp\left[\frac{-i\pi}{\lambda}(n_1+n_2-2n_0)t\right] \times \begin{bmatrix}\cos\theta & -\sin\theta\\ -\sin\theta & \cos\theta\end{bmatrix}\begin{bmatrix}e^{\left(\frac{+i\delta}{2}\right)} & 0\\ 0 & e^{\left(\frac{-i\delta}{2}\right)}\end{bmatrix}\begin{bmatrix}\cos\theta & \sin\theta\\ -\sin\theta & \cos\theta\end{bmatrix} \tag{6.1}$$

where λ is the wavelength of light used, n_1 and n_2 represent refractive indices along the directions of the principal stresses σ_1 and σ_2 respectively and t represents the thickness of the stressed material. The value of n_0 and δ respectively represent the refractive index of surroundings and relative phase retardation of the light beam propagating through the stressed photoelastic material and it is expressed by Equation (6.2),

$$\delta=\frac{2\pi}{\lambda}(n_1-n_2)t \tag{6.2}$$

Using Jones matrix approach the complex amplitude of object beam reaching image sensor plane after passing through circular polarizer and the stressed photoelastic material can be written by Equation (6.3),

$$E_O=\begin{bmatrix}M_{11} & M_{12}\\ M_{21} & M_{22}\end{bmatrix}\begin{bmatrix}1 & i\\ -i & 1\end{bmatrix}\begin{bmatrix}0 & 0\\ 0 & 1\end{bmatrix}\begin{bmatrix}E_{ox}e^{i\xi_x}\\ E_{oy}e^{i\xi_y}\end{bmatrix} \tag{6.3}$$

where the first matrix in Equation (6.3) represents a stressed photoelastic material and using Equation (6.1),

$$\begin{bmatrix}M_{11} & M_{12}\\ M_{21} & M_{22}\end{bmatrix} = e^{\left[\frac{-i\pi}{\lambda}(n_1+n_2-2n_0)t\right]} \times \begin{bmatrix}\cos\theta & -\sin\theta\\ -\sin\theta & \cos\theta\end{bmatrix}\begin{bmatrix}e^{\left(\frac{+i\delta}{2}\right)} & 0\\ 0 & e^{\left(\frac{-i\delta}{2}\right)}\end{bmatrix}\begin{bmatrix}\cos\theta & \sin\theta\\ -\sin\theta & \cos\theta\end{bmatrix} \tag{6.4}$$

$$= \frac{1}{\sqrt{2}}e^{\left[\frac{-i\pi}{\lambda}(n_1+n_2-2n_0)t\right]} \times \begin{bmatrix}\sin^2\theta e^{\left(\frac{-i\delta}{2}\right)}+\cos^2\theta e^{\left(\frac{+i\delta}{2}\right)} & 2i\sin\theta\cos\theta\sin\frac{\delta}{2}\\ 2i\sin\theta\cos\theta\sin\frac{\delta}{2} & \sin^2\theta\, e^{\left(\frac{+i\delta}{2}\right)}+\cos^2\theta e^{\left(\frac{-i\delta}{2}\right)}\end{bmatrix} \tag{6.5}$$

Substituting Equation (6.5) in Equation (6.3) the object beam will reduce to,

$$E_O = \frac{1}{\sqrt{2}} E_{oy} e^{i\xi_y} e^{\left[\frac{-i\pi}{\lambda}(n_1+n_2-2n_0)t\right]} \times \begin{bmatrix} i\left(\sin^2\theta\, e^{\left(\frac{-i\delta}{2}\right)} + \cos^2\theta e^{\left(\frac{+i\delta}{2}\right)} + 2\sin\theta\cos\theta \sin\frac{\delta}{2}\right) \\ \sin^2\theta\, e^{\left(\frac{+i\delta}{2}\right)} + \cos^2\theta e^{\left(\frac{-i\delta}{2}\right)} - 2\sin\theta\cos\theta \sin\frac{\delta}{2} \end{bmatrix} \quad (6.6)$$

Similarly, for reference beam, the Jones matrix will be,

$$E_R = \frac{1}{\sqrt{2}} \begin{bmatrix} 1 & i \\ -i & 1 \end{bmatrix} \begin{bmatrix} 0 & 0 \\ 0 & 1 \end{bmatrix} \begin{bmatrix} E_{rx} e^{i\xi_x} \\ E_{ry} e^{i\xi_y} \end{bmatrix} = \frac{1}{\sqrt{2}} E_{ry} e^{i\xi_y} \begin{bmatrix} i \\ 1 \end{bmatrix} \quad (6.7)$$

Now, the object beam and reference beam interfere at the image sensor plane and the intensity of single exposure hologram is given by (Lee and Hu, 1986),

$$I_H = E_O^+ J_R E_O \quad (6.8)$$

$$I_H = \frac{1}{2} E_{oy}^2 [-iM_{11} \quad M_{12}] \begin{bmatrix} 0 & i \\ 0 & 1 \end{bmatrix} \begin{bmatrix} iM_{11} \\ M_{12} \end{bmatrix} \quad (6.9)$$

where, $M_{11} = \left[\sin^2\theta\, e^{\left(\frac{-i\delta}{2}\right)} + \cos^2\theta e^{\left(\frac{+i\delta}{2}\right)} + 2\sin\theta\cos\theta \sin\frac{\delta}{2}\right]$ (6.10)

and, $M_{12} = \left[\sin^2\theta e^{\left(\frac{+i\delta}{2}\right)} + \cos^2\theta e^{\left(\frac{-i\delta}{2}\right)} - 2\sin\theta\cos\theta \sin\frac{\delta}{2}\right]$ (6.11)

where J_R is the Jones matrix, + is transpose of complex conjugate. Unit magnitude for the reference beam is assumed to arrive at the Equation (6.9). Upon algebraic simplification Equation (6.9) becomes,

$$I_H = E_{oy}^2 \left\{2cos^2\frac{\delta}{2} - 2\sin\theta\cos\theta\sin\delta\right\} \quad (6.12)$$

Substituting the value of $\theta = \pi/4$ for circular retarders, Equation (6.12) becomes

$$I_H = \frac{E_{oy}^2}{2}\left\{2\cos^2\frac{\delta}{2} - 2\sin\frac{\delta}{2}\cos\frac{\delta}{2}\right\} \quad (6.13)$$

Equation (6.13) clearly shows that the intensity of the holographic image is proportional to $\cos^2(\delta/2)$. For plane stress case, thickness of the stressed material is given as $t = t_0 C(1 - \frac{\upsilon}{E})(\sigma_1+\sigma_2)$ where t_0 is the thickness of unstressed material, υ is the Poisson's ratio, $C=A-B$ (Equation (6.16)) and E is the modulus of elasticity of the photoelastic material under test. Substituting these values in Equation (6.2), the value of δ becomes,

$$\delta=\frac{2\pi}{\lambda}(\sigma_1-\sigma_2)t_0 C(1-\frac{\upsilon}{E})(\sigma_1+\sigma_2) \tag{6.14}$$

Substituting Equation (6.14) in Equation (6.13), intensity becomes

$$\begin{aligned} I_H = E_{oy}^2 \Big\{ & \cos^2 \frac{\pi}{\lambda} C(\sigma_1-\sigma_2)t_0 \left(1-\frac{\upsilon}{E}\right)(\sigma_1+\sigma_2) \\ & - \sin \frac{\pi}{\lambda} C(\sigma_1-\sigma_2)t_0 \left(1-\frac{\upsilon}{E}\right)(\sigma_1+\sigma_2) \\ & \times \cos \frac{\pi}{\lambda} C(\sigma_1-\sigma_2)t_0 \left(1-\frac{\upsilon}{E}\right)(\sigma_1+\sigma_2) \Big\} \end{aligned} \tag{6.15}$$

Equation (6.15) represents the fundamental equation of holographic photoelasticity of a stressed material. One can claim to obtain isochromatic $(\sigma_1-\sigma_2)$ fringes alone using single exposure hologram of a stressed specimen using the geometry shown in Figure 6.1. But the phase is modulated with both sum and difference of the principal stresses.

Moreover, double exposure digital holographic interferometry (as explained in Section 1.1.1) of a birefringent material, using the digital holographic polariscope geometry given in Figure 6.1, generate isochromatic fringe system modulated with isopachic fringe system. As in conventional holography, one hologram is recorded before stressing the specimen and another hologram after stressing. The refractive index n_0 of unstressed state of the material is related to that of stresses material by Maxwell-Neumann stress optic law given by,

$$\begin{aligned} n_1 - n_0 &= A\sigma_1 + B\sigma_2 \\ n_2 - n_0 &= B\sigma_1 + A\sigma_2 \end{aligned} \tag{6.16}$$

In Equation (6.16), the refractive index n_1 represents the light polarization in the principal stress direction σ_1 and n_2 represents the light polarization along principal stress direction $\sigma_2$respectively. The terms A and B represent stress-optic coefficient of the material. If ψ_1 and ψ_2 are the phase changes in the directions of σ_1 and σ_2 respectively for loaded model and ψ is the phase change for the unloaded model, then the Jones matrices for loaded photoelastic model $[M]_l$ and unloaded model $[M]_{ul}$ is given as follows (Ajovalasit, 1974)

$$[M]_l = \begin{bmatrix} \cos^2\theta e^{(-i\psi_1)} + sin^2\theta e^{(-i\psi_2)} & \sin\theta\sin\theta\left(e^{(-i\psi_1)} - e^{(-i\psi_2)}\right) \\ \sin\theta\sin\theta\left(e^{(-i\psi_1)} - e^{(-i\psi_2)}\right) & \cos^2\theta\, e^{(-i\psi_2)} + \sin^2\theta\, e^{(-i\psi_1)} \end{bmatrix} \quad (6.17)$$

$$[M]_{ul} = \begin{bmatrix} 1 & 0 \\ 0 & 1 \end{bmatrix} e^{(-i\psi)} \quad (6.18)$$

The object waves for the first and second exposures are given as

$$E_{01} = [M]_l \begin{bmatrix} 1 & i \\ i & 1 \end{bmatrix} \begin{bmatrix} 0 & 0 \\ 0 & 1 \end{bmatrix} \begin{bmatrix} 0 \\ 1 \end{bmatrix} E_{oy} e^{i\psi_o} \quad (6.19)$$

$$E_{02} = [M]_{ul} \begin{bmatrix} 1 & i \\ i & 1 \end{bmatrix} \begin{bmatrix} 0 & 0 \\ 0 & 1 \end{bmatrix} \begin{bmatrix} 0 \\ 1 \end{bmatrix} E_{oy} e^{i\psi_o} \quad (6.20)$$

The reference wave is given as

$$E_R = \begin{bmatrix} 1 & i \\ i & 1 \end{bmatrix} \begin{bmatrix} 0 & 0 \\ 0 & 1 \end{bmatrix} \begin{bmatrix} 0 \\ 1 \end{bmatrix} E_R e^{i\psi_r} \quad (6.21)$$

The absolute retardations δ_1 and δ_2, respectively along the principal stresses directions when the material is loaded due to the changes in refractive index and thickness of the object are given as.

$$\delta_1 = \psi_1 - \psi = \frac{2\pi}{\lambda}[n_1 t - n_0 t_0 - n(t - t_0)] \quad (6.22)$$

$$= \frac{2\pi}{\lambda}\,[(n_1 - n_0) + (n_0 - n)(t - t_0) \quad (6.23)$$

$$= \frac{2\pi}{\lambda}\left[(A\sigma_1 + B\sigma_2) - (n_0 - n)\frac{\gamma}{E}(\sigma_1 + \sigma_2)\right] t_0 \quad (6.24)$$

$$\text{Similarly, } \delta_2 = \frac{2\pi}{\lambda}\left[(B\sigma_1 + A\sigma_2) - (n_0 - n)\frac{\gamma}{E}(\sigma_1 + \sigma_2)\right] t_0 \quad (6.25)$$

The light intensity of the primary image reconstructed from the double-exposure hologram can be expressed by the Equation (6.26) following Ajovalasit (1974)

$$I_H \propto [(E_R^+ E_{O1})^*(E_R^+ E_{O1}) + (E_R^+ E_{O2})^*(E_R^+ E_{O2}) + (E_R^+ E_{O1})(E_R^+ E_{O2})] \qquad (6.26)$$

Substituting the respective values in the above equation, Equation (6.26) becomes

$$I_H \propto 1 + 2\cos\left[\frac{\pi t_0}{\lambda}(A' + B')(\sigma_1 + \sigma_2)\right].\cos\left[\frac{\pi t_0}{\lambda}C(\sigma_1 - \sigma_2)\right] + \cos^2\left[\frac{\pi t_0}{\lambda}C(\sigma_1 - \sigma_2)\right] \qquad (6.27)$$

Here isochromatic fringe system is modulated with isopachic fringe system. It is generally not possible to separate the combined isopachic and isochromatic terms represented in the intensity Equation (6.27). But there are methods to separate it, and is beyond scope of this work. For obtaining isopachic fringes (σ_1+σ_2) alone for birefringent material, the circular polarizers in both object and reference arms are not required. Accordingly, the circular polarizers are removed from both object and reference arms and the modified geometry is shown in Figure 6.2. Now, by using conventional double exposure digital holographic interferometry method one can get isopachic fringes by recording holograms before and after the application of stress to the photoelastic object.

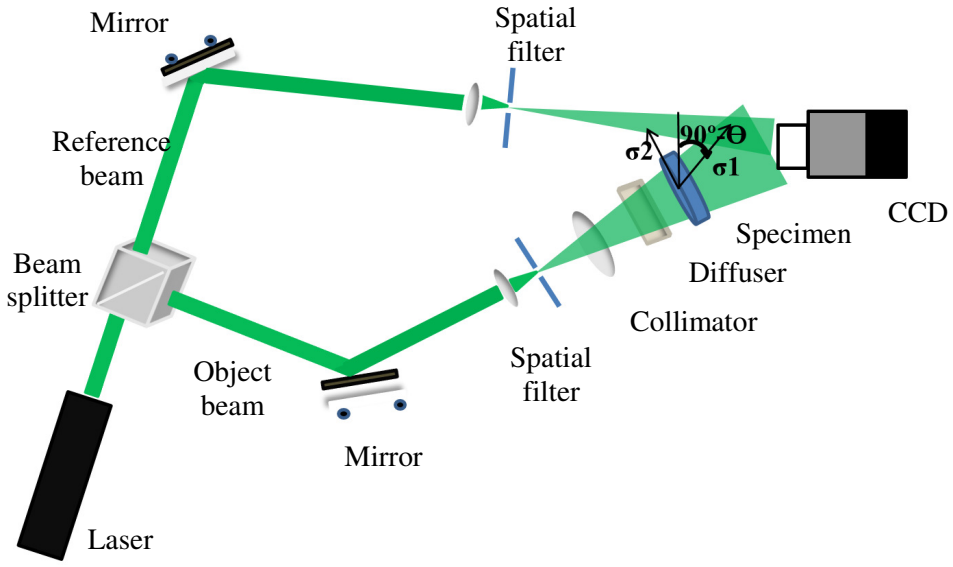

Figure 6.2 Schematic of digital holographic polariscope without circular polarizers

The modified intensity equation (Appendix I) can be represented by Equation (6.28). However, care should be taken to minimize the rigid body motion during loading.

$$I_H = \frac{E_{oy}^2}{2}\left\{cos^2 \frac{\pi t_0}{\lambda} C(\sigma_1 + \sigma_2)\right\} \quad 6.28$$

Further, if the object is a non-birefringent material, then the refractive index will be a constant value, and it will not undergo stress-induced refractive index change and because of that non-birefringent materials are insensitive to polariscope arrangement. As these materials exhibit only the thickness variations given by $t_0 - t = \frac{\upsilon}{E} t_0(\sigma_1+\sigma_2)$, isopachic fringes ($\sigma_1+\sigma_2$) are formed as a result of interference of two images formed after the first and second exposures respectively. Thus for non-birefringent material the intensity I reduces to Equation (6.29) (Appendix II)

$$I_H = 4cos^2\left(\frac{\pi t_0}{\lambda} C(\sigma_1 + \sigma_2)\right) \quad 6.29$$

6.3 Numerical Analysis of Digital Holographic Polariscope

Both numerical simulation and experimental studies were carried out to demonstrate the superiority of this digital holographic polariscope method for both birefringent and non-birefringent materials over conventional polariscope. Same sizes of birefringent and non-birefringent disc and ring specimens under the diametrical compression were considered for simulation and experiments. The details of the preparation of the birefringent and non-birefringent specimen are given in Section 6.4.

6.3.1. Isochromatic Fringes

The specimens are assumed to be loaded in the plane stress state with the principal stresses lie on x and y coordinates. For the stress-induced birefringent disc specimen

under diametrical compression, the principal stress components σ_1 and σ_2 are given by (Theocaris and Gdoutos, 1978),

$$\sigma_1 = \left(\frac{P}{\pi t R}\right) \frac{\left(x^2+y^2-R^2\right)^2}{\left(x^2+y^2-R^2\right)^2-4R^2y^2} \tag{6.30}$$

$$\sigma_2 = \left(\frac{P}{\pi t R}\right) \frac{\left(x^2+y^2-R^2\right)\left(x^2+y^2+3R^2\right)}{\left(x^2+y^2-R^2\right)^2-4R^2y^2} \tag{6.31}$$

In Equations (6.30) and (6.31), P represents the applied load, R is the radius of the disc and t is the thickness of the disc specimen. The wavelength of the monochromatic light was taken as 532 nm. Using the above two equations numerical simulations of single exposure holographic fringes of stressed birefringent disc specimen under compression were carried out using a MATLAB code. For ring specimen, the principal stresses obtained through FEM were used to plot the fringe patterns. Figures 6.3 (a) and 6.3 (b) show the numerically simulated single exposure holographic photoelastic fringes of stressed birefringent disc and ring specimens subjected to diametric compression.

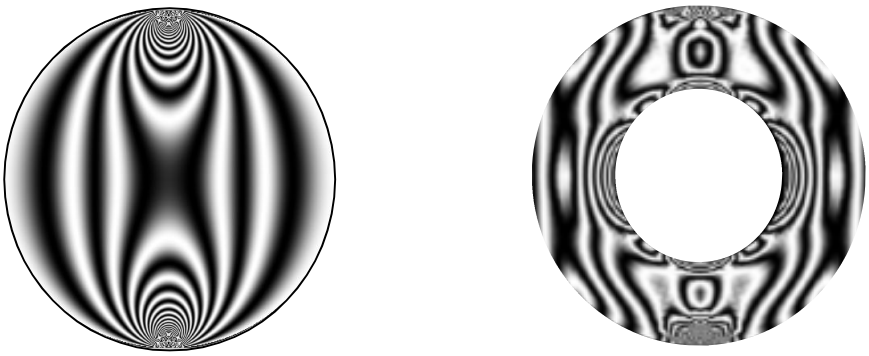

(a) (b)

Figure 6.3 Numerically simulated isochromatic fringes (a) disc under compression (b) ring under compression

6.3.2. Isopachic Fringes

Figure 6.4 (a) shows simulated isopachic fringe patterns for the birefringent disc using double exposure method with recording geometry in Figure 6.2. The

isopachic fringe of ring specimen of non-birefringent specimen with recording geometry in Figure 6.1 is shown in Figure 6.4 (b). Figure 6.4 (c) corresponds to isochromatic fringes modulated with isopachic fringes of disc under compression obtained through double exposure method with recording geometry in Figure 6.1

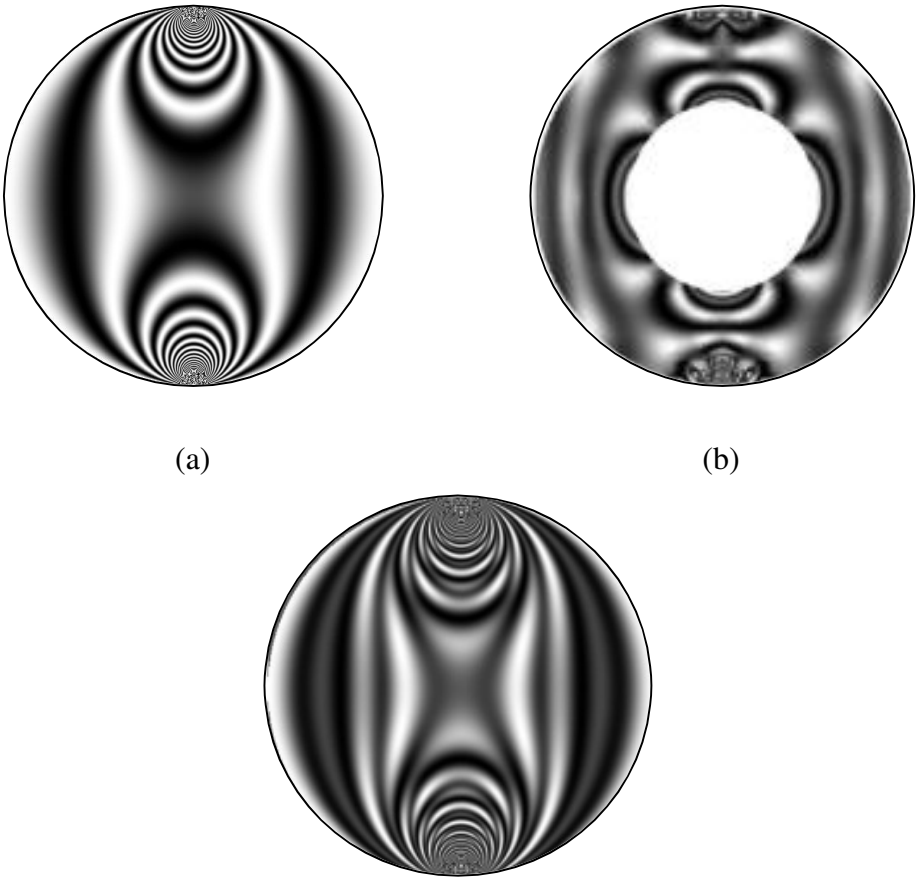

(a) (b)

(c)

Figure 6.4 Numerically simulated holographic isopachic fringes of (a) disc under compression and (b) ring under compression (c) isochromatic fringes modulated with isopachic fringes

6.4 Experimental Results and Discussion

Birefringent and non-birefringent specimens were used for conducting photoelasticity experiments with conventional polariscope and digital holographic polariscope. The birefringent specimen was fabricated through machining and casting processes. The epoxy resin used was Araldite CY230 cured with hardener AradurHY951 in the ratio 10:1. The epoxy casting was made out of thermosetting

resin, which while curing with the hardener undergoes polymerization. To study the nature of isochromatic and isoclinic fringes in the above specimens, single exposure holograms were recorded. These specimens can be either stress frozen or with live loading. In the present study, stress-frozen specimens were used. The stress frozen specimen was fabricated through continuous heating and cooling processes called stress freezing cycle. The loaded epoxy resin specimen was placed in an oven and the temperature was increased in steps upto 70^0C. Then after a short time interval, the specimen was allowed to gradually cool down. Due to this heating and cooling processes, the birefringent specimens will be in the stress frozen state and are considered to study the fringe system. On the other hand, the non-birefringent specimens were fabricated using Plexiglas sheets available in the market. Specimens from Plexiglas sheets were fabricated with cutting and filing tools

6.4.1Conventional photoelastic circular polariscope

Isochromatic, isopachic and isoclinic fringes of birefringent and non-birefringent specimens were recorded using both the conventional and digital holographic polariscope as this is required for comparison. The schematic of experimental setup of a conventional photoelastic polariscope to determine the variation of the stress field in birefringent and non-birefringent material is shown in Figure 6.5. The light beam from the source is polarized using a polarizer and then it passes through a quarter wave plate. The quarter wave plate converts linearly polarized light to circularly polarized and then circularly polarized light passes through the test specimen. The light after passing through test specimen passes through a second quarter wave plate which will convert the light back into plane polarized light. This light then passes through the analyzer and falls on to the digital camera. By rotating the analyzer desired intensity pattern in the CCD camera can be obtained. The theoretical explanation for conventional circular polariscope is shown in Appendix III and following that the intensity of light beam obtained from this conventional circular polariscope as $I = \cos^2(\delta/2)$ given by Equation (C.4) in Appendix III.

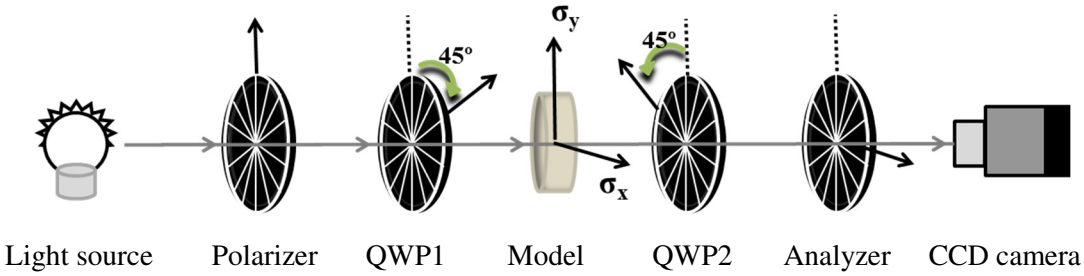

Figure 6.5 Schematic of conventional circular polariscope

6.4.1.1. Isochromatic and isoclinic fringes

The isochromatic fringes are lines of constant relative retardation along which the maximum shear stress or the difference between the principal stresses$(\sigma_1-\sigma_2)$occur. The isochromatic fringe pattern of a stress-induced birefringent specimen (epoxy resin) was recorded using the polariscope geometry shown in Figure 6.5. The isochromatic patterns recorded using Sodium light source are shown in Figures 6.6 (a) and 6.6 (b)

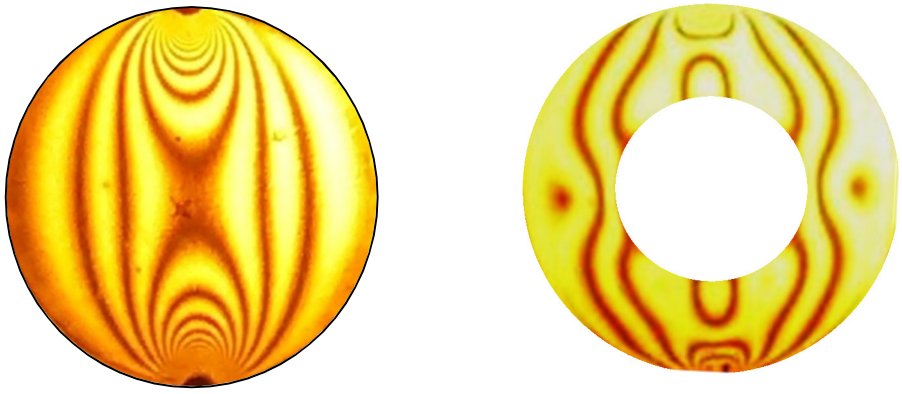

(a) (b)

Figure 6.6 Isochromatic fringes of a stressed birefringent (a) disc (b) ring obtained using conventional polariscope with Sodium light source

The combined isochromatic and isoclinic fringe patterns are formed in stress frozen birefringent disc specimens under linear polariscope with both quarter wave plates removed from the setup shown in Figure 6.5. Figure 6.7shows the isoclinic fringe system obtained when stress-frozen transparent birefringent specimen illuminated with Sodium light source using the conventional linear polariscope

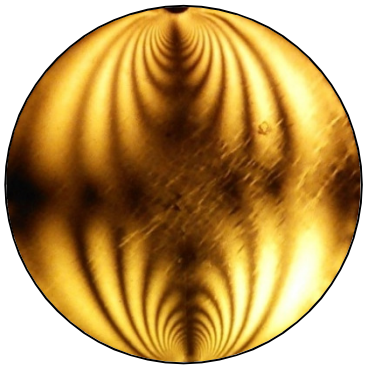

Figure 6.7 Combined isochromatic and isoclinic fringe systems of stressed birefringent disc under compressive load.

6.4.1.2. Isopachic fringes

The isopachic fringes are the locus of points of constant thickness, which indicate the changes in optical path length of an odd multiple of half wavelength. These changes are the result of a displacement, a change in refractive index of refraction or other means of changing optical path length. And also it represents the sum of principal stresses contours.

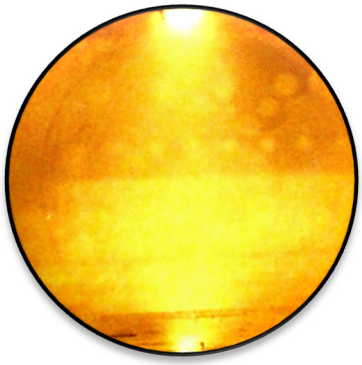

Figure 6.8 Stressed non-birefringent object when viewed using conventional polariscope with Sodium light source

In the case of non-birefringent materials, the isochromatic and isoclinic fringes are not formed as there will not be any change in refractive index unlike in birefringent materials. But, isopachic fringes can be obtained when a non-birefringent material undergoes stress. The conventional polariscope can recognize the isochromatic fringes of a stressed birefringent specimen when viewed through crossed polarizers, but it fails to recognize the isopachic fringes of a stressed non-birefringent specimen

(Plexiglas). Experiments with Sodium light source were conducted with stress-induced non-birefringent specimen as object. Figures 6.8 show the fringe system obtained for a stress-induced non-birefringent specimen using Sodium light source. It is clear from Figure 6.8 that conventional polariscope does not recognize the change in phases of light beam passing through the non-birefringent specimen before and after the application of stress.

6.4.2 Digital holographic polariscope

Experiments using both birefringent and non-birefringent specimens (same as that used for simulations as well as for conventional polariscope) as objects were conducted using digital holographic polariscope.

6.4.2.1. Isochromatic and isoclinic Fringes

The double exposure holographic fringes of non-stressed birefringent disc specimen recorded using the proposed digital holographic polariscope is shown in Figure 6.9(a) and we can clearly see the isochromatic fringes superposed with isopachic fringes. This is consistent with the Equation (6.27) for intensity, as it depends upon both isochromatic and isopachic fringes. The pure isochromatic fringe pattern of stress frozen is generated using digital holographic polariscope with the circular polarizer as shown in Figure 6.9 (b). Similarly combined isochromatic and isoclinic fringe patterns of the same (stress frozen Araldite) specimen is also generated as shown in Figure 6.9(c) using digital holographic polariscope. With the introduction of a diffuser which produces a random point to point polarization, the random irradiance distribution formed by light polarized along the σ_1 direction will be uncorrelated with that formed by light polarized along σ_2 direction. Therefore, the irradiance pattern of the image formed by the double exposure hologram is the sum of the irradiance of the two polarization components. A diffuser can thus eliminate a certain portion of isochromatic fringes but it is not possible to eliminate completely the superposition of isochromatic and isopachic fringes from a stressed birefringent specimen.

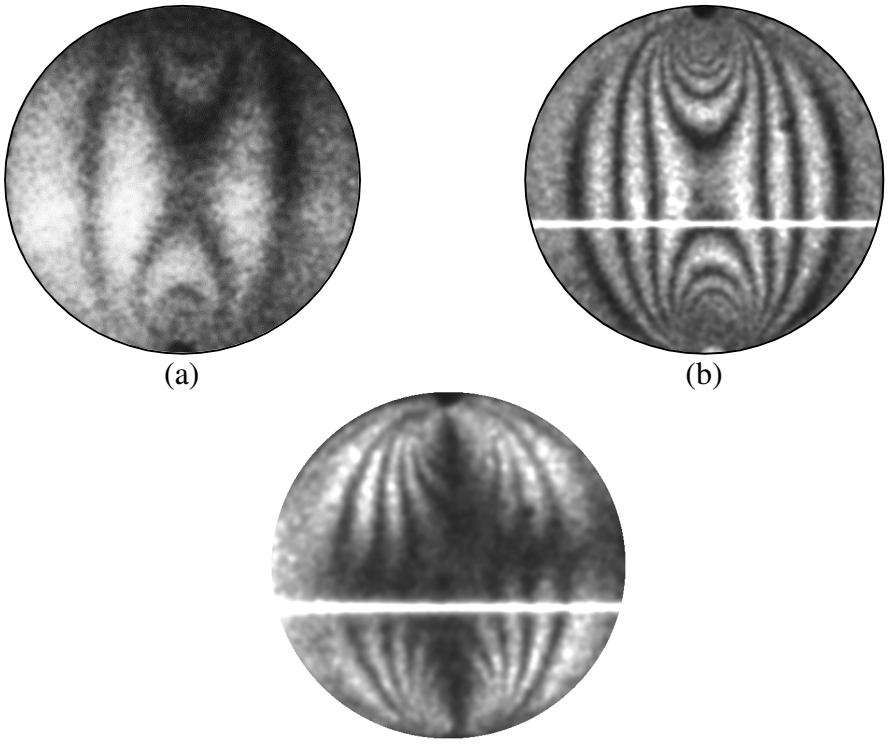

(a) (b)

(c)

Figure 6.9(a) Isochromatic fringes superposed with isopachic fringes (b) isochromatic fringes and (c) isochromatic fringes superposed with isoclinic fringes of birefringent disc specimen

The experiment to record isoclinics is similar to the recording of the isochromatic fringe patterns of stressed specimen, but the polarization angle of the reference beam has to be continuously varied to obtain isoclinic fringes. The variation is controlled by the rotation of linear polarizer replacing circular polarizer in the reference path. The dark field isoclinic fringe pattern is obtained when the linear polarizer is kept at an angle 0^0 and the angle of circular polarizer along the object path is kept at 90^0. Similarly, for obtaining bright field isoclinic fringe pattern, the linear polarizer along reference path should be kept at 90^0 and the circular polarizer along object path should be kept at 90^0respectively. Similarly, Figure 6.10 (a) shows superimposed isochromatic and isopachic fringes and Figure 6.10 (b) shows the isochromatic fringes for ring specimen. During numerical reconstruction, if the reconstructed image is not confined to a quadrant, streaks of the DC term, (shown as horizontal lines in Figure 6.9) may overlap the image. This can be avoided by proper alignment of reference beam and controlling its intensity.

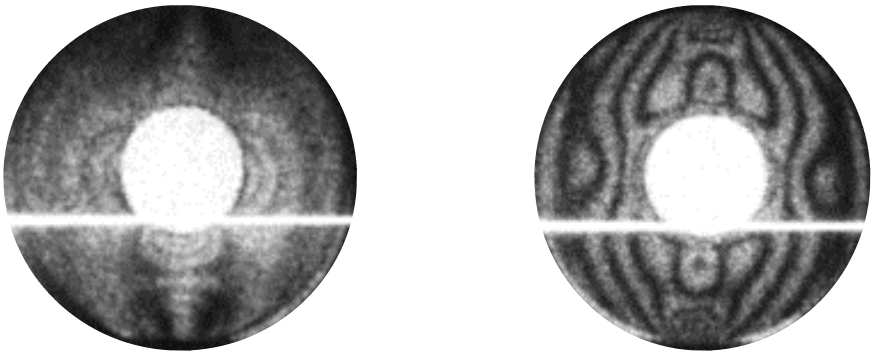

(a) (b)

Figure 6.10(a) Isochromatic fringes superposed with isopachic fringes (b) isochromatic fringes of a birefringent ring specimen

To obtain a representative picture on fringe order errors in isochromatics recorded using the digital holographic polariscope, fringe orders along a line near the center of the disc is plotted and compared with that obtained from simulated isochromatics. Initially wrapped phase maps are generated for both the experimental and simulated fringe patterns using the fringe orientation and direction based quadrature transform algorithm (Larkin et al., 2001; Servin et al., 2003; Quiroga et al., 2007; Kaufmann, 2011). Figure 6.11 (a) and 6.11 (b) show the wrapped phase maps around the central region of the disk superimposed over the respective experimental and simulated fringe patterns.

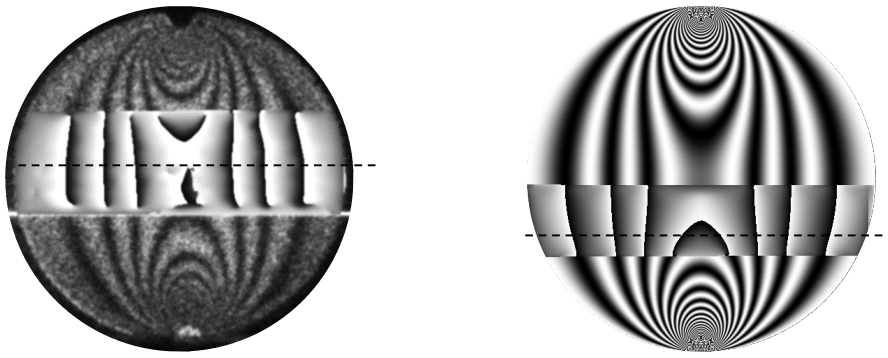

(a) (b)

Figure 6.11 Wrapped phase maps along the middle region of the disc specimen superimposed over (a) isochromatic fringes recorded using digital holographic polariscope and (b) simulated isochromatic fringes pattern

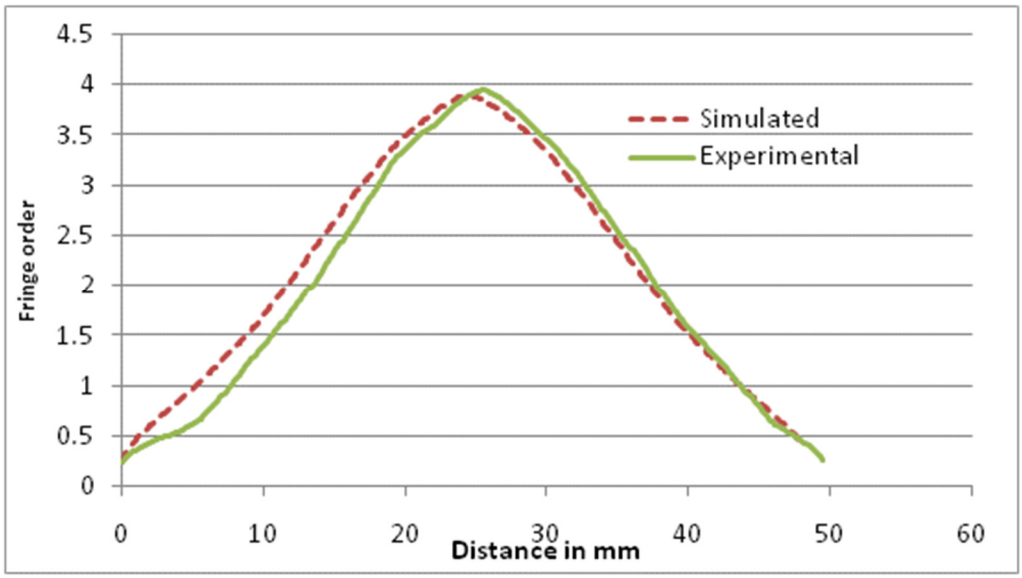

Figure6.12 Fringe order plot along the line across the width of the disc

Then wrapped phase data along a line as shown in Figures 6.11(a) and 6.11(b) near the center of the disc is unwrapped and the fringe order is plotted as shown in Figure 6.12 for experimental and simulated fringe patterns. A slight shift in fringe order is observed, however the fringe orders are found comparable from this plot. So similar to conventional polariscope the error in the fringe order calculation is limited by the contributions from loading setup and from wavelength-specific optical elements.

6.4.2.2. Isopachic fringes

The isopachic fringe separation is a difficult task in holographic fringe analysis because the rigid body motions play a crucial role in the isopachic fringe analysis. Commonly the double pass method with Faraday rotator (Regan and Dudderar, 1971; Chau, 1968; Chatelain, 1973), and the immersion methods (Kihara et al., 1976) are mainly preferred for isopachic fringe separation in transparent materials; these experiments are complex processes because of using Faraday rotor and other optical instruments. Here we could separate isopachic fringes from birefringent and non-birefringent material, without using complex optical elements. The experimental geometry shown in Figure 6.2 after removing circular polarizers from the object and reference beam is used to record double exposure holographic interferometry.

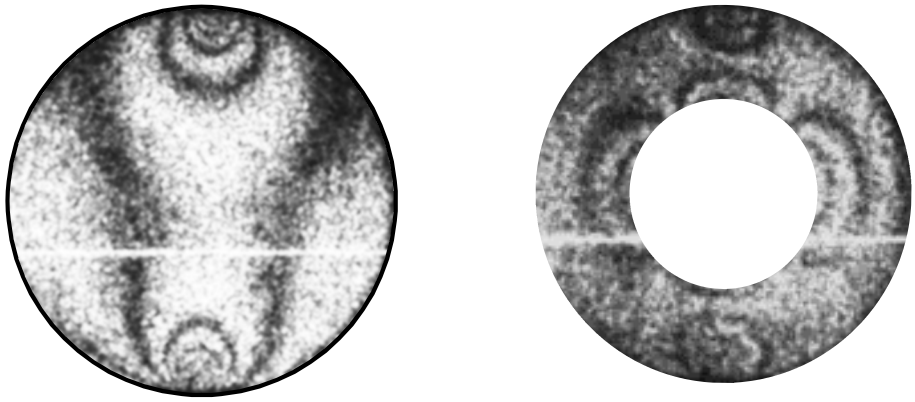

(a) (b)

Figure 6.13 Isopachic fringes obtained using digital holographic polariscope of a stressed non-birefringent (a) disc (b) ring specimens

Isopachic fringe separation is carried out using a double exposure holographic method in birefringent and non-birefringent disc specimens. The first exposure is taken before the load is applied to specimen and the second exposure is after the application of load on to it. Two different holograms were recorded on the image sensor and numerical reconstructions were carried out. We could obtain isopachic fringe patterns of a birefringent specimen (Araldite) and non-birefringent specimen(Plexiglas) clearly and this is consistent with the phase retardation δ derived in Appendix II as it is equal to $\frac{\pi}{\lambda} t_0 \, C \, (\sigma_1 + \sigma_2)$.Figures6.13 (a) and 6.13 (b) show the isopachic fringes for a non-birefringent (Plexiglas) disc and ring specimens respectively obtained using double exposure digital holography method in the digital holographic polariscope set-up shown in Figure 6.2. This result is in contrast to conventional polariscope as it could not record isopachic fringes of a stressed non-birefringent specimen.

6.5 Conclusion

A new digital holographic polariscope using single and double exposure digital holographic method is described in detail using both simulated and experimental methods for analyzing birefringent and non-birefringent specimens. The results are compared with conventional polariscope under Sodium light source. It is found that conventional polariscope could not record isopachic fringes of non-birefringent

specimen under stress whereas we could obtain isopachic fringes using digital holographic polariscope. It is also found that it is difficult to separate isochromatic and isopachics fringe system as they are always superposed but one can record separately isopachic fringes using an unstressed specimen as the object and in a digital holographic polariscope (Figure 6.2) by using double exposure holography. Also, the theoretical analysis clearly shows that isochromatic and isopachic fringes are superposed and that is evident from the dependence of $(\sigma_1-\sigma_2)$ and $(\sigma_1+\sigma_2)$ terms in phase retardation δ.

CHAPTER 7

CONCLUSION

Digital holography is an advanced imaging tool matured in recent years with the development of high-resolution image sensor and computing technology. And its variant called digital holographic interferometry is a highly sensitive metrology tool which can measure optical phase difference, in the order of fraction of the wavelength, between two states of an object. In this thesis work, an off-axis digital hologram recording setup was configured with optical fiber guides and real-time numerical reconstruction software was developed in LabVIEW to carry out all imaging and measurements.

The need for highly reliable components and fast inspection of large and complex structures resulted in employing, non-contact, whole field and strength based optical interferometry inspection techniques, by aerospace industries. Moreover, with the development of new materials and novel manufacturing techniques, conventional sensor technologies failed in properly inspecting the fabricated components. In this thesis, prevailing issues during the inspection of honeycomb core metallic sandwich panel were addressed and solutions were proposed therein, using time average method of digital holography.

The feasibility of time average method of digital holography in detecting debond along a curved sandwich construction with high curvature was studied. Towards this, the dynamic response of debonded face sheet along the curved edge was mapped and compared with that of flat panels. The behaviour of debonded face sheet along a curved edge is found similar to that of a flat panel. The feasibility of this technique is validated through programmed defects. However, the time consuming sinusoidal frequency sweep during time average method in search of the local resonances of each type and size of defects causes delay in the inspection. A

single source multi-frequency excitation strategy making use of the Fourier components of a square wave is proposed to avoid the frequency sweep. The difficulties in defect detection through sinusoidal and random excitations were illustrated. Moreover, displacement responses of single and multiple debond under square wave excitation with respect to the magnitude and location of excitation source are demonstrated. In this way, the inspection time drastically comes down and interferogram evaluation becomes reliable.

The geometric and material discontinuities due to the potted-inserts in a sandwich structure alter its dynamic response and their effects were studied using time average method.in this work. A plate with multiple local stiffeners could simulate the response at potted-inserts which act as highly rigid points at high frequency of excitation. The extent of debond also can be evaluated at high excitation frequency.

A method is also proposed to compute time average holographic fringe pattern under periodic non-sinusoidal or random excitation in this thesis. The probability density function of the displacement response, obtained through transient response analysis using finite element method, approximates the vibration amplitude of the object corresponds to locations where the object spends more time. Random excitation signals generated from the power spectral density curve was used for object excitation. Time average fringes were plotted and compared with the experimental results for a plate with a defect.

Finally, a digital holographic polariscope is proposed with single element circular polarizer to image the isochromatic and isopachic of transparent materials (birefringent and non-birefringent) instead of conventional four-element circular polariscope. Imaging of stresses in non-birefringent materials through double exposure digital holographic interferometry is also demonstrated. This method can be used for inspection of non-birefringent transparent materials through imaging the stress concentrations due to defects.

7.1 Recommendations for Future Work

Digital holographic polariscope can be further extended to image stress fields across the thickness of the material. The numerical focusing capability of digital holography can be made use of for tomography of stress fields for better visualization and reduction in error during quantification. Interference phase map from double exposure digital holography can be used for phase evaluation of isopachic fringe system. Quality of the isopachic and isochromatic fringes can be further improved through convolution approach of numerical reconstruction.

REFERENCES

1. Ajovalasit, A. (1974). Holographic photoelasticity: Influences of inaccuracies of optical retarders on isochromatics and isopachics. *Journal of Strain Analysis, 9*(1), 52-60.

2. Alexeenko, I., Gusev, M., & Gurevich, V. (2009). Separate recording of rationally related vibration frequencies using digital stroboscopic holographic interferometry. *Applied Optics, 48*(18), 3475-3480.

3. Baba, B. O., & Thoppul, S. (2009). Experimental evaluation of the vibration behavior of flat and curved sandwich composite beams with face/core debond. *Composite Structures, 91*, 110–119.

4. Beghuin, D., Cuche, E., Dahlgren, P., Depeursinge, C., Delacretaz, G., & Salathe, R. P. (1999). Single acquisition polarization imaging with digital holography. *Electronics Letters, 35*(23), 2053-2055.

5. Bianchi, G., Aglietti, G., & Richardson, G. (2010). Static performance of hot bonded and cold bonded inserts in honeycomb panels. *Journal. of Sandwich Structures and Materials, 12*(1), 59-62.

6. Borza, D. N. (2005). Mechanical vibration measurement by high-resolution time-averaged digital holography. *Measurement Science and Technology, 16*, 1853–1864.

7. Bozhevolnaya, E.; Lyckegaard, A.; Thomsen, O. T.; Skvortsov, V. (2004). Local effects in the vicinity of inserts in sandwich panels. *Composites: Part B, 35*, 619–627.

8. Burlayenko, V. N., & Sadowski, T. (2014). Nonlinear dynamic analysis of harmonically excited debonded sandwich plates using finite element modeling. *Composite Structures, 108*, 354–366.

9. Burlayenko, V. N.; Sadowski, T. (2010). Influence of skin/core debonding on free vibration behavior of foam and honeycomb-cored sandwich plates. *International Journal of Non-Linear Mechanics, 45*, 959 – 968.

10. Burlayenko, V. N.; Sadowski, T. (2012). Finite element nonlinear dynamic analysis of sandwich plates with partially detached face sheet and core. *Finite Elements in Analysis and Design, 62*, 49-64.

11. Chatelain, B. (1973). Holographic photoelasticity: independent observation of the isochromatic and isopachic fringes for a single model subjected to only one process. *Optics and Laser Technology, 5*, 201-204.

12. Chau, H. H. (1968). Holographic interferometer for isopachic stress analysis. *Review of Scientific Instruments, 39*(12), 1789-1792.

13. Clarady, J. F. (1990). Electronic holographic NDE. *Review of Progress in Quantitative Non-destructive Evaluation, 9*, pp. 1031-1038.

14. Clarady, J. F., & Summers, M. (1993). Electronic holography and shearography NDE for inspection of modern materials and structures. *Review of Progress in Quantitative Non-destructive Evaluation, 12*, pp. 381-386.

15. Clarady, J. F., Jessee, J. K., & Bearden, J. L. (1983, October 11). *US Patent No. US4408881A*.

16. Colomb, T., Dahlgren, P., Beghuin, D., Cuche, E., Marquet, P., & Depeursinge, C. (2002). Polarization imaging by use of digital holography. *Applied Optics, 41*(1), 27-37.

17. Colomb, T., Dürr, F., Cuche, E., Marquet, P., P, L. H., Salathe, R. P., & Depeursinge, C. (2005). Polarization microscopy by use of digital holography: application to optical-fiber birefringence measurements. *Applied Optics, 44*(21), 4461-4469.

18. Desse, M. J., & Olchewsky, F. (2018). Dual-reference digital holographic interferometry for analyzing high-density gradients in fluid mechanics. *Optics Letters, 43*(8), 1635-1638.

19. Erdogan, H., & Yetmez, M. (2014). Experimental dynamic analysis on naturally curved honeycomb sandwich beams with different damage patterns. *Mat.-wiss. u. Werkstofftech.(Material Science and Engineering Technology), 45*(4), 306-313.

20. Erf, R. K. (1974). *Holographic non-destructive testing.* New York: Academic Press Inc.

21. Erf, R. K., Aas, H. G., & Waters, J. P. (1970). Bond inspection by dynamic time-average interferometric holography of ultrasonically excited plates. *Journal of Acoustical Society of America, 47*(4), 968-969.

22. Farrar, C. R., & Doebling, S. W. (1997). An overview of modal-based damage identification methods. *EUROMECH 365 International Workshop: DAMAS 97.*

23. *FEAST*. (2018). Retrieved from FEAST, Structural Analysis software of Indian Space Research Organization based on Finite Element Method: feast.vssc.gov.in

24. Ferraro, P. (1991). Evaluation by Holographic Interferometry of Impact Damage in Composite Aeronautical Structures. *Proceedings of SPIE, 1553*, 349-357.

25. Ferraro, P., Ferraiuolo, A., Imaparato, S. I., Voto, C., & Stetson, K. .. (1994). On the holographic detection of core-to-skin disbonds in composite sandwich structures. *Materials evaluation, 52*(12), 1376-1381.

26. Findeis, D., & Gryzagoridis, J. (2014). Digital shearography and vibration excitation for NDT of aircraft components. *American Institute of Physics Conference Proceedings-AIVELA 2014*, *1600*, pp. 33-38.

27. Fourney, E. M. (1968). Application of holography to photoelasticity. *Experimental Mechanics, 8*, 33-38.

28. Fourney, M. E., & Mate, K. V. (1970). Further Application of holography to photoelasticity. *Experimental Mechanics, 10*, 177-186.

29. Fritzen, C. P. (2005). Vibration-based structural health monitoring – concepts and applications. *Key Engineering Materials, 293-294*, pp. 3-20.

30. Fryer, P. A. (1970). Vibration analysis by holography. *Reports on Progress in Physics, 33*, 489-531.

31. Gandomi, H., Sahab, M. G., Rahaei, A., & Gorji, M. S. (2008). Development in mode shape-based structural fault identification technique. *World Applied Sciences Journal, 5*(1), 29-38.

32. Ganesan, A. R., Meinlschmidt, P., & Hinsch, K. (1994). Vibration mode separation using comparative electronic speckle pattern interferometry. *Optics Communications, 107*, 28-34.

33. Ganesan, A. R.; Hinsch, K. D.; Meinlschmidt, P. (2000). Transition between rationally and irrationally related vibration modes in time-average holography. *Optics Communications, 174*, 347–353.

34. Gaskil, J. D. (1978.). *Linear Systems, Fourier Transforms and Optics.* New York: John Wiley & Sons.

35. Goodman, J. W., & Lawrence, R. W. (1967). Digital image formation from electronically detected holograms. *Applied Physics Letters, 11*(3), 77-79.

36. Gupta, P. C., & Singh, K. (1975). Characteristic fringe function for time-average holography of periodic non-sinusoidal vibration. *Applied Optics, 14*(1), 129-133.

37. Heimbs, S., & Pein, M. (2009). Failure behaviour of honeycomb sandwich corner joints and inserts. *Composite Structures, 89*, 575–588.

38. Hovanesian, J. D., Brcic, V., & Powell, R. L. (1968). A new experimental stress optic method: Stress–holo-interferometry. *Experimental Mechanics, 8*(8), 362-368.

39. Huang, S. J., & Lin, Y. T. (2008). Out-of-plane strain measurement in sandwich plates with single fully potted insert by using digital shearography. *Strain, 44*, 253–258.

40. Huang, S. J.; Lin, H. L.; Liu, H. W. (2007). Electronic speckle pattern interferometry applied to the displacement measurement of sandwich plates with single 'fully potted' insert. *Composite Structures, 79*, 157-162.

41. Hung, Y. Y., Luo, W. D., Lin, L., & Shang, H. M. (2000b). NDT of joined surfaces using digital time-integrated shearography with multiple-frequency sweep. *Optics and Lasers in Engineering, 33*, 369-382.

42. Hung, Y. Y.; Luo, W. D.; Lin, L.; Shang, H. M. (2000a). Evaluating the soundness of bonding using shearography. *Composite Structures, 50*, 353-362.

43. Ibarra-Castanedo, C., Piau, J.-M., Guilbert, S., Avdelidis, N. P., Genest, M., Bendada, A., & Maldague, X. P. (2009). Comparative study of active thermography techniques for the nondestructive evaluation of honeycomb structures. *Research in Nondestructive Evaluation, 20*, 1-31.

44. Kaufmann, G. H. (Ed.). (2011). *Advances in Speckle Metrology and Related Techniques.* Germany: WILEY-VCH Verlag & Co. KGaA:.

45. Kihara, T., Kubo, H., & Nagata, R. (1976). Isopachics measurement using immersion method polarization holography. *Applied Optics, 15*(12), 3025-3028.

46. Kreis, T., Juptner, W., & Biedermann, R. (1995). Neural network approach to holographic nondestructive testing. *Applied Optics, 34*(8), 1407-1415.

47. Kreis, Thomas. (2005). *Handbook of holographic interferometry: optical and digital methods.* Weinheim: WILEY-VCH GmbH & Co. KGaA.

48. Kumar, M., & Shakher, C. (2016). Experimental characterization of the hygroscopic properties of wood during convective drying using digital holographic interferometry. *Applied Optics, 55*(5), 960-968.

49. Larkin, K. G., Bone, D. J., & Oldfield, M. A. (2001). Natural demodulation of two-dimensional fringe patterns. I. General background of the spiral phase quadrature transform. *Journal of Optical Society of America, 18*(8), 1862-1870.

50. Lee, C.-K., & Hu, C. -P. (1986). Analytical methods for photoelastic holography. *Applied Optics, 25*(12), 1912-1916.

51. Marshall, I. (1991). *Composite structures 6.* New York: Elsevier Applied Science.

52. Matczak, M. J. (1994). Computer-aided simulation of deformation measurements by means of holographic interferometry. *Proceedings of SPIE, 2342*, 150-154.

53. Molin, N. E. (1998). Applications of whole field interferometry in mechanics and acoustics. In K. T. Grattan (Ed.), *Proceedings of the Applied Optics Divisional Conference of the Institute of Physics*, (pp. 3-10). Brighton.

54. Molin, N. E., & Stetson, K. A. (1969). Measuring combination mode vibration patterns by hologram interferometry. *Journal of Scientific Instruments (Journal of Physics E) series 2, 2*, 609-612.

55. Molin, N.-E. (1999). Applications of whole field interferometry in mechanics and acoustics. *Optics and Lasers in Engineering, 31*, 93-111.

56. Montalvão, D., Maia, N. M., & Ribeiro, A. M. (2006, July). A review of vibration-based structural health monitoring with special emphasis on composite materials. *The Shock and Vibration Digest, 38*(4), 295–324.

57. Mukhopadhyay, M. (2008). *Structural Dynamics: Vibrations and Systems.* India: Ane Books.

58. Narayanamurthy, C. S., Pedrini, G., & Osten, W. (2017). Digital holographic photoelasticity. *Applied Optics, 56*(13), F213-F217.

59. Narayanamurthy, C. S.; Dainty, J. C. (1992). Real-time holographic metrology using BSO. *Opt. Commun, 91*, 23-28.

60. Nisida, M., & Saito, H. (1964). A new interferometric method of two-dimensional stress analysis. *Experimental Mechanics, 4*(12), 366-376.

61. P. Ferraro, A. F. (1994). On the holographic detection of core-to-skin disbonds in composite sandwich structures. *Materials Evaluation, 52*, 1376-1381.

62. Pedersen, H. M., & Lglkberg, O. J. (1994). Detection of non-sinusoidal periodic vibrations using phase-modulated TV-holography. *Optics Communications, 104*, 271-276.

63. Pérez-Huerta, J. S., Saucedo-Anaya, T., Moreno, I., Ariza-Flores, D., & Saucedo-Orozco, B. (2017). Digital holographic interferometry applied to the investigation of ignition process. *Optics Express, 25*(12), 13190-13198.

64. Picart, P., Leval, J., Mounier, D., & Gaugeon, S. (2003). Time averaged digital holography. *Optics Letters, 28*(20), 1900-1902.

65. Powell, R. I.; Stetson, K. A. (1965). Interferometric vibration analysis by wavefront reconstruction. *Journal of Optical Society of America, 55*(12), 1593-1598.

66. Pryputniewicz, R. J. (1985). Time average holography in vibration analysis. *Optical Engineering, 24*(5), 843 -848.

67. Quiroga, A. J., Daniel, C., & Jose, G. P. (2007). XtremeFringe®: state of the art software for automatic processing of fringe patterns. *Proceedings of SPIE, 6616*.

68. Ragulskis, M., Palevicius, A., & Ragulskis, L. (2003). Plotting holographic interferograms for visualization of dynamic results from finite-element

calculations. *International Journal for Numerical Methods in Engineering, 56*, 1647–1659.

69. Rao, G. N., Agrawal, U., & Naik, N. (2005). Sandwich structures with composite inserts: Experimental studies. In O. T. Thomsen, E. Bozhevolnaya, & A. Lyckegaard (Ed.), *Proceedings of the 7th International Conference on Sandwich Structures.30*, pp. 997-1006. Netherlands: Springer.

70. Regan, R. O., & Dudderar, T. D. (1971). A new holographic interferometer for stress analysis. *Experimental Mechanics, 11*, 241-247.

71. Roesel, M., Herstrass, K., & Bajons, P. (2003). Computer generated optical holographic fringe patterns for the analysis of vibrating structures. *Ultrasonics, 41*, 663–669.

72. Ruiz, C. G., Torre-Ibarra, M. H., Flores-Moreno, J. M., Frausto-Reyes, C., & Santoyo, F. M. (2018). Cortical bone quality affectations and their strength impact analysis using holographic interferometry. *Biomedical Optics Express, 9*(10), 4818-4833.

73. Sanford, R. J. (1980). Photoelastic holography- A modern tool for stress analysis. *Experimental Mechanics, 20*, 427-436.

74. Schnars, U., & Juptner, W. (1994a). Direct recording of holograms by a CCD target and numerical reconstruction. *Applied Optics, 33*(2), 179-181.

75. Schnars, U., & Juptner, W. P. (1994b). Digital recording and reconstruction of holograms in hologram interferometry and shearography. *Applied Optics, 33*(20), 4373-4377.

76. Schnars, U.; Juptner, W. P. O. (2002). Digital recording and numerical reconstruction of holograms. *Measurement Science and Technology, 13*, R85-R101.

77. Schnars, U.; Kreis, T. M.; Juptner, W. P. O. (1996). Digital recording and numerical reconstruction of holograms- Reduction of spatial frequency spectrum. *Optical Engineering, 35*(4), 977-982.

78. Servin, M., Quiroga, J. A., & Marroquin, J. L. (2003). General n-dimensional quadrature transform and its application to interferogram demodulation. *Journal of Optical Society of America A, 20*(5), 925–934.

79. Sfarra, S., Ibarra-Castanedo, C., Avdelidis, N., Genest, M., Bouchagier, L., Kourousis, D., . . . Paoletti, D. (2010). A comparative investigation for the nondestructive testing of honeycomb structures by holographic interferometry and infrared thermography. *15th International Conference on Photoacoustic and Photothermal Phenomena (Journal of Physics: Conference Series 214).* IOP Publishing Ltd.

80. Shahdin, A., Morlier, J., & Gourinat, Y. (2010). Damage monitoring in sandwich beams by modal parameter shifts: A comparative study of burst random and sine dwell vibration testing. *Journal of Sound and Vibration, 329*, 566–584.

81. Sharma, S., Sheoran, G., & Shakher, C. (2012). Digital holographic interferometry for measurement of temperature in axi-symmetric flame. *Applied Optics, 51*(16), 3228-3235.

82. Steinchen, W., Yang, L., & Kupfer, G. (1997). Digital shearography for non-destructive testing and vibration analysis. *Experimental Techniques*, 20-23.

83. Stetson, K. A. (1971). Hologram interferometry of non-sinusoidal vibrations analyzed by density functions. *Journal of the Optical Society of America, 61*(10), 1359-1362.

84. Stetson, K. A.; Powell, R. I. (1965). Interferometric Hologram Evaluation and Real-Time Vibration Analysis of Diffuse Objects. *Journal of Optical Society of America, 55*(12), 1694-1695.

85. Tahara, T., Awatsuji, Y., Shimozato, Y., Kakue, T., Nishio, K., Ura, S., . . . Matoba, O. (2011). Single-shot polarization-imaging digital holography based on simultaneous phase-shifting interferometry. *Optics Letters, 36*(16), 3254-3256.

86. Theocaris, P. S. (1979). *Matrix theory of photoelasticity.* New York: Springer-Verlag Berlin Heidelberg GmbH.

87. Theocaris, P. S., & Gdoutos, E. E. (1978). A unified interpretation of interferometric and holographic fringe patterns in photoelasticity. *Strain Analysis, 13*(2), 95-102.

88. Thomas, B. P., & Pillai, S. A. (2009, May). Digital holographic interferometry for whole field NDT applications. *Journal of aerospace sciences and technologies, 61*(2), 334-341.

89. Thomas, B. P., Kumar, A., Rajendran, K. V., & Pillai, S. A. (2005). Theoretical simulation and experimental validation of holographic interferograms and shearograms. *Proceedings of International Conference on Experimental Mechanics (ICEM05).* Delhi.

90. Thomas, B. P.; Rajendran, K. V.; Pillai, S. A. (2007). Whole field NDT of thermal protection system using digital holography. *INSIGHT, Journal of The British Institute of NDT, 49*(5), 279-282.

91. Thomsen, O. T. (1998). Sandwich plates with through-the-thickness and 'fully potted' inserts: evaluation of differences in structural performance. *Composite Structures, 40*(2), 159-174.

92. Thomsen, O. T., & Rits, W. (1998). Analysis and design of sandwich plates with inserts-a high-order sandwich plate theory approach. *Composites Part B, 29B*, 795–807.

93. Toh, S. L., Shang, H. M., Chau, F. S., & Tay, C. J. (1991). Flaw detection in composites using time-average shearography. *Optics and Laser Technology, 23*(1), 25-30.

94. Vest, C. M. (1979). *Holographic interferometry.* New York: John Wiley & Sons.

95. Wagner, C., Seebacher, S., Osten, W., & Juptner, W. (1999). Digital recording and numerical reconstruction of lensless Fourier holograms in optical metrology. *Applied Optics, 38*(22), 4812-4820.

96. Wilson, A. D. (1970). Characteristic functions for time-average holography. *Journal of the Optical Society of America, 60*(8), 1068-1071.

97. Wilson, A. D. (1971). Computed time-average holographic interferometric fringes of a circular plate vibrating simultaneously in two rationally or irrationally related modes. *Journal of the Optical Society of America, 61*(7), 924-929.

98. Wilson, A. D.; Strope, D. H. (1970). Time-average holographic interferometry of a circular plate vibrating simultaneously in two rationally related modes. *Journal of the Optical Society of America, 60*(9), 1162-1165.

99. Yan, J.-x., Liu, C.-s., Liu, T.-z., & Zhao, L.-l. (2009). A review on advances of damage identification methods based on vibration. *Key Engineering Materials, 413-414*, 277-283.

100. Zambuto, M., & Lurie, M. (1970). Holographic Measurement of General Forms of Motion. *Applied Optics, 9*(9), 2066-2072.

101. Zou, Y., Tong, l., & Steven, P. G. (2000). Vibration-based model-dependent damage (delamination) identification and health monitoring for composite structures - A review. *Journal of Sound and Vibration, 230*(2), 357-378.

APPENDICES

Appendix I

For measuring isopachic fringes from an unstressed photoelastic specimen the digital holographic geometry does not require circular retarders and they can be removed. Figure 6.2 represents the modified digital holographic polariscope. To record isopachic fringes, first hologram is recorded with unstressed state and second hologram is recorded after applying stress to the specimen,

$$E_{\mathrm{O}}=\begin{bmatrix}M_{11} & M_{12}\\ M_{21} & M_{22}\end{bmatrix}\begin{bmatrix}0 & 0\\ 0 & 1\end{bmatrix}\begin{bmatrix}E_{ox}e^{i\xi_x}\\ E_{oy}e^{i\xi_y}\end{bmatrix} \tag{A.1}$$

where

$$\begin{bmatrix}M_{11} & M_{12}\\ M_{21} & M_{22}\end{bmatrix}=e^{\left[\frac{-\mathrm{i}\pi}{\lambda}(n_1+n_2-2n_0)t\right]} \tag{A.2}$$

$$\begin{bmatrix}\cos\theta & -\sin\theta\\ -\sin\theta & \cos\theta\end{bmatrix}\begin{bmatrix}\mathrm{e}^{\left(\frac{+\mathrm{i}\delta}{2}\right)} & 0\\ 0 & \mathrm{e}^{\left(\frac{-\mathrm{i}\delta}{2}\right)}\end{bmatrix}\begin{bmatrix}\cos\theta & \sin\theta\\ -\sin\theta & \cos\theta\end{bmatrix}$$

Now, Equation (A.1) becomes,

$$E_{\mathrm{O}}=E_{oy}e^{i\xi_y}\begin{bmatrix}M_{12}\\ M_{22}\end{bmatrix} \tag{A.3}$$

and the intensity of recorded hologram will be given by,

$$I_{\mathrm{H}}=E_O^{+}J_RE_O \tag{A.4}$$

$$I_{\mathrm{H}}=\frac{1}{2}E_{oy}^2\begin{bmatrix}M_{12} & M_{22}\end{bmatrix}\begin{bmatrix}0 & 0\\ 0 & 1\end{bmatrix}\begin{bmatrix}M_{12}\\ M_{22}\end{bmatrix} \tag{A.5}$$

$$I_{\mathrm{H}}=\frac{1}{2}E_{oy}^{2}|M_{22}|^{2} \tag{A.6}$$

$$I_{\mathrm{H}}=\left|sin^{2}\theta \mathrm{e}^{\left(\frac{+\mathrm{i}\delta}{2}\right)}+cos^{2}\theta \mathrm{e}^{\left(\frac{-\mathrm{i}\delta}{2}\right)}\right|^{2} \tag{A.7}$$

$$I_{\mathrm{H}}=(sin^{2}\theta-cos^{2}\theta)+4\,sin^{2}\theta\,cos^{2}\theta\,cos^{2}\frac{\delta}{2} \tag{A.8}$$

For a photoelastic stress birefringent model the value of $\theta=\pi/4$ and substituting this in Equation. (A.8) we get,

$$I_{\mathrm{H}}=\frac{1}{2}E_{oy}^{2}\,cos^{2}\frac{\delta}{2} \tag{A.9}$$

Appendix II

For, non-birefringent materials the refractive index will be a constant value and it doesn't change with loading. Therefore these materials are insensitive to conventional polariscope arrangement. The non-birefringent materials only exhibit the thickness variations and these fringes are known as isopachic fringes. The double exposure digital holography records two holograms one before stress and after the stress is applied to the specimen. The reconstructed hologram is combination of interference patterns obtained before and after the object has undergone a stress. Since the refractive index is not changing with load the intensity equation becomes,

$$I = |exp(-i\phi) + exp[-i(\phi + \Delta\phi)]|^2 \tag{B.1}$$

$$= exp(-i\phi) + exp[\ -i(\phi + \Delta\phi)]^2\ exp\ [\ \ i(2\phi + \Delta\phi)] \tag{B.2}$$

$$= exp(-i\phi) + exp[-2i(\phi + \Delta\phi)]\ exp\ [\ i(2\phi + \Delta\phi)] \tag{B.3}$$

$$2(1 + cos\,\Delta\phi) = 4cos^2\left(\frac{\Delta\phi}{2}\right) \tag{B.4}$$

$$\Delta\phi = \frac{2\pi t_0}{\lambda}\left[(A + B) - 2\frac{\gamma}{E}(n_0 - n)\right](\sigma_1 + \sigma_2) \tag{B.5}$$

$$I = 4cos^2\left(\frac{\frac{2\pi t_0}{\lambda}\left[(A + B) - 2\frac{\gamma}{E}(n_0 - n)\right](\sigma_1 + \sigma_2)}{2}\right) \tag{B.6}$$

$$I = 4cos^2\left[\frac{\pi t_0}{\lambda}(A' + B')(\sigma_1 + \sigma_2)\right] \tag{B.7}$$

$$I = 4cos^2\left[\frac{\pi}{\lambda}t_0\ C\ (\sigma_1 + \sigma_2)\right] \tag{B.8}$$

Appendix III

The circular polariscope is obtained from the plane polariscope by introducing two quarter wave plates, the first quarter wave plate after the polarizer and the second quarter wave plate before the analyzer whose fast axes makes angle $\pm 45^0$ with the axes of polarizer and analyzer. When the fast axes of the two quarter-wave plates are in opposite direction, no light emerges from analyzer so dark circular polariscope is obtained. When the fast axes of the two quarter-wave plates are parallel to each other then, bright circular polariscope is obtained (Theocaris, 1979). Following theoretical explanation gives the light intensity obtained for a bright circular polariscope (Figure 6.6). The component of light vector is given for the field shown in Figure 6.5 as,

$$\begin{bmatrix} E_x \\ E_y \end{bmatrix} = P_o \; Q_{+45} P_b Q_{-45} \; A_o \tag{C.1}$$

$$\begin{bmatrix} E_x \\ E_y \end{bmatrix} = \frac{1}{\sqrt{2}} e^{\left[\frac{-i\pi}{\lambda}(n_1+n_2-2n_0)t\right]} \begin{bmatrix} 0 & 0 \\ 0 & 1 \end{bmatrix} \begin{bmatrix} 1 & i \\ i & 1 \end{bmatrix}$$

$$\times \begin{bmatrix} sin^2\theta e^{\left(\frac{-i\delta}{2}\right)} + cos^2\theta e^{\left(\frac{+i\delta}{2}\right)} & 2i \sin\theta\cos\theta \; sin\frac{\delta}{2} \\ 2i \sin\theta\sin\theta \; sin\frac{\delta}{2} & sin^2\theta \; e^{\left(\frac{+i\delta}{2}\right)} + cos^2\theta e^{\left(\frac{-i\delta}{2}\right)} \end{bmatrix} \begin{bmatrix} 1 & -i \\ -i & 1 \end{bmatrix} \begin{bmatrix} 0 \\ 1 \end{bmatrix} \tag{C.2}$$

$$\begin{bmatrix} E_x \\ E_y \end{bmatrix} = \frac{1}{\sqrt{2}} e^{\left[\frac{-i\pi}{\lambda}(n_1+n_2-2n_0)t\right]} \begin{bmatrix} 0 \\ (M_{11}+M_{22}) + i(M_{12}-M_{21}) \end{bmatrix} \tag{C.3}$$

whereM_{11}, M_{22}, M_{12} and M_{21}represent similar values as given in Equation 6.4. The light intensity is given by,

$$I = [E_x^* \quad E_y^*] \begin{bmatrix} E_x \\ E_y \end{bmatrix} = |(M_{11}+M_{22}) + i(M_{12}-M_{21})|^2 = cos^2\frac{\delta}{2} \tag{C.4}$$

Appendix IV

1. MATLAB code for generating a random time signal from PSD

```
clear all
% Length of time signal
T = 1;
% Frequency range (Hz)
Startf=5000;
Endf=6000;
f1=Endf;
% Sample rate of time signal
fs = 30*f1;
% Build PSD
rmsLevel = .707;
df = 1/(2*T);
PSD = zeros(T*fs, 1);
fori=Startf:Endf
PSD(i*T+1) = ((rmsLevel^2)/df) /2;
PSD(end-i*T+1) = ((rmsLevel^2)/df) /2;
end
N=length(PSD);
frequency = ((-N/2):(N/2))*df;
X = sqrt(PSD.*T);
%Generation of white noise
even = true;
Nhalf = N/2-1;
if rem(N,2) ~= 0; even = false; Nhalf = (N-1)/2; end
rms_level = 1;
RNoise = rand(Nhalf, 1).*2*pi; % Random phase between 0 and 2pi
Whitenoise = rms_level.*exp(1i*randnums);   % white noise
% Linear spectrum for white noise
```

```
if even
linspecPF = [rms_level; RNoise; rms_level];%+ Freqs
else
linspecPF = [rms_level; Whitenoise];  %+Freqs
end
linspecNF = fliplr(conj(Whitenoise));      %-Freqs
nLinSpec = [linspecPF; linspecNF];
% Multiply noise * signal linear spectra in frequency-domain
totalLinSpec = X.*nLinSpec;
% Convert PSD to units in time domain
timeseries = real(ifft(totalLinSpec)*N*df);
time=linspace(0,T,fs*T);
figure(3)
plot(time, timeseries)
title('Generated Timesignal From PSD')
xlabel('Time (Sec)')
ylabel('Amplitude [mm]')
%FFT to check the content
t=time;
L=length(t);
Fs=1/((t(2)-t(1)));
y=timeseries;
figure;
NFFT = 2^nextpow2(L); % Next power of 2 from length of y
Y = fft(y,NFFT)/L;
f = Fs/2*linspace(0,1,NFFT/2);
% Plot single-sided amplitude spectrum.
plot(f,2*abs(Y(1:NFFT/2)))
freq=f';
title('Single-Sided Amplitude Spectrum of y(t)')
xlabel('Frequency (Hz)')
ylabel('|Y(f)|')
```

2. MATLAB code for generating square wave signal

a. Using summation of Fourier components

```
t = linspace(-1,1,10000);   % time
f = 0*t; % creates a zero valued function
 N=25; % number of harmonics
i=1;
for k=-N:1:N
if(k==0)  % skip the zeroth term
C_k(i)=0;
i=i+1;
continue;
end;
   % computes the k-th Fourier coefficient of the exponential form
C_k(i) = ((1)/(pi*1i*k))*(1-exp(-pi*1i*k));
f_k = C_k(i)*exp(2*pi*1i*k*t);   % k-th term of the series
   f = f + f_k; % adds the k-th term to f
i=i+1;
end
k=-N:1:N;
% Fourier components of square wave
bar(N+1:2*N+1, abs(C_k(N+1:2*N+1)),.02);
gridon;
xlabel('f');
ylabel('C_k');
% Square wave time signal
figure;
plot(t, f, 'LineWidth', 2);
gridon;
xlabel('t');
ylabel('f(t)');
```

b. Using built in MATLAB function

```
fid = fopen('square.txt', 'wt');
time=0;
fori=1:500:5000
t = time:1/(i*2*10):time+1001/((i*2*10));
y = square (2*pi*i*t);
a=[t(1:1000);y(1:1000)];
fprintf(fid,'%f  %f\n',a);
time=time+1001/((i*2*10));
end
fclose(fid)
```

Appendix V

MATLAB code for generating time average fringe pattern from the nodal displacement response

```
clearall;
% Read coordinates of the nodes from the finite element model
fid = fopen('coordinates.txt','r') ;
D{1} = textscan(fid, '%s %d %s %s %d %s %s %d %s %s %d');
fclose(fid);
 Nod=D{1,1}{1,2};
x=D{1,1}{1,5};
y=D{1,1}{1,8};
xm=double(x);
ym=double(y);
[xp,yp]=meshgrid(0:0.05:100,0:0.05:260);
% Read displacement response of the nodes from FE model
 cc=dlmread('rec plate tans defect R5000-6000.txt');
for k=1:4001
Da(k,1:6681)=cc(6682*(k-1)+2:k*6682,4);
end
%Time average fringe
MaxVal={};
binranges= [min(abs(Da(:))):0.0001:max(abs(Da(:)))];
fori=1:6681
[num,ix] =(histc( abs(Da(:,i)), binranges ));
MaxVal=[MaxVal,binranges(max(ix))];
end
q=cell2mat(MaxVal);
q=q';
colormapgray
F=TriScatteredInterp(xm,ym,q);
Intenp1=F(xp,yp);
```

```
B=5;D=5;
Intenpp1=tanh(B*Intenp1)./tanh(D);
imagesc(Intenpp1);
% PDF at one node
figure;
ft=fitdist(abs(Da(1000:2000,3593)),'Normal');
binranges=
[min(abs(Da(1000:2000,3593))):0.0001:max(abs(Da(1000:2000,3593)))];
pd=pdf(ft,binranges);
plot(binranges,pd)
[t,tt]=max(pdf(ft,binranges))
Val=binranges(tt);
```

LIST OF PUBLICATIONS BASED ON THE THESIS

Publications in Peer-Reviewed International Journal

1. Thomas, B. P., Pillai S. A. and Narayanamurthy, C. S. (2017). Investigation on vibration excitation of debonded sandwich structures using time average digital holography. *Applied Optics*, 56 (13), F7–F13.***(Editors' pick)***

2. Thomas, B. P., Pillai, S. A. and Narayanamurthy, C. S. (2019). Digital holographic study on the dynamic response of plates with geometric and material discontinuities simulating potted-insert metallic honeycomb sandwich structures. *Applied Optics*, 58(5), A33–A40.

3. Thomas, B. P., Pillai, S. A. and Narayanamurthy, C. S. (2019). Photoelastic digital holographic polariscope. *Journal of Modern Optics*, 66(8), 817-828 DOI: 10.1080/09500340.2019.1575484

4. Thomas, B. P., Pillai, S. A. and Narayanamurthy, C. S. Computed time average holographic fringe pattern of a defective plate under random excitation*(to be submitted)*

Presentation in Conference

5. Thomas, B. P., Pillai, S. A. and Narayanamurthy, C. S. (2013). Time average digital holographic interferometry for non-destructive testing of curved sandwich structures, *37th National Symposium of Optical Society of India*, Pondicherry University, India